3. CAROLINA SLOPE, SITES 1054 AND 1055[1]

Shipboard Scientific Party[2]

HOLE 1054A

Position: 33°0.000′N, 76°17.000′W (Carolina Slope)

Start hole: 1817 hr, 19 February 1997

End hole: 2015 hr, 20 February 1997

Time on hole: 25.97 hr (1.08 days)

Seafloor (drill-pipe measurement from rig floor, mbrf): 1302.5

Distance between rig floor and sea level (m): 11.2

Water depth (drill-pipe measurement from sea level, m): 1291.3

Total depth (from rig floor, mbrf): 1502.5

Penetration (mbsf): 200.0

Coring totals:
Type: APC; Number: 11; Cored: 94.30 m; Recovered: 95.74 m (101.53%)
Type: XCB; Number: 11; Cored: 105.70 m; Recovered: 86.81 m (82.13%)
Total: Number: 22; Cored: 200.00 m; Recovered: 182.55 m (91.28%)

Oldest formation cored: middle Pliocene silty and clayey mixed sediment with diatoms, foraminifers, and nannofossils

HOLE 1054B

Position: 32°59.985′N, 76°17.000′W (Carolina Slope)

Start hole: 2015 hr, 20 February 1997

End hole: 0455 hr, 21 February 1997

Time on hole: 8.67 hr (0.36 days)

Seafloor (drill-pipe measurement from rig floor, mbrf): 1304.8

Distance between rig floor and sea level (m): 11.2

Water depth (drill-pipe measurement from sea level, m): 1293.6

Total depth (from rig floor, mbrf): 1408.0

Penetration (mbsf): 103.2

Coring totals:
Type: APC; Number: 12; Cored: 103.20 m; Recovered: 106.29 m (102.99%)

Oldest formation cored: early Pleistocene silty and clayey mixed sediment with diatoms, foraminifers, and nannofossils

HOLE 1054C

Position: 32°59.968′N, 76°17.000′W (Carolina Slope)

Start hole: 0455 hr, 21 February 1997

End hole: 1654 hr, 21 February 1997

Time on hole: 11.98 hr (0.50 days)

Seafloor (drill-pipe measurement from rig floor, mbrf): 1305.9

Distance between rig floor and sea level (m): 11.2

Water depth (drill-pipe measurement from sea level, m): 1294.7

Total depth (from rig floor, mbrf): 1407.8

Penetration (mbsf): 101.9

Coring totals:
Type: APC; Number: 13; Cored: 101.90 m; Recovered: 104.55 m (102.60%)

Oldest formation cored: early Pleistocene silty and clayey mixed sediment with diatoms, foraminifers, and nannofossils

HOLE 1055A

Position: 32°47.042′N, 76°17.170′W (Carolina Slope)

Start hole: 1852 hr, 21 February 1997

End hole: 0045 hr, 22 February 1997

Time on hole: 5.88 hr (0.25 days)

Seafloor (drill-pipe measurement from rig floor, m): 1810.0

Distance between rig floor and sea level (m): 11.3

Water depth (drill-pipe measurement from sea level, m): 1798.7

Total depth (from rig floor, mbrf): 1819.5

Penetration (mbsf): 9.5

Coring totals:
Type: APC; Number: 1; Cored: 9.5 m; Recovered: 9.82 m (103.37%)

Oldest formation cored: Holocene(?) clayey nannofossil ooze with silt

HOLE 1055B

Position: 32°47.041′N, 76°17.179′W (Carolina Slope)

Time on hole: 9.00 hr (0.38 days)

Start hole: 0045 hr, 22 February 1997

End hole: 0945 hr, 22 February 1997

Seafloor (drill-pipe measurement from rig floor, mbrf): 1809.0

Distance between rig floor and sea level (m): 11.3

Water depth (drill-pipe measurement from sea level, m): 1797.7

Total depth (from rig floor, mbrf): 1937.0

Penetration (mbsf): 128.0

Coring totals:
Type: APC; Number: 14; Cored: 128.00 m; Recovered: 137.99 m (107.80%)

Oldest formation cored: early Pleistocene clay with nannofossils and silt

[1]Keigwin, L.D., Rio, D., Acton, G.D., et al., 1998. *Proc. ODP, Init. Repts.*, 172: College Station, TX (Ocean Drilling Program).

[2]Shipboard Scientific Party is given in the list preceding the Table of Contents.

Prior Chapter Contents Next Chapter

HOLE 1055C

Position: 32°47.056′N, 76°17.180′W (Carolina Slope)

Start hole: 0945 hr, 22 February 1997

End hole: 1955 hr, 22 February 1997

Time on hole: 10.17 hr (0.42 days)

Seafloor (drill-pipe measurement from rig floor, mbrf): 1809.0

Distance between rig floor and sea level (m): 11.3

Water depth (drill-pipe measurement from sea level, m): 1797.7

Total depth (from rig floor, mbrf): 1929.8

Penetration (mbsf): 120.8

Coring totals:
Type: APC; Number: 14; Cored: 120.80 m; Recovered: 126.10 m (104.39%)

Oldest formation cored: early Pleistocene clay with nannofossils and silt

HOLE 1055D

Position: 32°47.071′N, 76°17.179′W (Carolina Slope)

Start hole: 1955 hr, 22 February 1997

End hole: 0605 hr, 23 February 1997

Time on hole: 10.17 hr (0.42 days)

Seafloor (drill-pipe measurement from rig floor, mbrf): 1809.9

Distance between rig floor and sea level (m): 11.3

Water depth (drill-pipe measurement from sea level, m): 1798.6

Total depth (from rig floor, mbrf): 1939.0

Penetration (mbsf): 129.1

Coring totals:
Type: APC; Number: 14; Cored: 129.10 m; Recovered: 136.99 m (106.11%)

Oldest formation cored: early Pleistocene clay with nannofossils and silt

HOLE 1055E

Position: 32°47.093′N, 76°17.180′W (Carolina Slope)

Start hole: 0605 hr, 23 February 1997

End hole: 1145 hr, 23 February 1997

Time on hole: 5.67 hr (0.24 days)

Seafloor (drill-pipe measurement from rig floor, mbrf): 1809.0

Distance between rig floor and sea level (m): 11.3

Water depth (drill-pipe measurement from sea level, m): 1797.7

Total depth (from rig floor, mbrf): 1827.0

Penetration (mbsf): 18.0

Coring totals:
Type: APC; Number: 2; Cored: 18.00 m; Recovered: 18.48 m (102.67%)

Oldest formation cored: late Pleistocene clayey nannofossil ooze with silt

Principal results: Site 1054 is located on the Carolina Slope (CS) at a water depth of ~1300 m and was selected as the shallowest end-member of a transect of sites for high-resolution paleoclimate and paleo-ocean studies. The sedimentary succession recovered from the three holes at Site 1054 consists of a well-dated, 200-m-thick interval of latest middle Pliocene (Piacenzian) to Holocene nannofossil ooze and silty clay, with variable proportions of biogenic and siliciclastic components. Biocarbonates and biosilica are present throughout the succession. Three lithologic units were recognized: Unit I (0–19 meters below seafloor [mbsf], Holocene to middle Pleistocene) is clayey and silty mixed sediment defined largely on the basis of relatively abundant biocarbonates (as much as 67%) and higher amplitude oscillations in color reflectance than the underlying units; Unit II (~19 to ~119 mbsf; middle Pleistocene to early Pleistocene) is interbedded mixed sediment and silty foraminifer sand with fewer biocarbonate and color variations than the overlying unit; and Unit III (~119 to ~200 mbsf; early Pleistocene to latest middle Pliocene) is mixed sediment with higher clay content than the overlying unit. There is evidence of downslope transport with as many as 20 thin carbonate turbidites and debris-flow deposits observed at Hole 1054A, but their thickness and occurrence among Site 1054 holes suggest spatial variability.

The succession contains abundant and well-preserved calcareous nannofossils and planktonic and benthic foraminifers; diatoms are common to abundant and exhibit moderate to good preservation. Pteropods are well represented and become abundant in several discrete layers. Siliceous flagellates (including silicoflagellates and ebridians) and radiolarians range from trace to common in occurrence with good to moderate preservation. The abundance of diatoms suggests that conditions of high productivity might have characterized the area of Site 1054 in the past 2.5 m.y. Reworking and displacement of shallow-water forms is surprisingly low, in spite of the sedimentological evidence of downslope transport and current activity.

Paleomagnetic results indicate that the base of the Brunhes Chron (0.78 Ma) is located in the upper 26 mbsf of Hole 1054A, with the Jaramillo Subchron (0.99–1.07 Ma) between 27 and 31.5 mbsf. An alternate interpretation would place the base of the Brunhes at 31 mbsf, the Matuyama Chron (0.78–2.58 Ma) at 31–75 mbsf, and the Jaramillo Subchron at 33.5–50.5 mbsf. Below 75 mbsf in Hole 1054A, the magnetization signature is difficult to interpret because of drilling overprints and weak magnetizations.

Sedimentation rates were ~75 m/m.y. between 2.0 Ma and the bottom of the succession at ~2.5 Ma, ~120 m/m.y. between ~1.0 and 2.0 Ma, ~15 m/m.y. between ~0.5 and 1.0 Ma, and ~46 m/m.y. over the past 0.5 m.y. Low sedimentation rates between 0.5 and 1.0 Ma are associated with an interval where there is evidence of removal and redeposition of sediments by bottom currents.

Calcium carbonate contents fluctuate between 30 and 67 wt% with an average value of 46.5 wt%, gradually decreasing as sediment depth increases. The carbonate cycles probably reflect glacial–interglacial fluctuations. Total organic carbon (TOC) contents vary between 0.7 and 1.84 wt%, with an average value of 1.2 wt%. Organic C/N values between <5 and 10 are indicative of predominantly marine organic material. Results of Rock-Eval analysis indicate that organic matter is thermally immature with respect to petroleum generation.

Pore-water profiles from Site 1054 are typical of sediments in which sulfate reduction and methanogenesis occur. Sulfate concentrations decrease from seawater values at the top of the core to values less than 1 mM at ~48 mbsf. The onset of the methanogenic zone occurs at ~48 mbsf, coincident with the level of zero pore-water sulfate. The boundary between sulfate reduction and methanogenesis is very sharp, presumably because utilization of methane by sulfate-reducing bacteria prevents significant diffusive penetration of methane into the overlying sulfate reduction zone. The high C_1/C_2 values and the absence of a major contribution of higher molecular-weight hydrocarbons suggest that the source for methane is most likely in situ bacterial methanogenesis resulting from decomposition of organic matter in the sediments. Although Site 1054 is located in a well-characterized gas hydrate area, gradients of chloride are absent, suggesting that no gas hydrate was recovered.

Site 1055 (~1800 m) is a deeper water companion to Site 1054 on the Carolina Slope and is the second in a series of high deposition-rate locations cored for a paleoceanographic depth transect. The sedimentary succession recovered from the five holes at Site 1055 is a ~130-m-thick interval of early Pleistocene to Holocene nannofossil ooze and silty clay with variable proportions of biogenic and siliciclastic components. Biocarbonates and biosilica are present throughout the succession. Two lithologic units were recovered. Unit I (0 to ~80 mbsf; Holocene to early Pleistocene) is composed of interbedded layers of nannofossil ooze, nan-

nofossil ooze with silt, clayey nannofossil ooze, silty clay, silty clay with foraminifers, clay with silt, and clay. The occurrence of pteropods in several silty clay layers and the presence of dolomitized clay concretions in Section 172-1055D-6H-1 are noteworthy. Unit II (~80 to ~128 mbsf; early Pleistocene) is composed of predominantly massive, structureless, and homogeneous dark greenish gray clay with siliceous, calcite-cemented burrow fills. Although nannofossils are present throughout Unit II, the nannofossil-rich layers found above are completely absent.

Fauna and flora at Site 1055 are rich and diverse. Calcareous nannofossils and planktonic foraminifers are abundant and well preserved, whereas benthic foraminifers are rare to few but well preserved. Diatoms are less abundant than at Site 1054 and exhibit moderate to good preservation. Paleomagnetic results indicate that the upper 100 m of core from Hole 1055B appear to lie within the Brunhes Chron, although below this level the magnetization signature is difficult to interpret because of drilling overprints and weak magnetizations. Sedimentation rates, based on six calcareous nannofossil and planktonic foraminifer events, increased with decreasing age from 30 m/m.y. for the interval from ~1.3 to ~1.0 Ma, to 79 m/m.y. for the interval from ~1 to ~0.5 Ma, and to ~120 m/m.y. for the past 0.5 m.y. Multisensor track (MST) investigations document that recovery was complete over the entire sequence (0–129 mbsf), with good overlap across core breaks.

Calcium carbonate content fluctuates between 34 and 67 wt%, with an average value of 48 wt%, and gradually decreases. The carbonate cycles probably reflect glacial/interglacial fluctuations. TOC varies between 0.3 and 2.10 wt%. Organic C/N values lie mainly between ~5 and 35, with an average value of 6, and are indicative of predominantly marine organic material. Results of Rock-Eval analysis indicate that organic matter is thermally immature with respect to petroleum generation.

Pore-water profiles from Site 1055 are typical of sediments in which sulfate reduction and methanogenesis occur. Sulfate concentrations decrease from the seawater value at the top of the core to values less than 1 mM at ~25 mbsf. The shallower and thinner sulfate reduction zone in Site 1055 compared to Site 1054 is probably due to the labile nature of the sedimentary organic matter at Site 1055. The onset of the methanogenic zone occurs at ~25 mbsf, in coincidence with sulfate depletion. High C_1/C_2 values and the absence of a major contribution of higher molecular-weight hydrocarbons suggest that the source for methane is most likely in situ bacterial methanogenesis resulting from decomposition of organic matter in the sediments. Although Site 1055 is located in a well-characterized gas hydrate area, gradients of chloride are absent, suggesting that no gas hydrate was recovered.

BACKGROUND AND OBJECTIVES

Sites 1054 and 1055 are located on the Carolina Slope and form the shallow end-members of a paleoceanographic depth transect of cores extending down the Blake Outer Ridge and over to the Bahama Outer Ridge (Fig. 1). Site 1054, at a water depth of 1281 m, is ~2 km from the headwall scarp of the Cape Fear Slide, one of the largest and best documented continental margin slide features in the world (Dillon et al., 1982). Site 1055 is on the lower CS at a water depth of 1798 m, and is 24 km south of Site 1054.

The Carolina Slope and Rise include additional structures such as the Carolina Trough and diapirs, and the region is known for the extensive presence of marine gas hydrate (see Paull, Matsumoto, Wallace, et al., 1996). CS sites were selected based on U.S. Geological Survey (USGS) long-range scan sonar (GLORIA) results, which were interpreted as evidence of smooth topography with hemipelagic sedimentation (GLORIA, EEZ-SCAN 87 Scientific Staff, 1991). This interpretation was found to be consistent with site survey (*Knorr* cruise 140/2) 3.5-kHz profiling and gravity coring. Stable isotope and radiocarbon dating of gravity cores near Sites 1054 and 1055 showed Holocene and Pleistocene sedimentation rates to be 670 m/m.y. and ~300 m/m.y., respectively (L. Keigwin, unpubl. data). Sedimentation on the CS may be similar to slope regions to the north in the Mid-Atlantic Bight. That region is marked by a depocenter of high (1%–

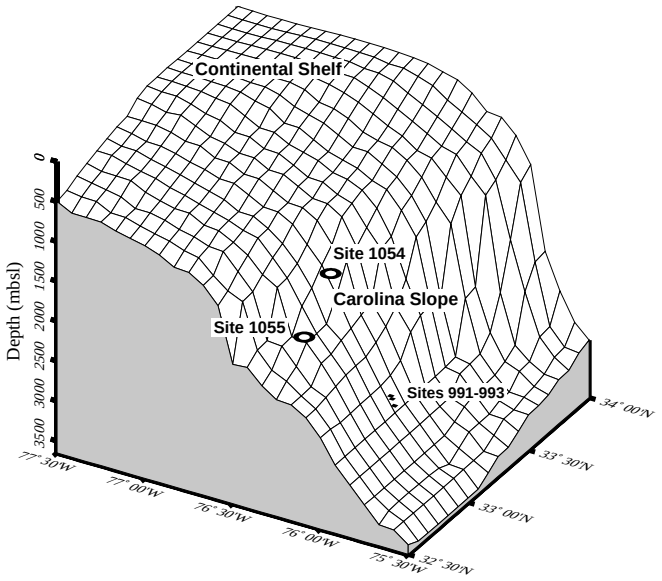

Figure 1. Locations of Sites 1054 and 1055 on a bathymetric relief map constructed from the ETOPO-5 data in the GMT software package (Wessel and Smith, 1991).

2%) organic carbon content and by sedimentation rates of several hundred meters per million years, and has been studied extensively by members of the Shelf Edge Exchange Program (SEEP) (Biscaye and Anderson, 1994). Seismic data on the CS show at least 1000 m of accumulation, with a prominent bottom-simulating reflector (BSR) that is present at the base of the gas hydrate stability zone.

Presently, the environment overlying the CS is influenced by the Gulf Stream and by the shallowest waters of the Deep Western Boundary Current (DWBC), which are thought to originate in the southern Labrador Sea (Pickart and Smethie, 1993). During glacial times, when the production rate of the lower component of North Atlantic Deep Water (NADW) decreased and the upper component increased (Boyle and Keigwin, 1987; Oppo and Fairbanks, 1987; Lehman and Keigwin, 1992), Sites 1054 and 1055 were probably influenced by glacial North Atlantic Intermediate Water (NAIW). The presence of high-latitude clay mineralogies and red sediments of Nova Scotian origin on the CS could be advective tracers for the flow of intermediate-depth waters (Heezen et al., 1966; Hathaway, 1972).

The objectives of drilling at Sites 1054 and 1055 were (1) to monitor the shallowest reaches of Upper NADW in Pleistocene time, (2) to provide high-resolution sections for paleomagnetic study, and (3) to provide sections for studying geochemical processes related to gas hydrate formation and dissociation. In addition, the sedimentary record recovered at Site 1055, together with those of Sites 1054 and 1056, may prove useful for testing models of continental slope sedimentation during glacial lowering of sea level.

OPERATIONS

The *JOIDES Resolution* departed Charleston, South Carolina, at 1900 hr (local time) on 18 February 1997. The *JOIDES Resolution* slowed at 0700 hr on 19 February to deploy and test new seismic gear, which included a generator-injector (GI) air gun, on loan from Seismic Systems, Incorporated, and two new multichannel seismic streamers produced by Innovative Transducers, Incorporated. By 1200 hr, we began a 46-km-long seismic survey over the first two drill sites—Sites 1054 and 1055. Very good seismic images were obtained using a combination of the GI gun source and the Teledyne single-channel oil-filled streamers, the latter of which are due to be replaced by the new multichannel streamers. Unfortunately, the first

Table 1. Coring summary for Sites 1054 and 1055.

Core	Date (Feb. 1997)	Time (UTC)	Interval (mbsf)	Length cored (m)	Length recovered (m)	Recovery (%)
172-1054A-						
1H	20	0045	0.0-8.0	8.0	8.02	100.3
2H	20	0140	8.0-17.5	9.5	9.86	103.8
3H	20	0220	17.5-27.0	9.5	9.94	104.6
4H	20	0250	27.0-36.5	9.5	10.06	105.9
5H	20	0325	36.5-46.0	9.5	9.17	96.5
6H	20	0355	46.0-55.5	9.5	10.13	106.6
7H	20	0430	55.5-59.4	3.9	3.88	99.5
8H	20	0505	59.4-65.8	6.4	6.34	99.1
9H	20	0550	65.8-75.3	9.5	8.63	90.8
10H	20	0710	75.3-84.8	9.5	10.23	107.7
11X	20	0900	84.8-93.5	8.7	9.88	113.6
12H	20	0950	93.5-103.0	9.5	9.48	99.8
13X	20	1115	103.0-112.7	9.7	9.27	95.6
14X	20	1150	112.7-122.3	9.6	9.53	99.3
15X	20	1255	122.3-131.9	9.6	8.52	88.8
16X	20	1345	131.9-141.5	9.6	9.65	100.5
17X	20	1450	141.5-151.2	9.7	0.00	0.0
18X	20	1550	151.2-160.9	9.7	8.73	90.0
19X	20	1625	160.9-170.5	9.6	5.16	53.8
20X	20	1710	170.5-180.1	9.6	7.49	78.0
21X	20	1750	180.1-189.8	9.7	9.62	99.2
22X	20	1840	189.8-200.0	10.2	8.96	87.8
Coring totals:				200.0	182.55	91.3
172-1054B-						
1H	20	2105	0.0-2.7	2.7	2.69	99.6
2H	20	2155	2.7-12.2	9.5	9.75	102.6
3H	20	2220	12.2-21.7	9.5	9.77	102.8
4H	20	2300	21.7-31.2	9.5	9.61	101.2
5H	20	2340	31.2-40.7	9.5	9.55	100.5
6H	21	0020	40.7-50.2	9.5	9.83	103.5
7H	21	0105	50.2-56.9	6.7	6.68	99.7
8H	21	0200	56.9-66.4	9.5	9.82	103.4
9H	21	0230	66.4-75.9	9.5	10.17	107.1
10H	21	0300	75.9-85.4	9.5	10.04	105.7
11H	21	0335	85.4-94.9	9.5	10.11	106.4
12H	21	0405	94.9-103.2	8.3	8.27	99.6
Coring totals:				103.2	106.29	103.0
172-1054C-						
1H	21	0615	0.0-8.2	8.2	8.25	100.6
2H	21	0645	8.2-17.7	9.5	9.78	102.9
3H	21	0730	17.7-27.2	9.5	10.06	105.9
4H	21	0800	27.2-28.2	1.0	1.03	103.0
5H	21	0835	28.2-37.7	9.5	9.65	101.6
6H	21	0905	37.7-47.2	9.5	9.96	104.8
7H	21	0930	47.2-56.7	9.5	9.99	105.2
8H	21	1000	56.7-58.7	2.0	1.91	95.5
9H	21	1045	58.7-68.2	9.5	9.56	100.6
10H	21	1115	68.2-77.7	9.5	9.75	102.6
11H	21	1145	77.7-87.2	9.5	9.84	103.6
12H	21	1220	87.2-96.7	9.5	9.55	100.5
13H	21	1250	96.7-101.9	5.2	5.22	100.4
Coring totals:				101.9	104.55	102.6
172-1055A-						
1H	22	0035	0-9.5	9.5	9.82	103.4
Coring totals:				9.5	9.82	103.4
172-1055B-						
1H	22	0115	0.0-4.5	4.5	4.48	99.6
2H	22	0145	4.5-14.0	9.5	9.72	102.3
3H	22	0220	14.0-23.5	9.5	10.01	105.4
4H	22	0300	23.5-33.0	9.5	10.12	106.5
5H	22	0335	33.0-42.5	9.5	9.86	103.8
6H	22	0410	42.5-52.0	9.5	9.94	104.6
7H	22	0445	52.0-61.5	9.5	9.71	102.2
8H	22	0520	61.5-71.0	9.5	10.12	106.5
9H	22	0555	71.0-80.5	9.5	10.17	107.1
10H	22	0635	80.5-90.0	9.5	10.25	107.9
11H	22	0705	90.0-99.5	9.5	10.88	114.5
12H	22	0735	99.5-109.0	9.5	11.26	118.5
13H	22	0815	109.0-118.5	9.5	10.60	111.6
14H	22	0850	118.5-128.0	9.5	10.87	114.4
Coring totals:				128.0	137.99	107.8
172-1055C-						
1H	22	1040	0.0-8.5	8.5	8.52	100.2
2H	22	1110	8.5-18.0	9.5	9.60	101.1
3H	22	1145	18.0-27.5	9.5	9.63	101.4
4H	22	1230	27.5-37.0	9.5	9.92	104.4
5H	22	1305	37.0-46.5	9.5	10.12	106.5
6H	22	1340	46.5-56.0	9.5	10.07	106.0
7H	22	1415	56.0-65.5	9.5	10.10	106.3
8H	22	1450	65.5-75.0	9.5	10.03	105.6
9H	22	1525	75.0-82.5	7.5	7.50	100.0
10H	22	1610	82.5-92.0	9.5	10.30	108.4
11H	22	1645	92.0-101.5	9.5	10.28	108.2
12H	22	1720	101.5-111.0	9.5	9.31	98.0
13H	22	1755	111.0-120.5	9.5	10.42	109.7
14H	22	1835	120.5-120.8	0.3	0.30	100.0
Coring totals:				120.8	126.10	104.4
172-1055D-						
1H	22	2050	0.0-5.6	5.6	5.64	100.7
2H	22	2125	5.6-15.1	9.5	9.41	99.1
3H	22	2205	15.1-24.6	9.5	9.98	105.1
4H	22	2245	24.6-34.1	9.5	9.98	105.1
5H	22	2330	34.1-43.6	9.5	9.92	104.4
6H	23	0005	43.6-53.1	9.5	10.17	107.1
7H	23	0045	53.1-62.6	9.5	10.13	106.6
8H	23	0120	62.6-72.1	9.5	10.20	107.4
9H	23	0155	72.1-81.6	9.5	10.19	107.3
10H	23	0230	81.6-91.1	9.5	10.20	107.4
11H	23	0305	91.1-100.6	9.5	10.23	107.7
12H	23	0345	100.6-110.1	9.5	10.15	106.8
13H	23	0420	110.1-119.6	9.5	10.50	110.5
14H	23	0455	119.6-129.1	9.5	10.29	108.3
Coring totals:				129.1	136.99	106.1
172-1055E-						
1H	23	0700	0.0-8.5	8.5	8.53	100.4
2H	23	0730	8.5-18.0	9.5	9.95	104.7
Coring totals:				18.0	18.48	102.7

Notes: UTC = Universal Time Coordinated. For each site, an expanded coring summary table for each hole that includes lengths and depths of sections and sampling comments is included on CD-ROM (back pocket, this volume).

of the two multichannel streamers failed when deployed; further testing was planned for later in the cruise (See "Site Geophysics" section, this chapter).

The total transit to Site 1054, including the seismic survey, was 156 nmi, which was traveled at an average speed of 9.9 kt. Drilling operations commenced at 1817 hr on 19 February. Very accurate survey and drilling positions were obtained because of the availability of the differential global positioning system (dGPS).

Site 1054

Three holes were drilled at Site 1054 using the advanced hydraulic piston corer (APC) system and, for the lower part of Hole 1054A, the extended core barrel (XCB) system. Cores 172-1054A-3H through 10H and 12H, 172-1054B-4H through 12H, and 172-1054C-3H through 13H, were oriented with the Tensor tool.

At Hole 1054A, the APC system reached 84.8 mbsf (Core 10H) with its usual high recovery rate (91%–108%), but failed to penetrate on the next try (Table 1). One XCB core was taken from 84.8 to 93.5 mbsf and penetrated a small hard claystone zone that was underlain by ooze. Piston coring resumed on the next core and advanced with a full stroke to 103.0 mbsf. When an attempt with another piston core failed to advance because of indurated sediments, the remainder of the hole was cored with the XCB.

After the vessel was offset ~30 m south of the initial hole, Hole 1054B was spudded at a depth of 1304.8 meters below rig floor (mbrf). APC coring advanced to refusal, which was at 103.2 mbsf. The vessel was offset another 30 m south, and Hole 1054C was cored to 101.0 mbsf. By 1700 hr on 21 February, the drilling equipment was secured and the vessel was underway on a 14-nmi transit to the next site.

Site 1055

Coring operations started at Site 1055 at 0025 hr on 22 February. All holes were APC cored with recovery ranging from 98% to 118% (Table 1). Cores 172-1055B-3H through 14H, 172-1055C-3H through 14H, and 172-1055D-3H through 14H were oriented with the Tensor

Table 2. XRD data for Sites 1054 and 1055.

Core, section, interval (cm)	Quartz	K-spar	Plagioclase	Clay	Calcite	Dolomite	Siderite	Aragonite	Pyrite	Comments
172-1054B-										
1H-1, 29	13	8	6	5	42	2	0	11	2	
2H-1, 70	22	5	2	5	45	3	1	7	3	
3H-1, 70	19	6	2	5	45	4	1	8	3	
4H-1, 104	19	6	4	4	46	3	0	9	3	
5H-2, 20	29	4	16	4	15	22	0	1	3	
6H-2, 20	30	2	15	3	35	2	0	3	3	
7H-2, 20	23	4	3	6	43	3	0	6	5	
8H-2, 20	33	3	6	4	36	1	0	3	6	
9H-1, 5	0	2	7	2	15	71	0	1	2	Nodule
9H-2, 18	21	4	7	5	36	12	0	3	6	
11H-2, 20	33	14	11	1	6	4	7	11	11	
13X-1, 64	7	1	2	3	17	67	0	0	2	Nodule
13X-1, 90	9	1	4	2	19	61	0	1	2	Nodule
172-1055C-										
1H-1, 4	43	3	7	6	22	8	1	2	3	
172-1055C-										
1H-1, 50	13	7	3	5	41	3	0	11	6	
172-1055B-										
2H-1, 130	41	3	7	6	20	8	1	2	4	
3H-1, 50	15	5	2	7	50	3	0	7	5	
172-1055C-										
3H-2, 47	29	12	18	4	24	4	0	3	2	
172-1055B-										
4H-1, 35	29	2	23	4	18	12	3	4	4	
172-1055C-										
4H-2, 20	30	4	3	6	37	1	0	6	6	
172-1055B-										
5H-1, 50	29	2	17	4	32	3	0	4	3	
172-1055C-										
6H-2, 103	16	4	4	5	52	2	0	6	6	
6H-6, 12	12	1	3	4	65	4	0	0	5	
172-1055B-										
10H-1, 83	18	4	4	7	48	2	0	6	6	
11H-1, 20	20	6	4	6	43	3	0	8	6	
172-1055C-										
12H-1, 51	41	2	12	6	23	8	1	1	2	
172-1055B-										
13H-3, 45	51	6	5	18	11	0	1	2	5	
14H-1, 20	19	3	5	4	34	24	0	4	4	

Notes: K-spar = potassium feldspar. All data shown are relative percentiles.

tool. The first core barrel in Hole 1055A contained 9.82 m of sediment and, therefore, did not give a reliable indication of the mudline depth. Thus, Hole 1055B was spudded ~15 m to the west, and the mudline was obtained in the first core, from which a seafloor depth of 1809.0 mbrf was estimated.

The vessel was offset ~30 m north of Hole 1055B, and Hole 1055C was spudded at a mudline depth calculated as 1809.0 mbrf. Hole 1055D was spudded ~30 m north of Hole 1055C at a mudline depth calculated as 1809.9 mbrf. The final two cores were collected at Hole 1055E, which is ~40 m north of Hole 1055D in order to have multiple copies of the glacial–interglacial transition recorded by the near-surface sediments at this site. The *JOIDES Resolution* was on its way to Site 1056 by 1145 hr on 23 February.

LITHOSTRATIGRAPHY

Sediments recovered at Sites 1054 and 1055 are predominantly nannofossil clay/mixed sediment ooze and silty clay with variable proportions of biogenic and siliciclastic components. Dominant lithologies at both sites include silty clay, clay with silt, and silty and clayey mixed sediments with diatoms, foraminifers, and nannofossils. Most of the lithologic variability in these sediments occurs as decimeter- to centimeter-scale variations in the proportion of biogenic material, detrital clay, and detrital silt.

The analytical processes used to define the primary lithostratigraphic units at Sites 1054 and 1055 are outlined in the "Explanatory Notes" chapter (this volume). X-ray diffraction (XRD) and smear-slide analyses reveal that quartz, inorganic calcite, dolomite, and aragonite dominate the detrital silt component and are concentrated in the silty layers (Table 2). Accessory iron sulfide minerals, commonly in the form of disseminated pyrite, are also ubiquitous at Sites 1054 and 1055. Calcium carbonate contents average 46.5 and 47.6 wt% for Sites 1054 and 1055, respectively. The most striking lithologic distinctions between the two sites are increased diatom-bearing sediments at Site 1054 and frequent grain-size variations. Site 1054 has a greater number of beds composed of normally graded silty clay with shell fragments and sharp lower contacts, whereas the coarser deposits from Site 1055 frequently have sharp upper contacts and scoured basal contacts.

Lithostratigraphic Units of Site 1054

Unit I

Intervals: 172-1054A-1H through 3H-1 (0–19.0 mbsf); 172-1054B-1H through 3H-4 (0–16.8 mbsf); 172-1054C-1H through 3H-1 (0–19.2 mbsf)
Age: Holocene to middle Pleistocene

Unit I consists primarily of clayey and silty mixed sediments. Color reflectance data (Fig. 2) show high-amplitude oscillations in lightness (data on CD-ROM, back pocket, this volume). This may be caused by variations in bulk percent carbonate, with high carbonate content correlated with high spectral reflectance L-parameter values. Similar large-scale variations in percent carbonate at Sites 1054 and 1055 suggest both lithologies can be assigned to the same unit.

Unit II

Intervals: 172-1054A-3H-1 through 14X (19.0–118.7 mbsf); 172-1054B-3H-4 through 12H (16.8–103.2 mbsf); 172-1054C-3H-1 through 13H (19.2–101.9 mbsf)
Age: middle Pleistocene to early Pleistocene

Unit II contains interbedded layers of two basic sediment types, a silty clay with varying minor biogenic components and a silty foraminifer sand. The silty clay contains a siliceous component composed of diatoms, silicoflagellates, radiolarians, and sponge spicules, and a biogenic carbonate component with foraminifers and less abundant nannofossils. In the coarse fraction, there is a rhythmic alternation downcore between grains that are dominantly quartz or dominantly aragonite and calcite. The silty foraminifer sand is episodically present at Site 1054 in relatively thin layers. The two sediment types in Unit II at Site 1054 contain little color variation, with the majority of the sediment being a dark greenish gray color (10Y 4/1, Munsell color number).

Unit III

Interval: 172-1054A-14X through 21X (118.7–198.8 mbsf)
Age: early Pleistocene to middle Pliocene

Unit III is composed solely of a mixed sediment with similar characteristics to Unit II but with higher percentages of clay. The boundary between Unit II and Unit III was chosen at the last downhole occurrence of the silt lithology.

Lithostratigraphic Units of Site 1055

Unit I

Intervals: 172-1055A-1H (0–9.5 mbsf); 172-1055B-1H through 10H (0–90.1 mbsf); 172-1055C-1H through 8H (0–75.0 mbsf); 172-1055D-1H through 8H (0–72.3 mbsf); 172-1055E-1H through 2H (0–18.0 mbsf)
Age: Holocene to early Pleistocene

Unit I sediments of Site 1055 are dominated by intercalated beds of nannofossil clay/mixed sediment with silt, clayey nannofossil ooze, silty clay, silty clay with foraminifers, clay with silt, and clay. Several distinct lithologies, such as silty clay with pteropods, also are present within the more common sediments. Generally, the abundance of clay increases with depth, but the frequent recurrence of several lithologies constrains these sediments to one unit. The color for all lithologies is fairly consistent, ranging from dark greenish gray (10Y 6/2) to light bluish gray (5B 7/1), depending on the relative fraction of clay, nannofossils, and other carbonate present. The high and variable organic carbon content may also influence color variation (see "Organic Geochemistry" section, this chapter). Sediment color also seems to be affected by diagenetic redox reactions, creating abrupt and frequent color transitions. As in Site 1054, dolomitized clay concretions are present (e.g., in Section 172-1055D-6H-1).

Unit II

Intervals: 172-1055B-10H through 14H (90.1–128.0 mbsf); 172-1055C-8H through 14H (75.0–101.9 mbsf); 172-1055D-8H through 14H (72.3–129.1 mbsf)
Age: early Pleistocene

At Site 1055, Unit II is best distinguished by the L-parameter spectrophotometry data, where a smaller amplitude in the oscillations reflects decreasing variability in weight percent carbonate (Fig. 2; see data on CD-ROM, back pocket, this volume). The sediments of Unit II are predominantly massive, structureless, and homogeneous dark greenish gray (10Y 4/1) clay with siliceous, calcite-cemented burrow fills. Most importantly, Unit II is completely devoid of nannofossil-rich sediments frequently observed in Unit I of Site 1055.

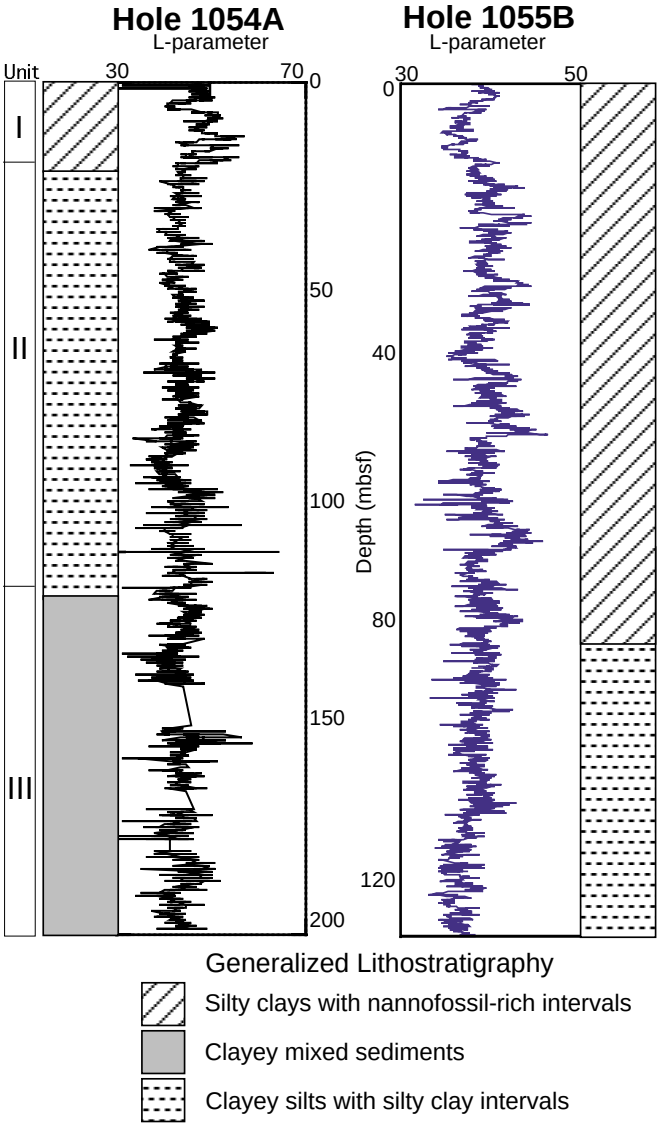

Figure 2. Color reflectance data and generalized lithostratigraphy for Sites 1054 and 1055. At Site 1054 the boundary between Units II and III at 118.7 mbsf is based on the absence of foraminifer sand below that depth. At Site 1055 the amplitude decrease in the color reflectance data at 74 mbsf reflects changes in the relative proportion of clays and carbonates.

Discussion and Interpretation

The consistent decrease in percent carbonate variability and similar lithologies at Sites 1054 and 1055 suggest Units I and II are of similar age at both sites. Lower bulk carbonate variations in Unit II may result from the diminution of several competing influences: (1) dilution of biogenic and inorganic calcium carbonate by siliciclastic material, (2) dissolution of calcium carbonate by respiration-derived carbonic acid in interstitial waters, or (3) decreased precipitation of biogenic calcium carbonate in highly productive surface waters. Percent carbonate variation may also be affected by recrystallization of calcite cements under sufficient overburden pressure.

Several interesting sedimentary features are common at Site 1054. The first occurrence of a calcite-cemented, siliceous burrow fill containing abundant diatom fragments and spicules is observed in Section 172-1054A-7H-2. Decimeter-scale light greenish gray dolomitized clay concretions are also found in Cores 172-1054A-8H, 9H, and 13X (Fig. 3). These structures indicate the occurrence of late diagenetic reactions, and the close association of intergranular dolo-

mite cement and iron sulfide minerals suggests an anaerobic origin for cementation (Berner, 1984).

Another important lithologic feature of Site 1054 are beds of clayey mixed sediment coarsening downsection and terminating in foraminifer sand (Table 3). The basal contacts of these beds are sharp and commonly scoured, whereas the upper contacts are often gradational, bioturbated, and poorly defined. Both contacts commonly contain mud clasts and laminated layers of finer and coarser sediments. The laminated layers often appear to have been folded. A photograph (Fig. 4) of interval 172-1054B-10H-3, 87–118 cm, shows a representative fining-upward deposit with a scoured basal contact and mud clasts near both contacts. Sediments above and below the thin layers of foraminifer sand appear to have been deposited by pelagic sedimentation, whereas the coarser beds appear to originate from downslope processes and appear to mark intervals of sediment removal by slumping.

There are two major zones of repeated mass-transport deposits and sediment removal in Site 1054. The first zone begins in the first core of all three holes and continues down through Sections 172-1054A-3H-4, 172-1054B-2H-7, and 172-1054C-2H-6. The second zone begins in Section 172-1054A-9H-2, and the events increase in frequency down to Section 13X-5, after which there is a mass-transport interval in each section until Section 14X-4. These intervals are also contained in Core 172-1054B-10H and in Cores 172-1054C-11H through 13H. Hole 1054A has more mass-transport intervals (as many as 20 were observed) than Hole 1054B or 1054C, and Hole 1054C has more than 1054B. This pattern suggests that the lithologies are correlatable, that deposit thickness and occurrence are spatially variable, and that Hole 1054A may have been nearest the mass-transport locus, whereas Hole 1054B may have been the most distal of the three holes.

Several lithologic features distinguish Site 1055 from Site 1054. First, a consistent, gradational color change from light greenish gray to pale red is found in Sections 172-1055B-1H-3 and 1H-4, and thin (2–4 cm) pteropod layers are often present in the same section. Second, the frequency of sharp, coarse intervals with scoured boundaries decreases markedly, with only one bed observed in interval 172-1055D-6H-1, 81–100 cm. Although the frequency of the scoured beds decreases, gradational, decimeter- to centimeter–scale coarse beds become increasingly common. The top contacts of these beds are frequently sharp and the basal contacts gradational, although this pattern may be an artifact of preferential bioturbation along the basal contact or winnowing at the upper contact. Within the coarsening–fining beds, the grain size change is consistent, ranging from silty clay or silt to clay or clay with silt.

The sedimentological characteristics of the foraminifer sand layers in Site 1054 are consistent with mass-transport deposits associated with sediment removal by slumping. Across these intervals, there are no age reversals in the biostratigraphic data, but the biostratigraphic evidence suggests decreased overall sedimentation rates in sections with larger numbers of foraminifer sand deposits. We interpret these observations as evidence for removal of sediment from Site 1054. Site 1055 contains similar coarse beds, but these deposits have characteristics of both mass wasting processes and contourite sedimentation. Biostratigraphic data for Site 1055 imply less marked inflections in sedimentation rate, suggesting the diminution of down-slope processes occurring at Site 1054. Lithologic similarity between the two sites, however, strongly suggests similar overall depositional histories for the observed time intervals.

Lithologic variability between the two sites accurately reflects patterns of sedimentation on continental margins. The consistent presence of pale red beds in the first cores of Site 1055 and their absence in Site 1054 may be explained by (1) the removal of glacial-age sediment at Site 1054 by increased margin slumping during sea-level minima above gas hydrate-bearing sediments (Paull et al., 1996), (2) high deposition rates at Site 1054 leading to slope failure, (3) reduction of Fe^{3+} oxides to soluble Fe^{2+} at Site 1054 as a result of large influxes of organic carbon, or (4) deposition of northern source sediments by geostrophic contour currents near the water depth of Site

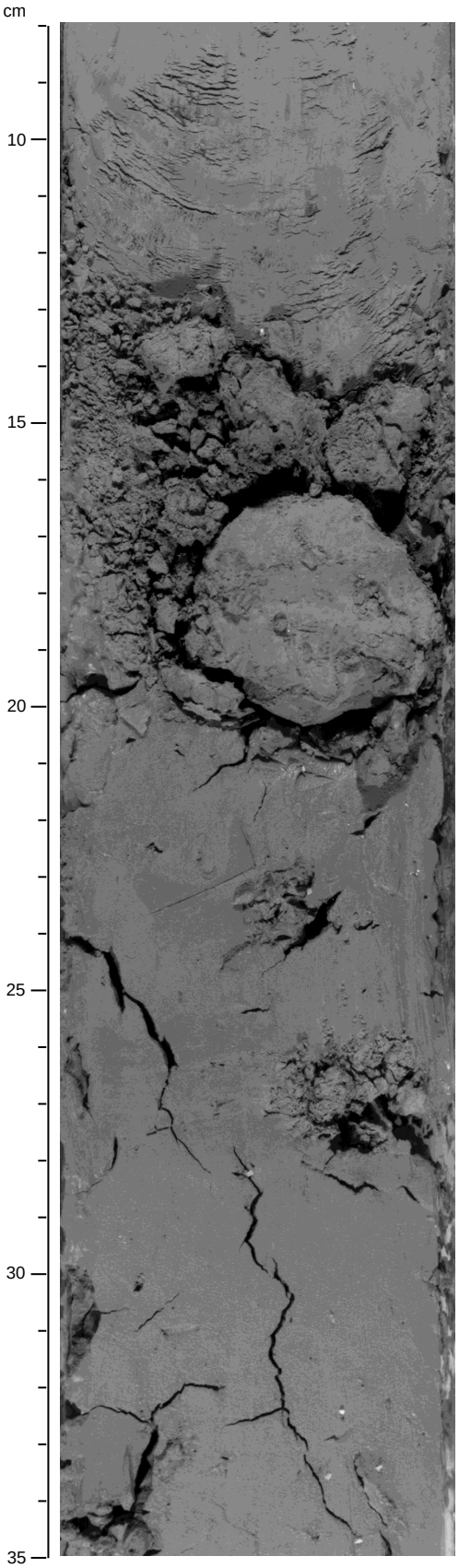

Figure 3. A dolomitized clay concretion in interval 172-1054A-8H-1, 16–20 cm, indicates the occurrence of late diagenesis reactions.

Table 3. Location of mass-flow deposits at Site 1054.

Core, section	Base depth (cm)
172-1054A-	
1H-5	120
2H-1	110
2H-3	134
2H-5	90
2H-7	44
3H-1	138
3H-4	120
6H-5	73
9H-2	74
10H-4	23
10H-6	140
10H-7	62
11X-2	107
12H-3	104
12H-4	120
12H-6	110
13X-2	130
13X-5	28
13X-6	140
13X-CC	18
14X-1	130
14X-2	133
14X-3	110
14X-4	110
172-1054B-	
2H-7	55
6H-1	126
6H-6	60
6H-7	43
10H-3	112
10H-5	60
10H-6	20
172-1054C-	
1H-5	45
2H-3	110
2H-6	3
5H-7	15
9H-4	89
11H-1	66
11H-1	140
11H-5	35
11H-6	114
13H-1	80
13H-1	103
13H-1	107

1055 (Heezen et al., 1966). Southward-flowing waters of southern Labrador Sea origin have recently been identified in the region of Sites 1054 and 1055 (Pickart and Smethie, 1993), supporting the fourth explanation. Although all hypotheses could explain the absence of the pale red beds at Site 1054, high-resolution stable isotope and carbonate stratigraphies could determine the absence or presence of glacial periods at Site 1054. Most importantly, Sites 1054 and 1055 demonstrate the influence of downslope transport and contourite sedimentation on the Carolina Slope.

BIOSTRATIGRAPHY

Biostratigraphic control at Sites 1054 and 1055 was provided by shipboard analyses of calcareous nannofossils and planktonic foraminifers. Nannofossils were examined from Holes 1054A, 1054B, 1054C, 1055B, 1055C, and 1055D, whereas planktonic foraminifer analyses were confined to Holes 1054A and 1055B. Faunal assemblage changes in benthic foraminifers were studied from Holes 1054A, 1054B, 1055B, and 1055C. Diatoms were examined in core-catcher sediments in Holes 1054A, 1054B, 1055B, and 1055C.

Within the resolution of the biostratigraphic datums, the sequence at Site 1054 is nearly complete from the late Pliocene to Holocene and at Site 1055 from the early Pleistocene to the Holocene. Although recovery was not complete (Figs. 5, 6), a composite section was spliced together from adjacent holes (see "Stratigraphic Correlation" section, this chapter).

Sixteen datums (nine planktonic foraminifer and seven nannofossil) were identified from Hole 1054A. Foraminifer datums were constrained to within 1.5 m and nannofossil datums to between 30 cm and 1.5 m. For Hole 1055B, six datums (three planktonic foraminifer

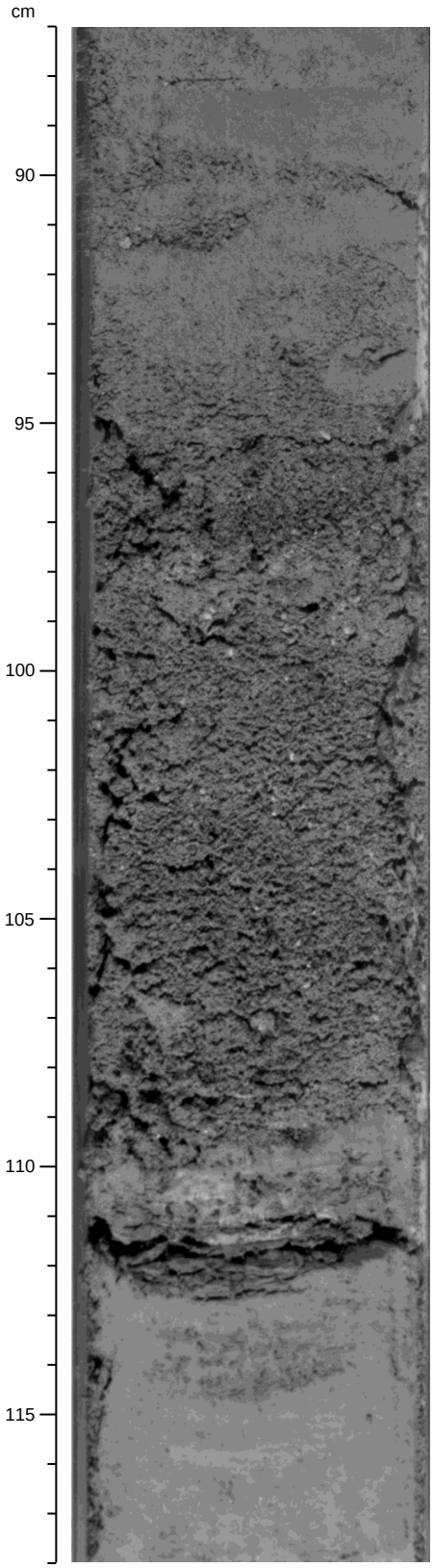

Figure 4. An example from Hole 1054B (interval 172-1054B-10H-3, 87–118 cm) of coarse- and fine-grained layered sediments with scoured basal contacts, indicating sediment removal, mass flow, and downslope transport.

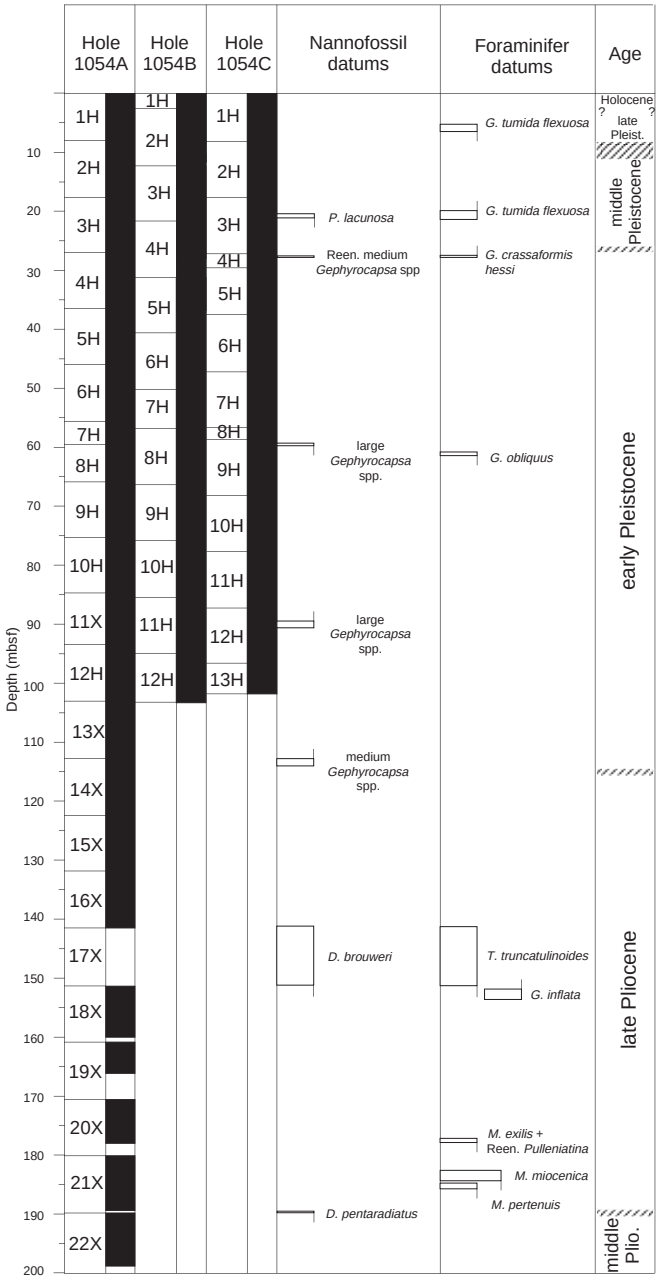

Figure 5. Core recovery and calcareous microfossil datum levels at Site 1054.

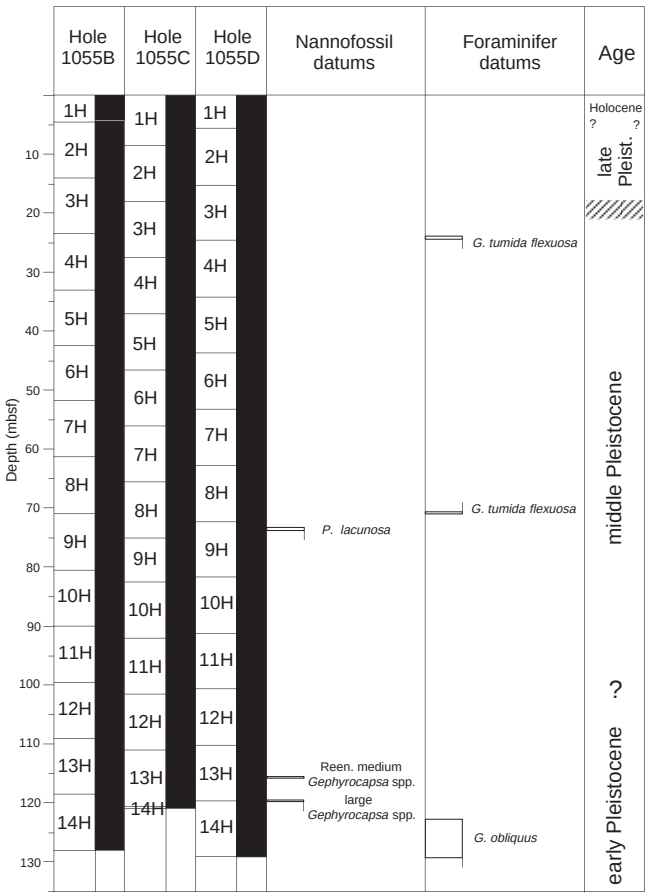

Figure 6. Core recovery and calcareous microfossil datum levels at Site 1055.

and three nannofossil) were considered reliable and constrained to the same extent as those at the shallower Carolina Slope site. Hole 1054A was cored to 198.37 mbsf, and core-catcher material in Core 172-1054A-22X (the bottom level) contained fossils that are associated with the middle Pliocene planktonic foraminifer Zone N21 and nannofossil Subzone CN12c. Hole 1055B was cored to 128 mbsf, and the bottom of the hole is in early Pleistocene planktonic foraminifer Zone N22 and nannofossil Subzone CN13b.

Calcareous Nannofossils

The biostratigraphic information preserved in the calcareous nannofossil floras at Sites 1054 and 1055 was investigated in smear slides from core-catcher samples and from samples within cores to obtain better constraint of the biohorizons.

The nannofossil biostratigraphy suggests some sediments at Site 1054 were probably removed by downslope transport processes during the late Pleistocene–Holocene (see Fig. 5; "Lithostratigraphy" section, this chapter). From 28 mbsf to the bottom of the hole, a continuous stratigraphic record from the lower Pleistocene to the upper Pliocene was recovered (approximately from the upper part of Subzone CN13b [~1 Ma] to the Subzone CN12d/CN12c boundary [~2.53 Ma]).

The section was studied in detail for Hole 1054A and part of Hole 1054B to constrain a few biohorizons, the results of which are presented in Table 4. The nannofossil assemblages show a generally rich diversity and are mostly well preserved and abundant. In a few samples of Cores 172-1054A-3H and 4H, the nannofossil assemblage is strongly reduced in numbers through "dilution" by biogenic fragments and clay particles, but preservation remains good so that biostratigraphic characterization is always possible. There is no evidence of severe sediment mixing, either through sedimentological processes or during the coring procedure. The short intervals that appear affected by downslope transport processes (see "Lithostratigraphy" section, this chapter) explain some of the inconsistencies observed in the nannofossil record, such as the anomalously short interval between the last occurrence (LO) of *Pseudoemiliania lacunosa* and the reentrance of medium-sized *Gephyrocapsa* spp. (Table 4).

The Pleistocene encompasses the interval from the top of the section to approximately the level of the first appearance (FAD) of medium-sized (≥4 µm) *Gephyrocapsa* spp. and the last appearance (LAD) of *Globigerinoides fistulosus*. In the interval between Cores 172-1054A-1H and 3H, *Emiliania huxleyi* was observed in abundances that indicate a position below marine isotope Substage (MIS) 5b. Core 3H contained the extinction of *P. lacunosa,* and therefore in-

Table 4. Calcareous microfossil datums for Holes 1054A and 1055B.

Event	ID	Age (Ma)	Core, section, interval (cm) Top	Core, section, interval (cm) Bottom	Depth (mbsf) Top	Depth (mbsf) Bottom	Depth (mbsf) Mean	Depth (mcd) Mean
172-1054A-								
T *G. tumida flexuosa*	F1	0.068	1H-4, 70-72	1H-5, 32-34	5.20	6.32	5.76	5.76
Reent. *G. tumida flexuosa*	F2	0.401	3H-2, 70-72	3H-3, 70-72	19.70	21.20	20.45	21.70
T *P. lacunosa*	N1	0.46	3H-3, 20	3H-3, 70-72	20.50	21.20	20.85	22.10
B *G. crassaformis hessi*	F3	0.75	3H-CC, 21-24	4H-1, 68-70	27.41	27.88	27.55	28.72
Reent. m. *Gephyrocapsa* spp.	N2	1.00	4H-1, 50	4H-1, 68-70	27.50	27.68	27.59	28.49
T large *Gephyrocapsa* spp.	N3	1.24	7H-3, 47	8H-1, 48	59.35	59.88	59.62	62.22
T *G. obliquus*	F4	1.3	8H-1, 68-70	8H-2, 68-70	60.08	61.58	60.83	63.43
B large *Gephyrocapsa* spp.	N4	1.58	11X-2, 69-71	11X-3, 69-71	89.39	90.89	89.89	91.94
B m. *Gephyrocapsa* spp.	N5	1.69	14X-1, 70-72	14X-2, 37	112.94	114.11	133.53	139.52
T *D. brouweri*	N6	1.95	16X-CC, 30-33	18X-1, 40	141.52	151.60	146.56	152.55
B *T. truncatulinoides*	F5	2.0	16X-CC, 30-33	18X-1, 70-72	141.52	151.90	146.71	152.70
B (common) *G. inflata*	F6	2.15	18X-1, 70-72	18X-2, 70-72	151.90	153.40	152.90	158.89
T *M. exilis*	F7	2.2	20X-5, 70-72	20X-6, 70-72	177.20	177.95	177.58	183.57
Reent. *Pulleniatina*	F8	2.3	20X-5, 70-72	20X-6, 70-72	177.20	177.95	177.58	183.57
T *M. miocenica*	F9	2.3	21X-4, 70-72	21X-5, 70-72	184.86	185.72	185.29	191.28
T *D. pentaradiatus*	N7	2.52	21X-CC, 33-37	22X-1, 20	189.69	189.89	189.79	195.78
T *M. pertenuis*	F10	2.6	21X-3, 70-72	21X-4, 70-72	182.86	184.86	183.86	189.85
172-1055B-								
T *G. tumida flexuosa*	F1	0.068	2H-CC, 15-18	3H-1, 27-30	14.19	14.70	14.45	15.99
B *G. tumida flexuosa*	F2	0.401	8H-CC, 21-24	9H-1, 70-72	71.59	71.70	71.65	79.81
T *P. lacunosa*	N1	0.46	9H-2, 70-72	9H-2, 116-117	73.20	73.66	73.43	81.94
Reent. m. *Gephyrocapsa* spp.	N2	1.00	13H-6, 39-40	13H-6, 70-72	115.65	115.96	115.81	131.41
T *Gephyrocapsa* spp	N3	1.24	14H-1, 39-40	14H-2, 39-40	119.17	119.32	119.25	136.98
T *G. obliquus*	F3	1.3	14H-4, 70-72	14H-CC, 43-46	122.73	129.34	126.04	143.77

Notes: Event abbreviations: T = top, B = base, Reent. = reentrance; m = medium sized. ID abbreviations: F = planktonic foraminifer datum, N = nannofossil datum. ID numbers correspond to those in Figure 27.

cludes the upper Pleistocene Subzone CN14a and CN14b boundary. Numerous large specimens (>5 µm) of the genus *Gephyrocapsa* with large central openings were observed in the interval above the extinction level of *P. lacunosa*. The overall large size, the exceptionally large central opening and the correspondingly narrow rim distinguish this morphotype from other members of the *Gephyrocapsa* assemblage. This form was described in the same stratigraphic interval at ODP Leg 154 sites (Curry, Shackleton, Richter, et al., 1995). The biostratigraphically important large *Gephyrocapsa* morphotypes (>5.5 µm) of the lower Pleistocene are clearly distinguished from the upper Pleistocene *Gephyrocapsa omega* morphotypes *sensu* Bukry (1973, pl. 3, figs. 5–11) by a wider rim and by the orientation of the bridge spanning the central opening. *P. lacunosa* shows a sharp final decline in abundance that can be determined precisely in Core 172-1054A-3H. The well-established succession of Pleistocene gephyrocapsid events, which relies largely on taxonomic subdivision into three size classes (Raffi et al., 1993), was observed. The reentrance of medium-sized forms occurs in Core 172-1054A-4H. The range of large forms (>5.5 µm) is between Sections 172-1054A-7H-CC and 11H-CC, and Sections 172-1054B-7H-CC and 10H-CC. The first occurrence (FO) of medium-sized forms is in Core 172-1054A-14H. The LO of *Helicosphaera sellii* was observed in the middle of the range of large *Gephyrocapsa*. The position of this biohorizon is in accordance with the results from the Ceara Rise (Leg 154; Curry, Shackleton, Richter, et al., 1995), where its calibration is "older" than estimates derived from the mid- to high-latitude North Atlantic and Mediterranean (near the top of the range of large gephyrocapsids; see discussion in Raffi et al., 1993). The rare and scattered presence of specimens of *Calcidiscus macintyrei* make it impossible to precisely delimit its LO.

Upper Pliocene sediments were recorded in core from the bottom of the Hole 1054A, and correspond to the interval between the successive extinctions of *Discoaster brouweri* and *Discoaster pentaradiatus*. The absence of *Discoaster surculus* in the oldest sediment cored at Site 1054 makes it possible to constrain the age to ~2.53 Ma.

Calcareous nannofossils are common to abundant throughout the sediments cored at Site 1055. The biostratigraphic resolution offered by nannofossils indicates that the continuously cored sections from Site 1055 are complete. The observed assemblages indicate ages that range from the Holocene to the late part of early Pleistocene (from Zone CN15 to Zone CN13, upper part). The results from the biostratigraphic investigations are presented in Table 4 and Figure 6. Most nannofossil events in Hole 1055B were determined to within 0.4–0.8 m. The upper Pleistocene biohorizons, the FO of the *Emiliania huxleyi* acme, and the FO of the *E. huxleyi* range cannot be accurately detected because of the small size of the marker (1–2 µm). *P. lacunosa* becomes extinct within Core 172-1055B-9H. The gephyrocapsid group is rich and well diversified and dominates the nannofossil assemblage together with *P. lacunosa*. Large *Gephyrocapsa* morphotypes (>5.5 µm) and *H. sellii* are consistently present at the bottom of the Site 1055 stratigraphic section (Core 172-1055B-14H), and this constrains the age of the oldest sediments recovered to the time interval between 1.25 and 1.58 Ma.

Planktonic Foraminifers

The FO and LO of *Globorotalia tumida flexuosa* (0.068 and 0.401 Ma) were the first two planktonic foraminifer datums to be delimited at both sites (see Table 4 for sample and mbsf levels of all datum horizons). The *flexuosa* variety occurs with the *Globorotalia tumida tumida* form, but is easily distinguished by the pronounced flexure of the keel on the final chamber. The FO of *Truncorotalia crassaformis hessi* (0.75 Ma) is not as reliable as the previously mentioned datums. This variety is identified by a kummerform final chamber that has a smoother texture than the more pustulose earlier chambers of the final whorl, and its spiral surface is often not parallel with those of previous chambers. The form is uncommon, and its sporadic occurrence makes constraining the bottom of its range problematic. The LO of *Globigerinoides obliquus* (1.3 Ma) is made difficult by the rarity of this taxon at the top of its range and the presence of occasional specimens of *Globigerinoides ruber* that have final chambers added obliquely (i.e., with the aperture over a chamber, rather than a chamber suture). Irregular specimens of *G. ruber* may be distinguished from *G. obliquus* by examination of the aperture position on the penultimate chamber, which is always in the characteristic orientation.

The base of Zone N22 is delimited by the FO of *Truncorotalia truncatulinoides* (2.0 Ma). This datum is diachronous between the southwest and tropical Pacific (Dowsett, 1988), but appears to be isochronous within the tropics (Chaisson and Leckie, 1993; Chaisson and Pearson, 1997). The LO of *D. brouweri* (1.95 Ma) is found im-

mediately above the FO of *T. truncatulinoides*, suggesting that the latter datum is isochronous between the tropics and the western subtropical Atlantic.

The reentrance of *Globoconella inflata* into the North Atlantic record is given as 2.06 Ma (an average of ranges determined at Deep Sea Drilling Project [DSDP] Sites 606 and 607) by Weaver and Clement (1987), adjusted to 2.15 Ma according to the time scale of Lourens et al. (1996). Initial results suggest that this event is also identifiable in the western subtropical Atlantic. The reentrance of *Pulleniatina* into the Atlantic record at 2.3 Ma appears to be slightly delayed in the subtropical western Atlantic, as it is well above the LO of *Menardella miocenica* (2.3 Ma) in Hole 1054A.

The late Pliocene extinctions of *Menardella exilis, M. miocenica,* and *Menardella pertenuis* (2.2, 2.3, and 2.6 Ma, respectively) are all recorded at Site 1054. Nannofossil data indicate that the deepest sediments at Site 1054 are ~2.5 Ma, which means that *M. pertenuis* should not be observed. However, ages for the menardellid datums that were derived using an orbitally tuned time scale at the Ceara Rise in the western tropical Atlantic (Chaisson and Pearson, 1997) differ from the published ages (Berggren et al., 1995). At Ceara Rise, *M. exilis* was found to persist until 2.1 Ma and *M. pertenuis* until 2.3 Ma, which is later than the published age. By contrast, the LO of *M. miocenica* at Ceara Rise was slightly earlier (2.4 Ma) when compared to the published age. The datums appear to be diachronous. The order of the menardellid extinction noted at the Ceara Rise is repeated here, but if the nannofossil datums (LO of *D. brouweri* and LO of *D. pentaradiatus*) are isochronous between the Ceara Rise and the Blake Outer Ridge, then the menardellid globorotaliids disappear somewhat earlier in the subtropics than in the tropical Atlantic.

Benthic Foraminifers

Benthic foraminifers were studied mainly in core-catcher samples from Holes 1054A and 1054B and from Holes 1055B and 1055C. In addition, some samples from within the cores were examined to better constrain the levels of major faunal changes. At both sites, samples are characterized by the presence of abundant but small *Bolivina* spp. and *Epistominella exigua,* which suggests sorting during transport by bottom currents.

At Site 1054 benthic foraminifers are common and well preserved, except in Sections 172-1054A-13X-CC through 15X-CC, where preservation is poor and benthic foraminifers are rare or absent (Section 15X-CC). Two major faunal changes are recognized within the recovered section. The first transition takes place between Sections 2H-CC and 3H-CC and is marked by a large increase in the numbers of infaunal species, with a predominance of deep infaunal ones. In Samples 172-1054A-1H-CC and 2H-CC and 172-1054B-1H-CC and 2H-CC, the benthic foraminifer fauna is characterized by high overall abundances of *Cassidulina carinata* and by fluctuations in the abundances of *Bulimina marginata, Gyroidinoides soldanii,* and *Globobulimina affinis.* The dominance of *C. carinata* may be linked to well-oxygenated, fast-moving bottom waters. Changing abundances of infaunal (*B. marginata* and *G. affinis*) vs. epifaunal (*G. soldanii*) species may be limited to changing oxygen contents. In Cores 172-1054A-3H through 12H the most common species are *Chilostomella oolina* and *G. affinis,* with lower numbers of *Fursenkoina mexicana, B. marginata,* and *Stilostomella* spp. The relative abundances of these species show very large fluctuations. In Core 172-1054A-10H *Cibicidoides wuellerstorfi* is found, and in Core 12H *Hoeglundina elegans* is common. The second transition is between Sections 172-1054A-12H-CC and 16X-CC. In Cores 172-1054A-16X through 22X, the main benthic foraminifer faunal components are *Uvigerina senticosta, C. wuellerstorfi, Cibicidoides pachyderma, H. elegans, Bulimina costata,* and *Gyroidinoides* spp. This interval is also characterized by recurrent fluctuation of faunal abundances.

Table 5. Distribution of diatoms in Holes 1054A and 1055B.

Core, section	Presence of diatoms
172-1054A-	
1H-CC	A - fragments/R - whole
2H-CC	F - fragments
3H-CC	F - fragments
4H-CC	A - fragments and whole
5H-CC	A - fragments and whole
6H-CC	A - fragments/F - whole
7H-CC	A - fragments/F - whole
8H-CC	A - fragments/F - whole
9H-CC	A - fragments and whole
10H-CC	F - fragments
11X-CC	A - fragments and whole
12H-CC	A - fragments/F - whole
13X-CC	F - fragments
14X-CC	A - fragments/F - whole
15X-CC	Barren
16X-CC	C - fragments/R - whole
17X-CC	No recovery
18X-CC	C - fragments/R - whole
19X-CC	A - fragments/F - whole
20X-CC	C - fragments/R - whole
21X-CC	A - fragments/F - whole
22X-CC	A - fragments/F - whole
172-1055B-	
1H-CC	Barren
2H-CC	F - fragments
3H-CC	Barren
4H-CC	F - fragments
5H-CC	F - fragments
6H-CC	R - fragments
7H-CC	R - fragments
8H-CC	R - fragments
9H-CC	R - fragments
10H-CC	F - fragments and whole
11H-CC	X - fragments
12H-CC	F - fragments and whole
13H-CC	A - fragments and whole
14H-CC	A - fragments and whole

Note: Quantity abbreviations: X = scarce, R = rare, F = few, C = common, A = abundant.

At Site 1055 benthic foraminifers are well preserved, but are rare or few in number. No major faunal fluctuations occur within the recovered succession, except for a slight increase in the relative abundance of *Globobulimina* in Core 172-1055B-9H. The main components of the benthic fauna are *C. carinata, B. marginata, Gyroidinoides* spp., and *Valvulineria laevigata.* Minor abundance changes of *Globocassidulina subglobosa, Oridorsalis umbonatus,* and some cibicidoids were, however, observed. In some samples from Site 1055, benthic foraminifers are rare and poorly preserved. In these samples, the fauna contain small numbers of several species, but *Bolivina* spp. and *Epistominella exigua* are most commonly encountered.

Diatoms

Diatoms were briefly examined from Holes 1054A, 1054B, 1055B, and 1055C. Results of this study should be considered preliminary, as only the core catchers were examined. Diatoms are abundant and well preserved in the following core catchers: Samples 172-1054A-4H-CC, 5H-CC, 6H-CC, 9H-CC, 11X-CC, 12H-CC, and 14X-CC; 172-1054B-4H-CC and 5H-CC; 172-1055B-13H-CC and 14H-CC; and 172-1055C-6H-CC, 13H-CC, and 14H-CC. The remaining core catchers from each site contained either fragments or no diatom remains at all. Samples barren of diatomaceous material were more numerous at Site 1055 (Table 5).

Samples with sufficient diatom preservation were found to be within the *Nitzschia reinholdii* Zone at both sites. All samples contained *N. reinholdii* as well as *Pseudoeunotia doliolus,* constraining them to the period between 0.65 and 1.8 Ma (Baldauf, 1984; Barron, 1985). These data agree with both nannofossil and planktonic foraminifer datums. Poor preservation at the top and bottom of Hole

1054A allowed only one zone to be delimited. Further examination of samples within the cores will improve the diatom biostratigraphy.

The assemblage of diatoms found at these two sites is a curious mixture of open-ocean species and coastal, benthic associations. It is uncertain whether this is caused by downslope transport or whether the local environment was suitable for in situ deposition. Because the sedimentological record includes some transport structures, the former explanation is deemed the most likely. Worth noting is the observation of reworked Eocene species in Sample 172-1055C-14H-CC. This would further support sediment transport from the continental shelf.

PALEOMAGNETISM

The natural remanent magnetization (NRM) of the archive-half sections from Holes 1054A (APC and XCB cores), 1054B, and 1054C (APC cores), and 1055A through 1055E (APC cores) was measured using the pass-through cryogenic magnetometer at a 5-cm interval. After measuring the NRM, most sections were partially demagnetized in peak alternating fields (AF) of 10 mT, and all sections were partially demagnetized at 20 mT with the aim of removing overprints to reveal the character of the geomagnetic field changes. More detailed AF demagnetization treatments up to 60 mT were conducted on a few sections to evaluate the demagnetization behavior of the sediments at higher fields. The data are given in Tables 6 through 17 on CD-ROM in the back pocket of this volume.

The NRM inclinations are almost always strongly biased toward high positive inclinations (70°–90°), which is inconsistent with the ~52° inclination expected for an axial dipole field at the latitude of these sites. The observed inclinations indicate that a magnetic overprint is present as identified during many previous DSDP and ODP legs. This secondary overprint is characterized by steep inclinations and is probably acquired during drilling.

Magnetic cleaning in peak fields of 20 mT appears to remove most of the overprint for the upper 75–100 m of core at each hole as evidenced by directional data downcore (Figs. 7, 8) and demagnetization behavior of discrete samples (Fig. 9). The magnetic intensity drops off rapidly with depth at both sites (Figs. 7, 8), probably because of dissolution (reduction diagenesis) of the initial magnetic minerals (probably magnetite). Some continuing magnetic mineral dissolution at depth (and perhaps enhanced when sulfate reduction is replaced by methanogenesis) is likely causing the remaining magnetic mineral fraction to become smaller in volume and coarser in grain size downhole at both sites because of loss of the high surface-area/volume, fine-grained magnetic material. The residual coarse-

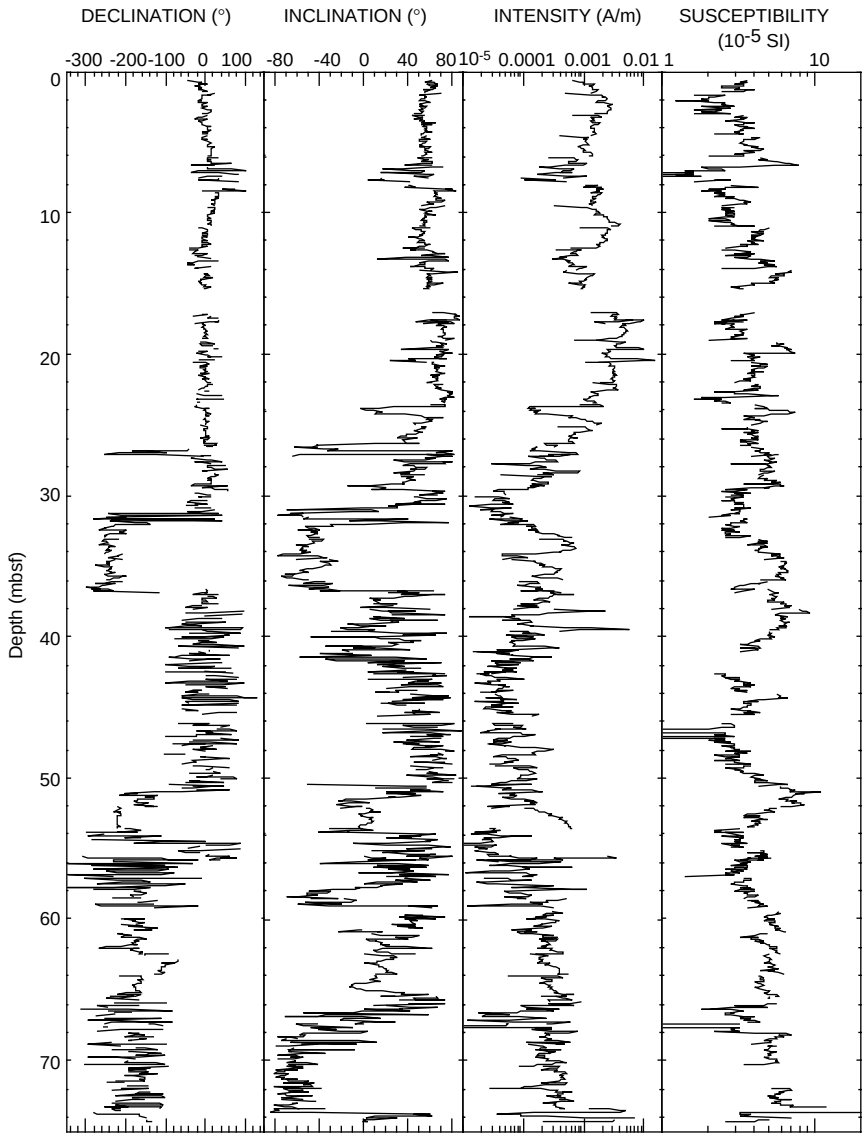

Figure 7. Downhole variation in the remanent magnetization direction and intensity after 20-mT demagnetization and in the susceptibility for Hole 1054A. For intervals interpreted to be normal polarity, the observed declinations were rotated such that the mean declination for the core was zero.

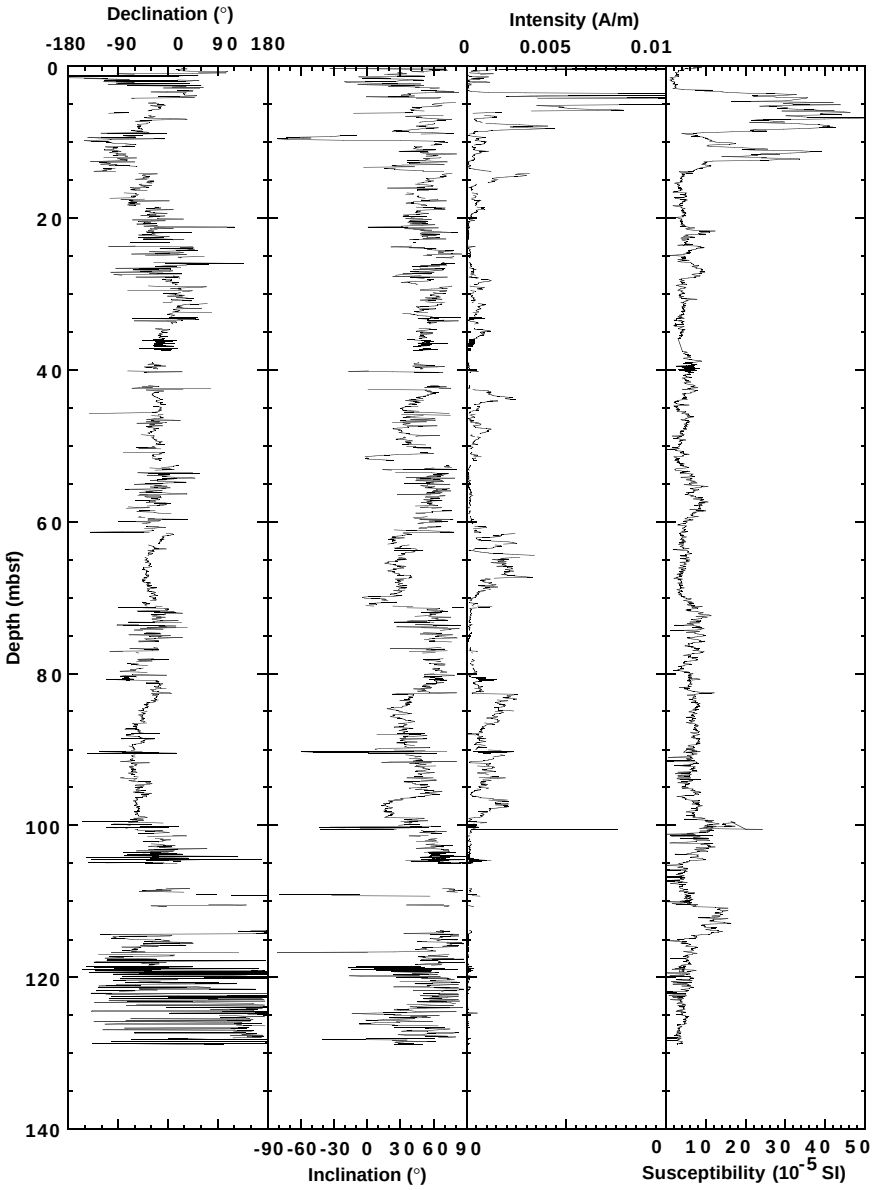

Figure 8. Downhole variation in the remanent magnetization direction and intensity after 20-mT demagnetization and in the susceptibility for Hole 1055B.

grained, multi-domain magnetic material would be more prone to acquiring a drill-string overprint.

Superimposed on the trend of decreasing intensity downhole are oscillations between high and low intensity. Neither the trend nor the oscillations are correlated to the variations in magnetic susceptibility, illustrating the very weak magnetization of these sediments. The susceptibility signal of the paleomagnetic minerals is almost entirely swamped by the susceptibility of the paramagnetic clays. The exception to this is between 3 and 9 mbsf at Site 1055, where reduction diagenesis had not dissolved away the magnetite.

Nevertheless, a potentially clean paleomagnetic signal was obtained for the top 35–55 m of Site 1054 and the top 100 m of Site 1055 (see below). Below these depths, the intensities are too weak and the overprint too strong for the results to be directly interpreted without further processing.

Orientation

The Tensor tool was used to orient the APC cores collected from these holes, starting with the third core at each hole, except for Hole 1054B where orientation started at the fourth core (Tables 14, 15, on CD-ROM, back pocket, this volume). The Tensor tool data were noisy at Site 1054, and the orientation data were not useful in aligning the declinations between cores. Better quality orientation data were collected at Site 1055 and proved to be more successful in aligning the declinations between cores. The corrected declinations for Hole 1055B average ~340° and exhibit large, coherent, easterly and westerly swings of up to 30°.

Discrete Sample Analysis

Oriented discrete samples (6-cm^3 plastic boxes) were collected from almost every core from Holes 1054A and 1055B. These samples were generally subjected to stepwise AF demagnetization up to 60 mT in order to assess the magnetic coercivity of the sediments and estimate a demagnetization level suitable to remove the secondary magnetization (Table 16, 17 on CD-ROM, back pocket, this volume). It is clear that a large (>60% of total NRM) magnetic overprint is present, which can be routinely removed by demagnetization to 20 mT (Fig. 9). Above 20 mT, the samples commonly decay toward the origin in a simple manner. With increasing depth, the effectiveness of the overprint removal diminishes. This may be due to an increasingly

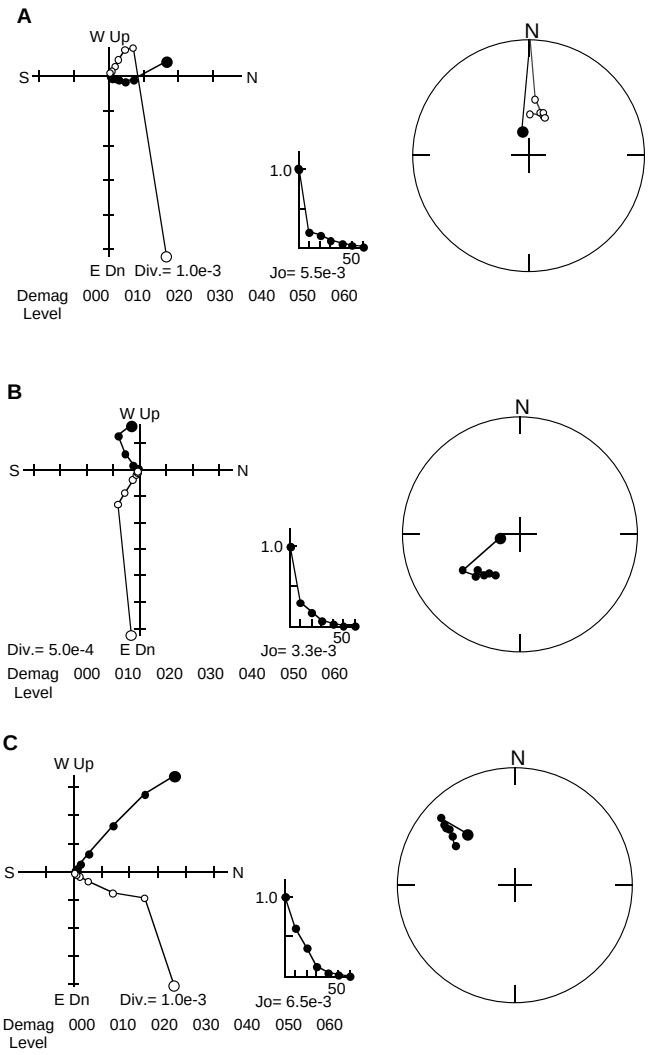

Figure 9. Typical NRM demagnetizations of selected discrete samples from (**A**) 172-1055B-2H-4, 40 cm, (**B**) 172-1055B-4H-6, 80 cm, and (**C**) 172-1055B-8H-4, 50 cm. Samples were progressively demagnetized up to 60 mT at 10-mT intervals.

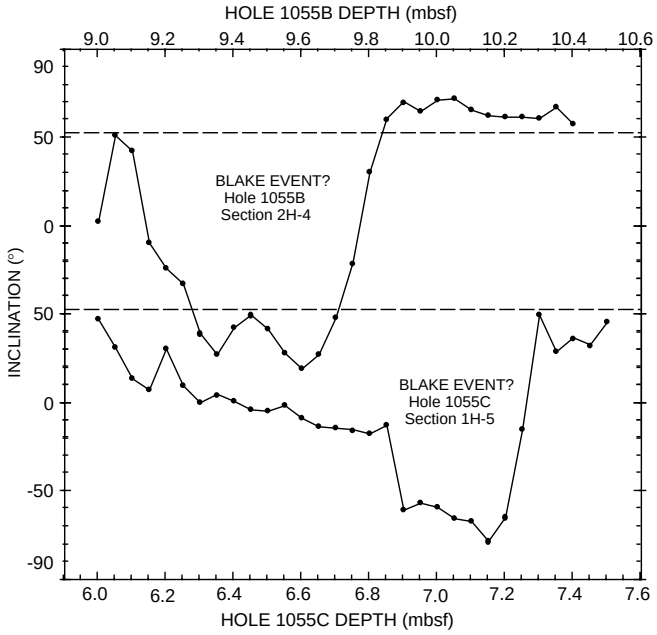

Figure 10. Inclination variation in Holes 1055B and 1055C over an ~1.5-m-long interval that records an excursion (?), which may be the Blake Event.

coarse overall magnetic grain size, which is easier to remagnetize, or to downhole addition of new chemical magnetic phases with higher coercivity.

Magnetic Polarity Stratigraphy

After magnetic cleaning of 20 mT, the remanent magnetization directions for Hole 1054A yield a distinctive magnetic polarity stratigraphy within the uppermost 75 m that is reproducible for Holes 1054B and 1054C (Fig. 7).

Our first interpretation is that the Brunhes Normal Polarity Chron (0–0.78 Ma) occurs from 0 to 31 mbsf, whereas the Matuyama Reversed Polarity Chron (0.78–2.58 Ma) extends from 31 to >75 mbsf. The Jaramillo Normal Polarity Subchron (0.99–1.07 Ma) within the Matuyama Chron occurs from 33.5 to 50.5 mbsf. There are intervals of normal polarity (?) inclination below the Jaramillo Subchron that could be related to the Cobb Mountain Subchron (1.20–1.21 Ma), but they could equally well be caused by an unremoved normal polarity overprint.

A second interpretation places the Brunhes/Matuyama boundary at 26 mbsf in Hole 1054A, with the Jaramillo between 27 and 31.5 mbsf. This interpretation gives only a short interval of reversed Matuyama polarity between the Jaramillo and the Brunhes. However, the equivalent interval from Hole 1054C is thicker (2 m), there is evidence of scour (see "Lithostratigraphy" section, this chapter), and the biostratigraphy indicates a very low sedimentation rate (see "Biostratigraphy" section, this chapter). Additionally, this interpretation lies closer to the biostratigraphic age-depth model than the first.

Below 75 mbsf in Hole 1054A (and similar depths in Holes 1054B and 1054C), the NRM diminishes in intensity and contains effectively random declinations with noisy, but biased toward normal polarity, inclinations. We interpret this lower interval to be completely overprinted and unsuitable for further paleomagnetic studies. The NRM in this interval seems to be very weak, but has higher coercivities suggestive of the chemical addition of a small amount of new magnetic minerals.

After magnetic cleaning at 20 mT, the sediments of Hole 1055B are of normal polarity and are interpreted to be from the Brunhes age. The mean directions are consistent with the expected geocentric axial dipole inclination at this site, although there is a tendency toward steeper inclinations. The unit vector mean direction has a declination of 343.5°, an inclination of 58.8°, a k of 14.2, and an $\alpha 95$ of 3.7°, for $N = 99$ measurements along a characteristic interval from Core 172-1055B-5H. The intensities average between 10^{-3} and 10^{-4} A/m down to a depth of ~100 mbsf. Below this depth the intensities drop to values averaging an order of magnitude weaker. At depths greater than ~100 m, increased inclination and declination dispersion may indicate that sediments of the Matuyama Reversed Polarity Chron are present, but that a normal overprint has not been effectively removed.

Excursions

A magnetic field excursion may be present at Site 1055 within the uppermost 10 mbsf of the sediment. Figure 10 shows the excursion inclination pattern within two core segments from Holes 1055B and 1055C. Figure 11 shows typical NRM demagnetizations through the excursion interval in Hole 1055B, which was identified based on several steps of long-core AF demagnetization. The normal polarity overprint seems to be easily removed, and the remaining reversed polarity inclinations demagnetize toward the origin. The position of this

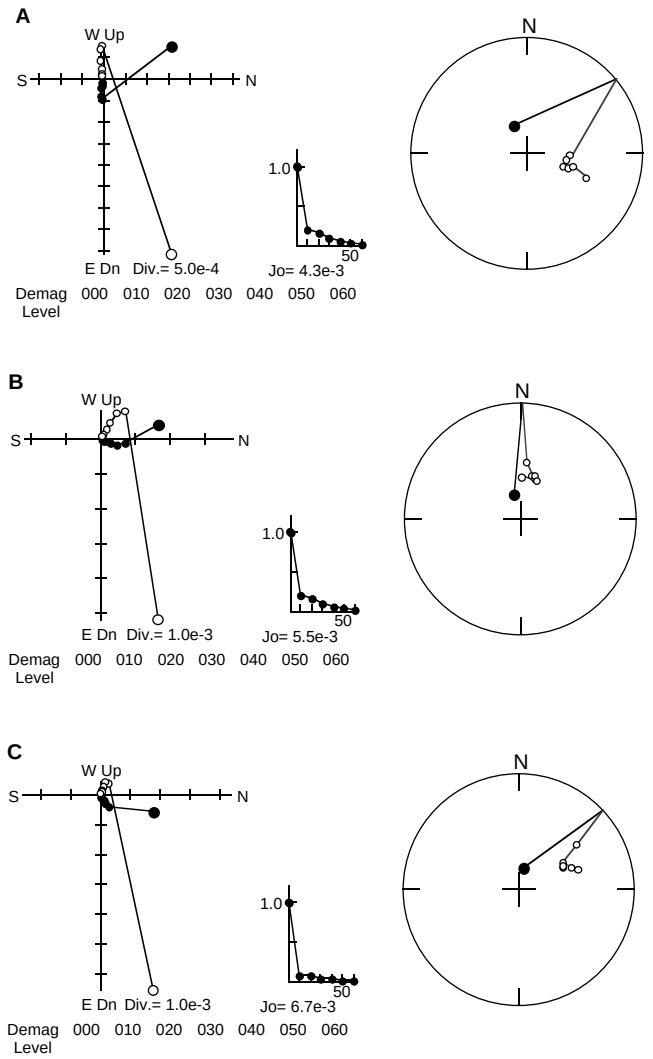

Figure 11. Demagnetization behavior of three samples in Section 172-1055B-2H-4 at (**A**) 30 cm, (**B**) 40 cm, and (**C**) 70 cm, which were progressively demagnetized to 60 mT at 10-mT steps. The results illustrate the removal of an overprint with a steep downward direction (the drill-string overprint) after 10 to 20 mT of AF demagnetization, after which stable reversed-polarity directions are present.

excursion indicates that it could be the Blake Event (~125 ka; Smith and Foster, 1969).

Another excursion may be present at Site 1054 just above the Brunhes/Matuyama boundary at ~23.5 m. The excursion (?) is identifiable in Figure 7 and is replicated in Hole 1054C. This interval may also represent the reversed interval between the Jaramillo Subchron and the Brunhes Chron.

COMPOSITE DEPTHS AND STRATIGRAPHIC CORRELATION

MST and color reflectance data collected for all holes at Sites 1054 and 1055 (and smoothed over a 31-cm window) were used to correlate between individual holes at each site, to determine depth offsets in the composite section, and to create spliced records. On the composite depth scale (meters composite depth [mcd]), features of the plotted MST and reflectance data present in adjacent holes are aligned so that they occur at approximately the same depth. Working from the top of the sedimentary sequence, a constant was added to the mbsf depth for each core in each hole to arrive at an mcd for that core. A spliced record for each site was created by combining intervals of the individual composite depth sections to create an overall stratigraphic section. Intervals having significant disturbance or distortion were avoided if possible. This information, along with the offsets suggested for individual core sections, can be used as a sampling guide to recover a single sedimentary sequence and to identify variability in cored records between sites. The depth offsets that comprise the composite depth section are given in Tables 18 and 19. Affine and splice tables appropriate for use in the Splicer program are on CD-ROM (back pocket, this volume). The integrity of the recovered sedimentary sequence could be documented for the upper 62 mcd (~60 mbsf) at Site 1054 (although correlative sequences cored below 62 mcd are cored in the different holes) and for the entire length cored at Site 1055 (to ~120 mbsf, although there are few features to correlate between cores at some depths).

Magnetic susceptibility and the color indexes lightness (L*) and chromaticity (a* and b*) were the primary parameters used for interhole correlation. Gamma-ray attenuation porosity evaluator (GRAPE) density was also examined in several instances to provide additional support for composite construction, but it is often noisy because of core expansion. Natural gamma-ray measurements and *P*-wave velocity measurements were not systematically made for all holes and were not used for correlation. The GRAPE records were used to identify voids (values less than 1.03 g/cm^3), and GRAPE data from these intervals were not used. No allowance was made, however, for core expansion resulting from large gas voids, decompression, or distributed small gas voids. Within the Splicer computer program, cores can only be shifted as a whole, even where hiatuses are thought to exist within a core. More precise correlation between holes will have to be undertaken post cruise based on additional data.

The magnetic susceptibility, GRAPE, and color indexes L*, a*, and b* used to verify core overlap are shown on a composite depth scale in Figures 12 through 16 for Site 1054, and in Figures 17 through 21 for Site 1055. The data used for correlation for each hole (with composite depths) and the spliced data at each site are on CD-ROM (back pocket, this volume). Also shown on each figure is a spliced record created by combining selected intervals of the composited cores. Spliced magnetic susceptibility and color reflectance (L*, a*, and b*) for Sites 1054 and 1055 are shown in Figures 22 and 23.

Site 1054

The chromaticity parameters a* and b* and the magnetic susceptibility appear well correlated between holes for the upper 62 mcd. As a result of core expansion, the mcd at Site 1054 is ~7% larger than the drilled depths (mbsf) above 118 mcd (Fig. 24). Deeper than 118 mcd, the mcd shows no expansion relative to mbsf because the section was cored only one time. Both GRAPE bulk density and lightness L* are less well correlated between sites, apparently because of cracks in the sediment and because carbonate-rich turbidites are somewhat different in character in different holes. There is a region of poor overlap between holes at ~62 mcd, resulting in a gap in the spliced record. This gap is apparently caused by a hard layer, as there is poor recovery in all holes at this depth. The poor correlation between Hole 1054A and Holes 1054B and 1054C from ~65 to 74 mcd is probably caused by lateral variability in lithology at this level and by a partial stroke and possible flow-in in Core 172-1054A-7H. Below 74 mcd, a correlation can be made between holes to the limit of multiple coring (~110 mcd), although the correlation is less robust. In particular, Hole 1054A appears to be missing part of the deeper section, from 74 to 78 mcd. The variable character of the deposit from 74 to 78 mcd and the missing section in Hole 1054A are apparently the result of an erosional unconformity (supported by paleontological evidence from

Table 18. Composite depths and depth offsets for Sites 1054 and 1055.

Core, section	Depth (mbsf)	Offset (m)	Depth (mcd)
172-1054A-			
1H-1	0.00	0.00	0.00
2H-1	8.00	–0.35	7.65
3H-1	17.50	1.25	18.75
4H-1	27.00	0.90	27.90
5H-1	36.50	1.75	38.25
6H-1	46.00	1.85	47.85
7H-1	55.50	2.60	58.10
8H-1	59.40	2.60	62.00
9H-1	65.80	–0.40	65.40
10H-1	75.30	1.75	77.05
11X-1	84.80	2.05	86.85
12H-1	93.50	6.09	99.59
13X-1	103.00	5.99	108.99
14X-1	112.70	5.99	118.69
15X-1	122.30	5.99	128.29
16X-1	131.90	5.99	137.89
18X-1	151.20	5.99	157.19
19X-1	160.90	5.99	166.89
20X-1	170.50	5.99	176.49
21X-1	180.10	5.99	186.09
22X-1	189.80	5.99	195.79
172-1054B-			
1H-1	0.00	0.15	0.15
2H-1	2.70	1.45	4.15
3H-1	12.20	3.35	15.55
4H-1	21.70	2.70	24.40
5H-1	31.20	3.15	34.35
6H-1	40.70	4.40	45.10
7H-1	50.20	5.20	55.40
8H-1	56.90	5.30	62.20
9H-1	66.40	5.15	71.55
10H-1	75.90	5.85	81.75
11H-1	85.40	6.94	92.34
12H-1	94.90	7.64	102.54
172-1054C-			
1H-1	0.00	0.15	0.15
2H-1	8.20	1.40	9.60
3H-1	17.70	0.80	18.50
4H-1	27.20	2.35	29.55
5H-1	28.20	2.90	31.10
6H-1	37.70	2.70	40.40
7H-1	47.20	2.60	49.80
8H-1	56.70	3.60	60.30
9H-1	58.70	3.70	62.40
10H-1	68.20	3.30	71.50
11H-1	77.70	3.85	81.55
12H-1	87.20	6.29	93.49
13H-1	96.70	7.54	104.24
172-1055A-			
1H-1	0.00	1.35	1.35

Core, section	Depth (mbsf)	Offset (m)	Depth (mcd)
172-1055B-			
1H-1	0.00	0.15	0.15
2H-1	4.50	-0.05	4.45
3H-1	14.00	3.13	17.13
4H-1	23.50	4.43	27.93
5H-1	33.00	5.72	38.72
6H-1	42.50	6.42	48.92
7H-1	52.00	7.37	59.37
8H-1	61.50	7.81	69.31
9H-1	71.00	8.51	79.51
10H-1	80.50	10.46	90.96
11H-1	90.00	12.07	102.07
12H-1	99.50	14.49	113.99
13H-1	109.00	15.60	124.60
14H-1	118.50	17.73	136.23
172-1055C-			
1H-1	0.00	0.00	0.00
2H-1	8.50	0.80	9.30
3H-1	18.00	3.19	21.19
4H-1	27.50	3.82	31.32
5H-1	37.00	5.72	42.72
6H-1	46.50	6.47	52.97
7H-1	56.00	8.67	64.67
8H-1	65.50	9.36	74.86
9H-1	75.00	9.96	84.96
10H-1	82.50	10.46	92.96
11H-1	92.00	14.95	106.95
12H-1	101.50	17.36	118.86
13H-1	111.00	17.11	128.11
14H-CC	120.50	13.55	134.05
172-1055D-			
1H-1	0.00	0.11	0.11
2H-1	5.60	1.71	7.31
3H-1	15.10	3.10	18.20
4H-1	24.60	4.54	29.14
5H-1	34.10	5.87	39.97
6H-1	43.60	6.62	50.22
7H-1	53.10	7.67	60.77
8H-1	62.60	9.26	71.86
9H-1	72.10	10.26	82.36
10H-1	81.60	11.97	93.57
11H-1	91.10	14.37	105.47
12H-1	100.60	18.01	118.61
13H-1	110.10	18.38	128.48
14H-1	119.60	20.16	139.76
172-1055E-			
1H-1	0.00	-0.20	-0.20
2H-1	8.50	1.08	9.58

this site). The spliced records from this site utilize data primarily from Holes 1054B and 1054C above 118 mcd, and then use the only available data below 118 mcd from Hole 1054A.

Site 1055

The magnetic susceptibility, lightness L*, and the chromaticity parameters a* and b* appear well correlated between holes for the entire interval cored. As a result of core expansion, the composite depth scale (mcd) is ~10% larger than the drilled depths (mbsf) at Site 1055 (Fig. 25). GRAPE bulk density is less well correlated between holes deeper in the cored interval, apparently because of cracks in the sediment. Composite depth offsets were determined for all five holes at this site. Holes 1055A and 1055E were shallow holes that correlate well to the deeper holes at this site, but they are not shown on the composite figures. Hole 1055B appears to differ somewhat from Holes 1055C and 1055D in the interval from ~25 to 32 mcd, suggesting either problems with sediment recovery or lateral variation in sedimentary units. The spliced records from this site were created by combining portions of the composite records from Holes 1055C, 1055D, and 1055E.

Correlations Between Sites 1054 and 1055

Spliced records from all sites are plotted in Figure 26 (see backpocket foldout, this volume). The spliced records from Sites 1054 and 1055 are not easily correlated on the basis of susceptibility and color patterns alone because of the large difference in sedimentation rates between the two sites (see “Biostratigraphy” section, this chapter) and the apparently large number of hiatuses at failure planes represented by turbidites and other mass-flow deposits (see “Lithostratigraphy” and “Site Geophysics” sections, this chapter).

SEDIMENTATION AND MASS ACCUMULATION RATES

At Site 1054 sedimentation rates are calculated using only the biostratigraphic markers, as the magnetic susceptibility record is not clearly understood. The sedimentation rates in the past 0.5 m.y. have a mean value of 4.5 cm/k.y., but between ~0.5 and ~1.0 Ma a much lower rate (~1.3 cm/k.y.) is calculated (Fig. 27A). The lithostratigraphy (see “Lithostratigraphy” section, this chapter) through this interval (Core 172-1054A-3H and the upper part of 4H, ~20–35 mbsf) includes several scoured surfaces beneath fining-upward sequences, suggesting periodic removal and redeposition of sediment by bottom currents.

By contrast, at Site 1055 progressively higher rates of sediment accumulation are interpreted based on biostratigraphic data between 1.3 Ma (~130 mbsf) and the top of the section (Fig. 27B). But the sediment record at Site 1055 is not complete, and a hiatus may be present somewhere between 130 mcd (114.4 mbsf) and 90 mcd (81.5 mbsf

Table 19. Splice tie points for Sites 1054 and 1055.

Hole, core, section, interval (cm)	Depth (mbsf)	Depth (mcd)		Hole, core, section, interval (cm)	Depth (mbsf)	Depth (mcd)
1054A-1H-4, 54.0	5.04	5.04	Tie	1054B-2H-1, 89.0	3.59	5.04
1054B-2H-6, 89.0	11.09	12.54	Tie	1054C-2H-2, 144.0	11.14	12.54
1054C-2H-6, 39.0	16.09	17.49	Tie	1054B-3H-2, 44.0	14.14	17.49
1054B-3H-4, 104.0	17.74	21.09	Tie	1054A-3H-2, 84.0	19.84	21.09
1054A-3H-5, 124.0	24.74	25.99	Tie	1054B-4H-2, 9.0	23.29	25.99
1054B-4H-6, 9.0	29.29	31.99	Tie	1054C-5H-1, 89.0	29.09	31.99
1054C-5H-5, 104.0	35.24	38.14	Tie	1054B-5H-3, 79.0	34.99	38.14
1054B-5H-5, 129.0	38.49	41.64	Tie	1054C-6H-1, 124.0	38.94	41.64
1054C-6H-6, 19.0	45.39	48.09	Tie	1054B-6H-2, 149.0	43.69	48.09
1054B-6H-5, 129.0	47.99	52.39	Tie	1054C-7H-2, 109.0	49.79	52.39
1054C-7H-6, 109.0	55.79	58.39	Tie	1054B-7H-2, 149.0	53.19	58.39
1054B-7H-5, 34.0	56.54	61.74	Append	1054B-8H-1, 0.0	56.90	62.20
1054B-8H-7, 49.0	66.39	71.69	Tie	1054B-9H-1, 14.0	66.54	71.69
1054B-9H-7, 48.7	75.89	81.04	Tie	1054A-10H-3, 98.7	79.29	81.04
1054A-10H-6, 88.7	83.69	85.44	Tie	1054B-10H-3, 68.7	79.59	85.44
1054B-10H-5, 49.0	82.39	88.24	Tie	1054A-11X-1, 139.0	86.19	88.24
1054A-11X-7, 4.0	93.84	95.89	Tie	1054C-12H-2, 88.0	89.60	95.89
1054C-12H-5, 89.0	94.09	100.38	Tie	1054A-12H-1, 79.0	94.29	100.38
1054A-12H-5, 129.0	100.79	106.88	Tie	1054B-12H-3, 134.0	99.24	106.88
1054B-12H-6, 19.0	102.59	110.23	Tie	1054A-13X-1, 124.0	104.24	110.23
1054A-13X-6, 139.0	111.89	117.88	Append	1054A-14X-1, 0.0	112.70	118.69
1054A-14X-CC, 14.0	122.16	128.15	Append	1054A-15X-1, 0.0	122.30	128.29
1054A-15X-CC, 19.0	130.64	136.63	Append	1054A-16X-1, 0.0	131.90	137.89
1054A-16X-CC, 24.0	141.46	147.45	Append	1054A-18X-1, 0.0	151.20	157.19
1054A-18X-6, 144.0	159.41	165.40	Append	1054A-19X-1, 0.0	160.90	166.89
1054A-19X-4, 39.0	165.79	171.78	Append	1054A-20X-1, 0.0	170.50	176.49
1054A-20X-6, 19.0	177.53	183.52	Append	1054A-21X-1, 0.0	180.10	186.09
1054A-21X-7, 129.0	189.31	195.30	Append	1054A-22X-1, 0.0	189.90	195.79
1054A-22X-6, 103.7	198.34	204.33				
1055C-1H-4, 44.0	4.94	4.94	Tie	1055B-2H-1, 49.0	4.99	4.94
1055B-2H-5, 44.0	10.94	10.89	Tie	1055C-2H-2, 9.0	10.09	10.89
1055C-2H-6, 89.7	16.90	17.70	Tie	1055B-3H-1, 55.2	14.57	17.70
1055B-3H-2, 139.0	16.89	20.02	Tie	1055D-3H-2, 32.0	16.92	20.02
1055D-3H-5, 4.0	21.14	24.24	Tie	1055C-3H-3, 3.0	21.05	24.24
1055C-3H-7, 114.0	27.11	30.30	Tie	1055D-4H-1, 114.5	25.76	30.30
1055D-4H-6, 129.0	33.39	37.93	Tie	1055C-4H-5, 59.5	34.11	37.93
1055C-4H-7, 24.0	36.74	40.56	Tie	1055D-5H-1, 58.5	34.69	40.56
1055D-5H-5, 74.0	40.84	46.71	Tie	1055C-5H-3, 99.0	40.99	46.71
1055C-5H-6, 114.7	45.65	51.37	Tie	1055D-6H-1, 114.7	44.75	51.37
1055D-6H-7, 64.7	53.25	59.87	Tie	1055B-7H-1, 49.7	52.50	59.87
1055B-7H-6, 29.7	59.80	67.17	Tie	1055D-7H-5, 39.7	59.50	67.17
1055D-7H-6, 49.7	61.10	68.77	Tie	1055C-7H-3, 109.7	60.10	68.77
1055C-7H-7, 9.0	65.09	73.76	Tie	1055D-8H-2, 38.0	64.50	73.76
1055D-8H-6, 54.7	70.65	79.91	Tie	1055B-9H-1, 39.7	71.40	79.91
1055B-9H-7, 44.0	80.44	88.95	Tie	1055C-9H-3, 99.0	78.99	88.95
1055C-9H-5, 74.0	81.74	91.70	Tie	1055B-10H-1, 74.0	81.24	91.70
1055B-10H-5, 29.0	86.79	97.25	Tie	1055C-10H-4, 72.5	86.79	97.25
1055C-10H-6, 104.0	90.10	100.56	Tie	1055D-10H-5, 99.0	88.59	100.56
1055D-10H-7, 9.0	90.69	102.66	Tie	1055B-11H-1, 59.0	90.59	102.66
1055B-11H-8, 54.0	100.24	112.31	Tie	1055C-11H-5, 24.0	97.36	112.31
1055C-11H-8, 4.0	101.66	116.61	Tie	1055B-12H-3, 3.0	102.12	116.61
1055B-12H-8, 64.0	110.37	124.86	Tie	1055C-12H-4, 150.0	107.50	124.86
1055C-12H-5, 59.0	108.09	125.45	Tie	1055B-13H-2, 59.0	109.85	125.45
1055B-13H-9, 44.0	118.92	134.52	Tie	1055D-13H-5, 109.5	116.14	134.52
1055D-13H-8, 29.0	119.82	138.20	Tie	1055B-14H-2, 144.0	120.47	138.20
1055B-14H-4, 79.0	122.82	140.55	Tie	1055D-14H-1, 79.0	120.39	140.55
1055D-14H-7, 84.0	129.44	149.60				

between 1 Ma and MIS 12; see "Lithostratigraphy" section, this chapter).

Because of the hiatus, estimates of the sedimentation and accumulation rates using high-resolution magnetic susceptibility records (see "Explanatory Notes" chapter, this volume) are made only for the past 600 k.y., during which the sedimentation rate averages 19 cm/k.y. The highest sedimentation rates are during MISs 2 through 4 and MISs 9 and 10 (Fig. 28). The highest value (~23 cm/k.y.) is that of MIS 10, and the lowest (~14–16 cm/k.y.) are those of MIS 6 and the 465- to 600-ka period. No consistent pattern in the sedimentation rates between glacial and interglacial intervals is discernible from the data (Tables 20, 21; Fig. 28). Sedimentation rates for the entire cored interval increase by between 13% and 15% because of the conversion from the mbsf to the mcd depth scale (see "Stratigraphic Correlation" section, this chapter).

Calcium carbonate accumulation rates average around 8 g/cm^2/k.y., and range from 4.6 to 12.9 g/cm^2/k.y. (Tables 22, 23; Fig. 29) at Site 1055. Carbonate fluxes at this site are generally higher during interglacial than during glacial intervals, except in MISs 2 and 4, where they reach approximately 10 and 12 g/cm^2/k.y., respectively. These deviations from the general pattern may be caused by shifts of data points during composite-depth scale conversion. The highest calcium carbonate accumulation rate value (>12 g/cm^2/k.y.) is calculated for MIS 7. The lowest ones (1–2 g/cm^2/k.y.) are calculated for MISs 2, 6, 10, and at ~580 ka. Calcium carbonate accumulation rates, in general, do not show any correlation with the sedimentation rates, indicating that sediment accumulation is largely controlled by the detrital influx rather than by oceanic productivity.

Organic carbon fluxes were calculated as well, but because of poor time resolution (only nine data points for the past 600 k.y.) no trend is recognizable. Carbon fluxes display an average value of 0.12 g/cm^2/k.y., and reach a maximum of around 0.18 g/cm^2/k.y. during MIS 3 (Tables 22, 23; Fig. 29).

ORGANIC GEOCHEMISTRY

Routine monitoring of headspace and vacutainer gases was done for drilling safety in at least every core using the standard ODP headspace sampling techniques (see "Explanatory Notes" chapter, this volume). Calcium carbonate and organic carbon concentrations were also measured on samples obtained from Holes 1054A and 1055B.

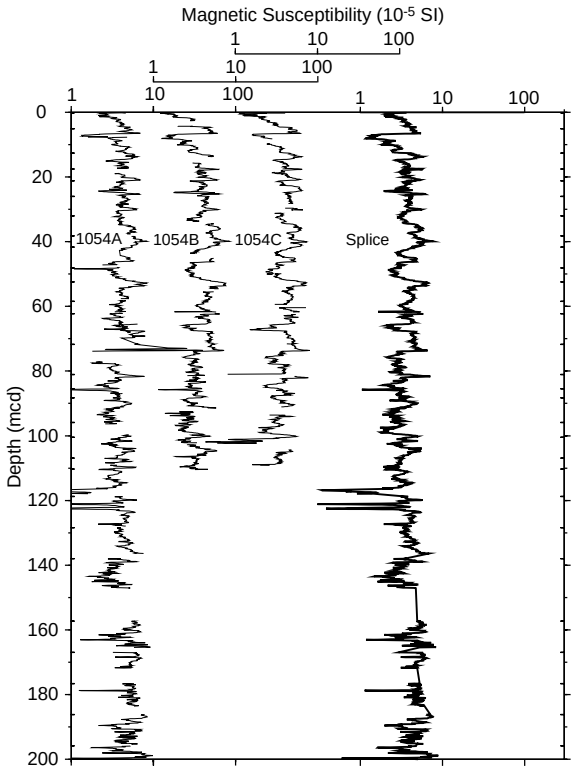

Figure 12. Smoothed magnetic susceptibility data (31-cm Gaussian window; logarithmic scale) from Site 1054 on the mcd scale for Holes 1054A through 1054C and the spliced record. Note: Only the upper 200 mcd is plotted (to ~194 mbsf), although the spliced record extends to ~204 mcd (~198 mbsf).

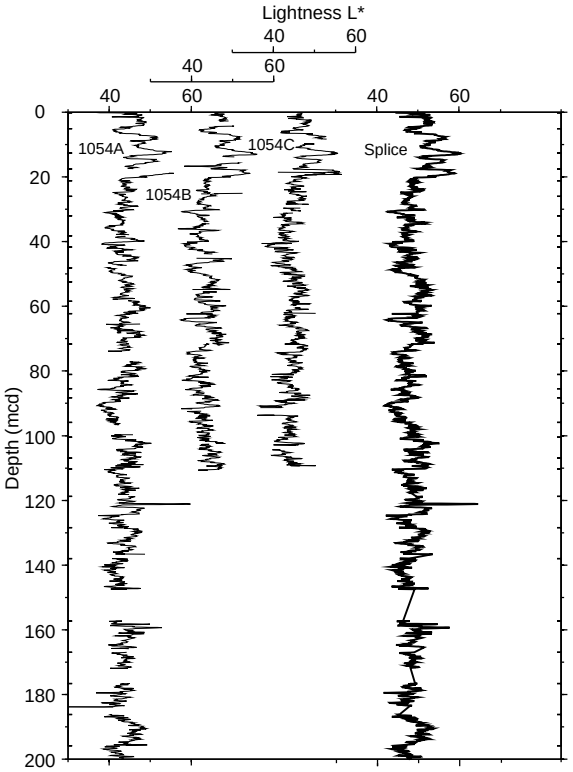

Figure 14. Smoothed lightness (L*) data (31-cm Gaussian window) from Site 1054 on the mcd scale for Holes 1054A through 1054C and the spliced record. Note: Only the upper 200 mcd is plotted (to ~194 mbsf), although the spliced record extends to ~204 mcd (~198 mbsf).

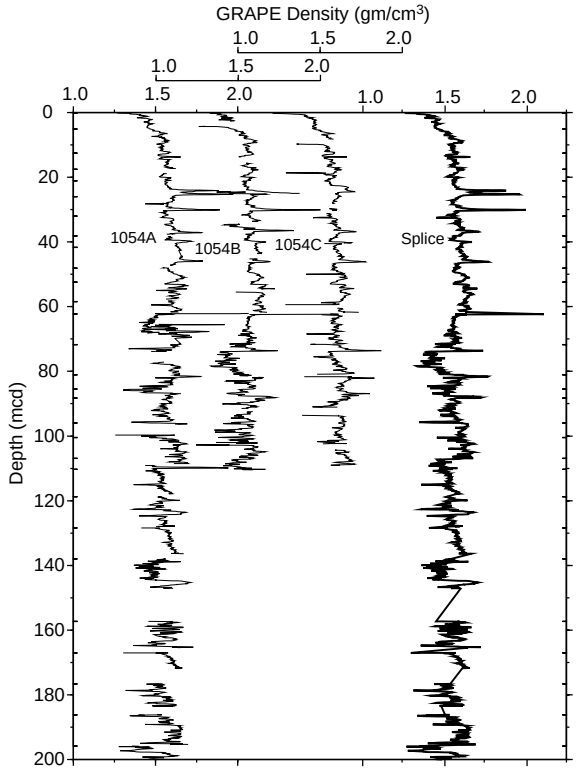

Figure 13. Smoothed GRAPE data (31-cm Gaussian window) from Site 1054 on the mcd scale for Holes 1054A through 1054C and the spliced record. Note: Only the upper 200 mcd is plotted (to ~194 mbsf), although the spliced record extends to ~204 mcd (~198 mbsf).

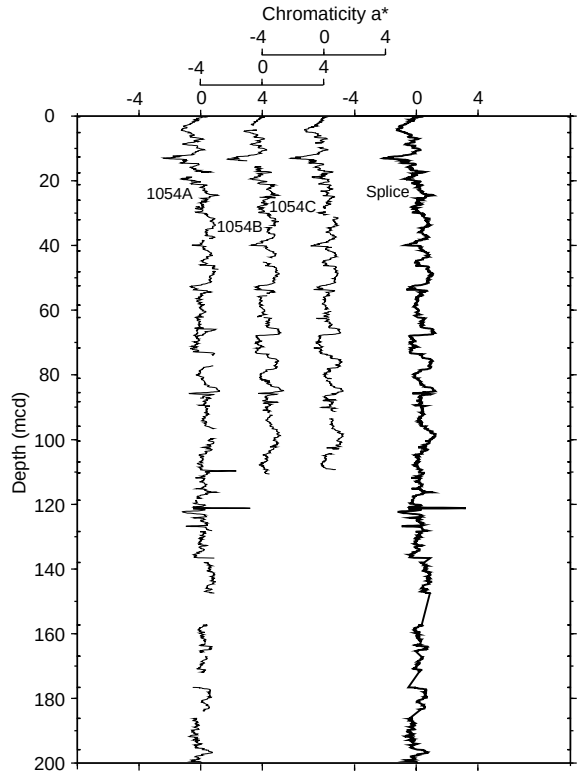

Figure 15. Smoothed chromaticity (a*) data (31-cm Gaussian window) from Site 1054 on the mcd scale for Holes 1054A through 1054C and the spliced record. Note: Only the upper 200 mcd is plotted (to ~194 mbsf), although the spliced record extends to ~204 mcd (~198 mbsf).

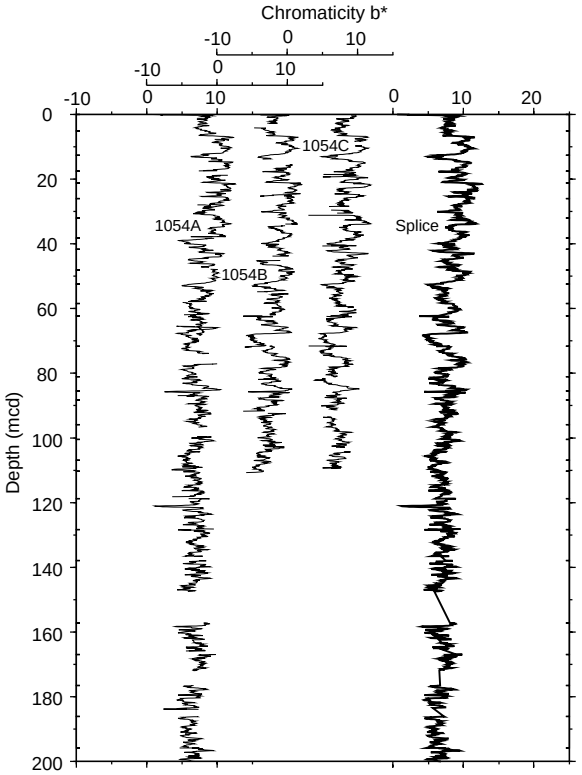

Figure 16. Smoothed chromaticity (b*) data (31-cm Gaussian window) from Site 1054 on the mcd scale for Holes 1054A through 1054C and the spliced record. Note: Only the upper 200 mcd is plotted (to ~194 mbsf), although the spliced record extends to ~204 mcd (~198 mbsf).

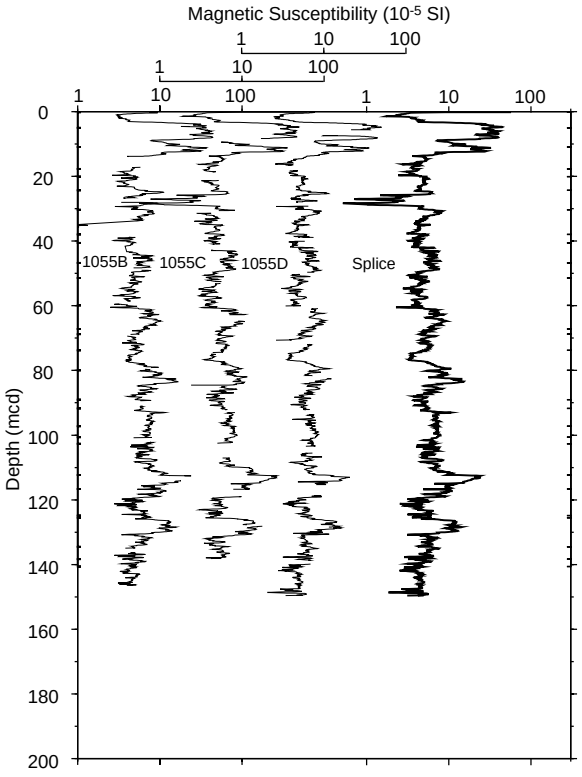

Figure 17. Smoothed magnetic susceptibility data (31-cm Gaussian window, logarithmic scale) from Site 1055 on the mcd scale for Holes 1055B through 1055D and the spliced record.

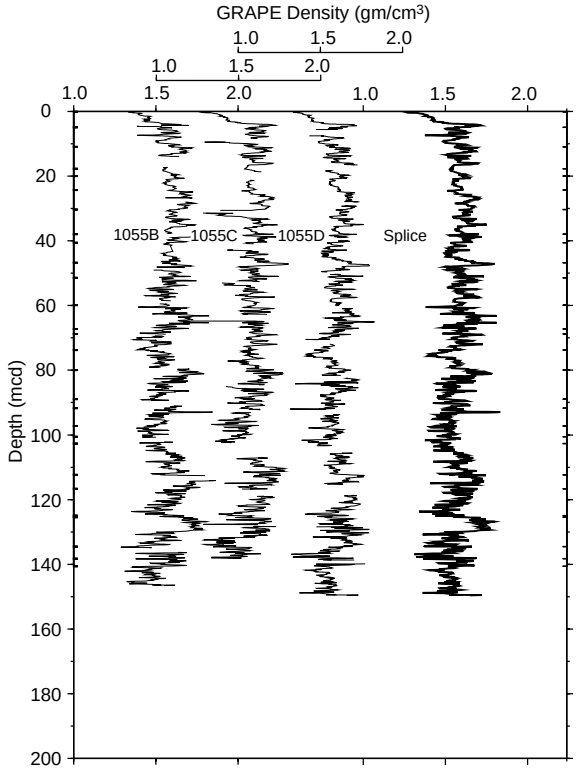

Figure 18. Smoothed GRAPE data (31-cm Gaussian window) from Site 1055 on the mcd scale for Holes 1055B through 1055D and the spliced record.

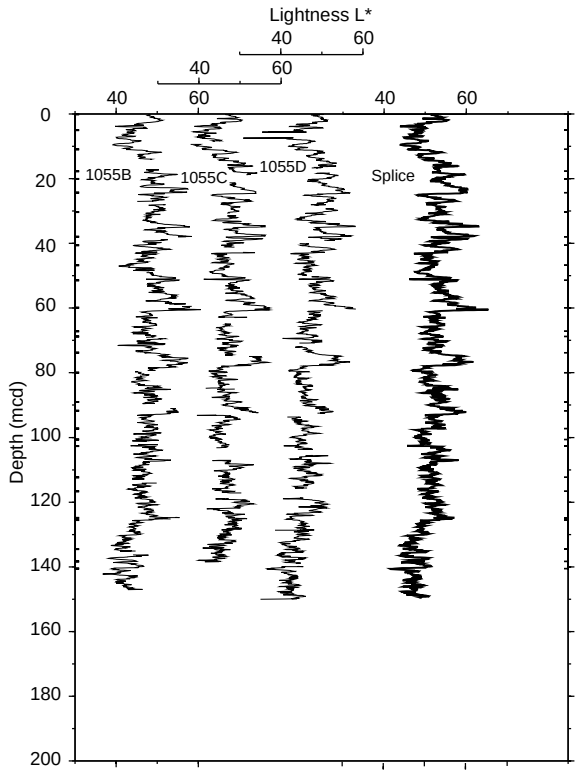

Figure 19. Smoothed lightness (L*) data (31-cm Gaussian window) from Site 1055 on the mcd scale for Holes 1055B through 1055D and the spliced record.

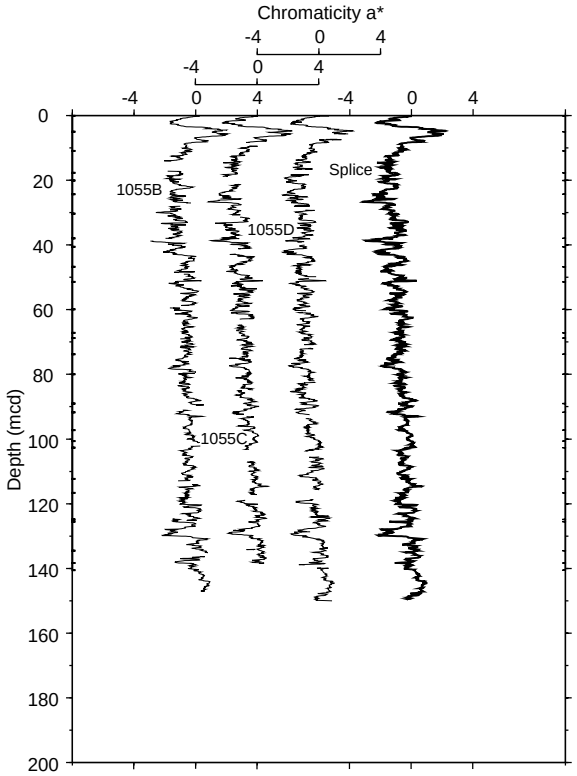

Figure 20. Smoothed chromaticity (a*) data (31-cm Gaussian window) from Site 1055 on the mcd scale for Holes 1055B through 1055D and the spliced record.

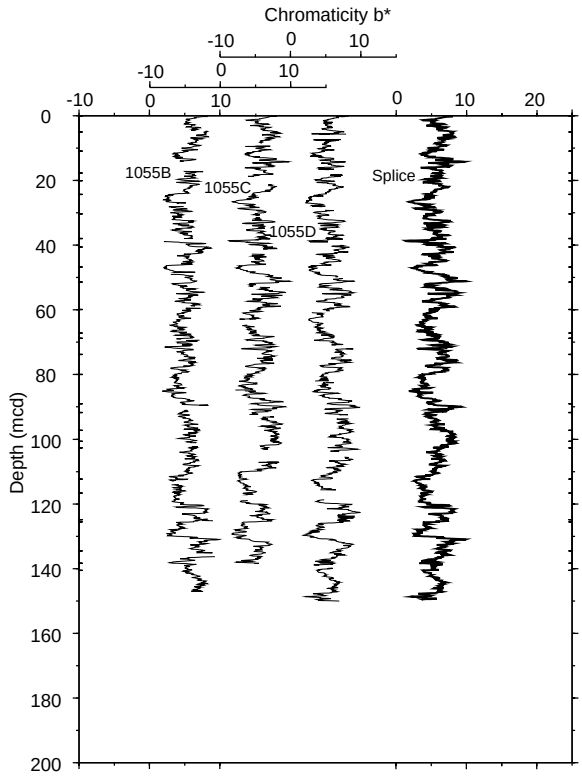

Figure 21. Smoothed chromaticity (b*) data (31-cm Gaussian window) from Site 1055 on the mcd scale for Holes 1055B through 1055D and the spliced record.

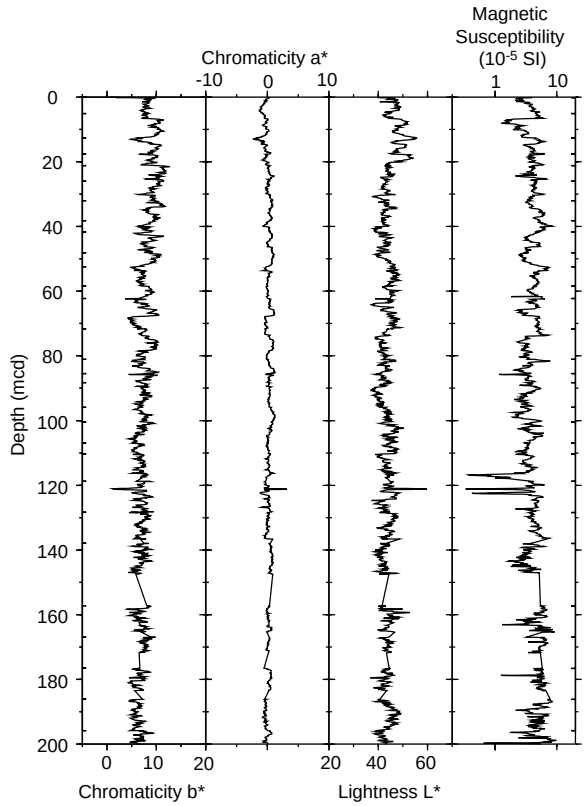

Figure 22. Summary of spliced records for Site 1054. Straight line segments show gaps in the record. Note: only the upper 200 mcd is plotted (to ~194 mbsf), although the spliced record extends to ~204 mcd (~198 mbsf).

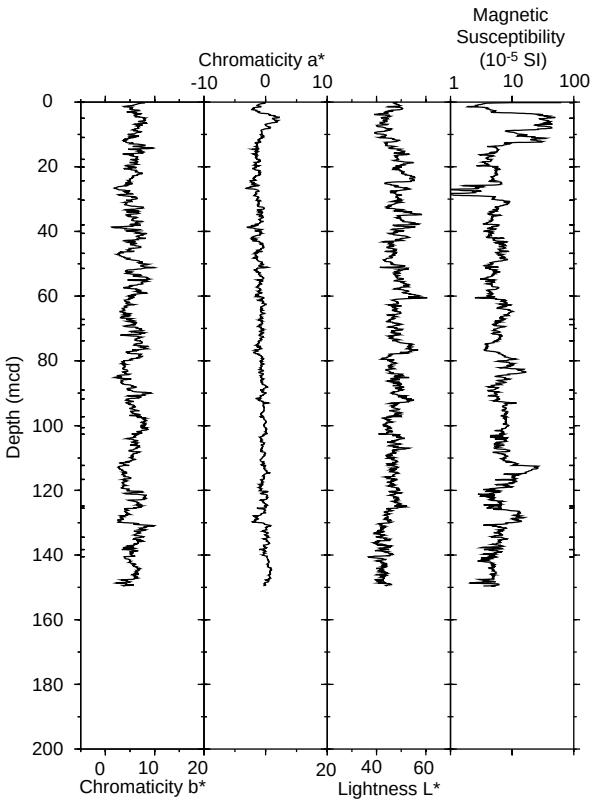

Figure 23. Summary of spliced records for Site 1055.

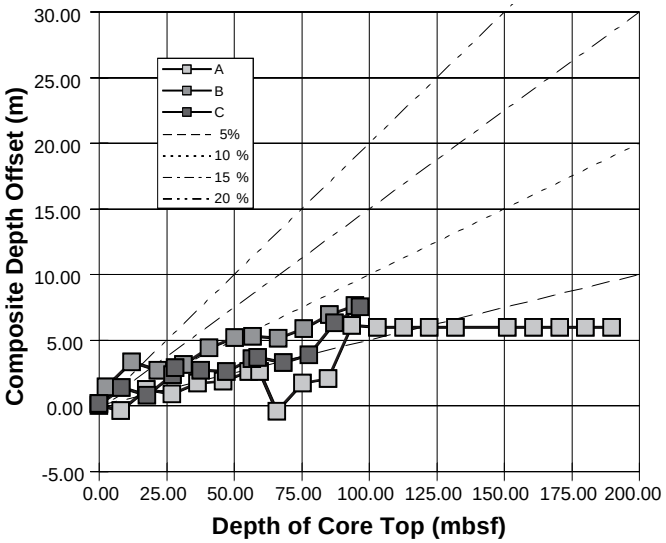

Figure 24. Composite depth offsets vs. core-top depth (mbsf) for Site 1054.

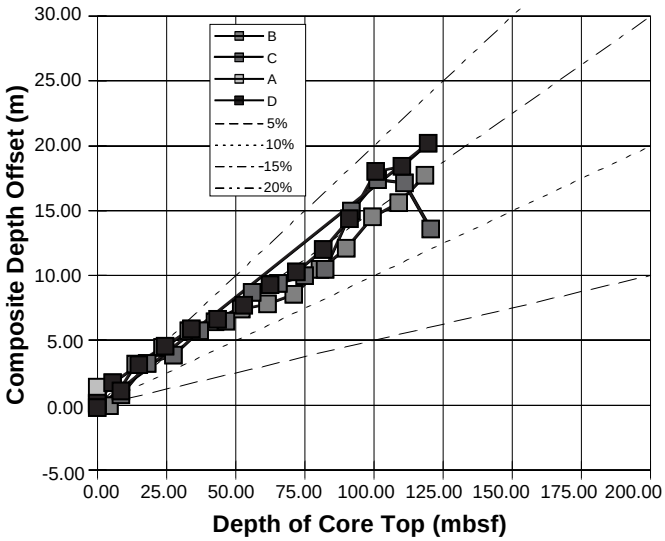

Figure 25. Composite depth offsets vs. core-top depth (mbsf) for Site 1055.

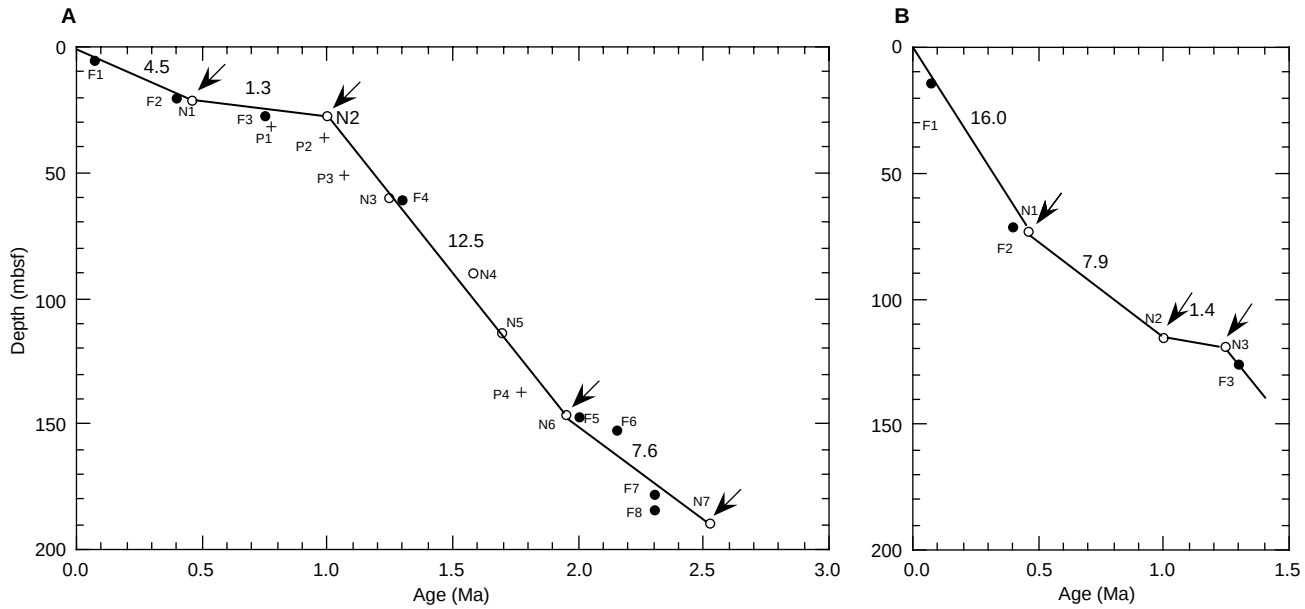

Figure 27. Age/depth plots for Holes (**A**) 1054A and (**B**) 1055B based on biostratigraphic tie points (arrows). Solid circles = planktonic foraminifer markers, open circles = nannoplankton markers, and crosses = magnetostratigraphic markers. See Table 4 to associate species names with the labels used in this figure. Sedimentation rates are expressed in centimeters per thousand years.

Organic matter C/N values and Rock-Eval pyrolysis analyses were employed to determine the type of organic matter contained in the sediments.

Volatile Hydrocarbons

Hole 1054A

Methane concentrations measured in headspace gas are heavily influenced by coring techniques, time exposure of the core to atmospheric pressure, the stage of sediment diagenesis, and analytical procedures (desorption conditions). Methane concentrations are low in the upper sections of Hole 1054A, but increase rapidly from 44 to 109 mbsf, reaching 33,779 ppm at 82.8 mbsf (Table 24; Fig. 30). Below this depth, methane generally decreases. Other hydrocarbons are present in extremely low amounts. Ethane does not reach higher concentrations than ~9 ppm; higher molecular-weight hydrocarbons are typically at concentrations of less than 1 ppm.

Headspace and vacutainer C_1/C_2 values show comparable downhole patterns. Higher values are recorded at intermediate depths, between 50 and 90 mbsf (Tables 24, 25; Fig. 31), decreasing downhole, but remaining at levels higher than 1000. Anomalously low headspace C_1/C_2 values (<100) occur in the uppermost section, probably caused by preferential loss of methane due to microbial oxidation rather than from a major contribution of thermal gas.

Hole 1055B

Hole 1055B generally shows a depth trend of light hydrocarbon concentration similar to Hole 1054A. Methane concentrations are low in the upper three cores (Table 24; Fig. 32) and then increase rap-

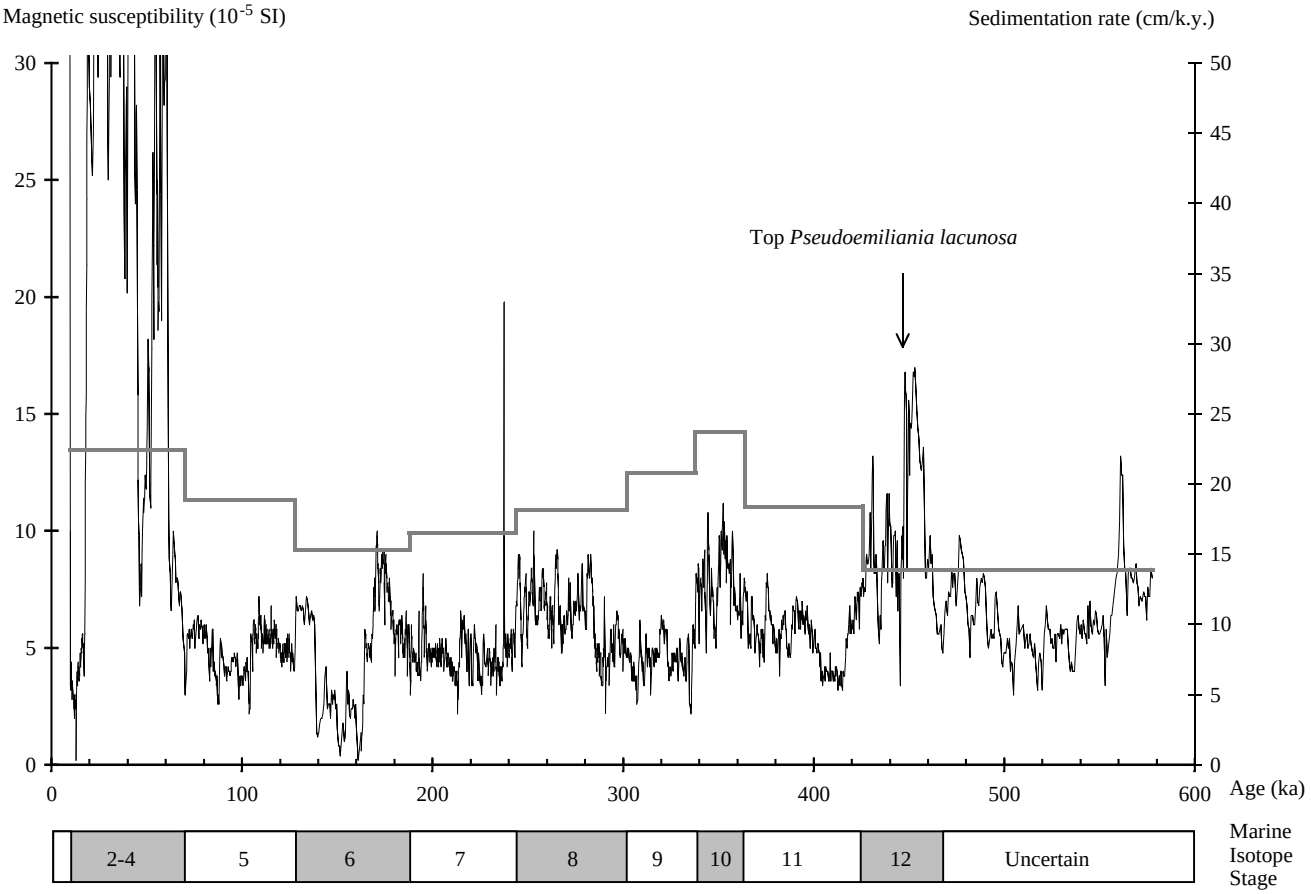

Figure 28. Magnetic susceptibility record (left scale, thin curve, composite record) and sedimentation rate (right scale, thick stepwise line) of Site 1055 (composite). The MISs are indicated, with the glacial ones shaded, in the bar along the bottom of the figure. The top of the *Pseudoemiliania lacunosa* range (460 ka) is indicated by the arrow (32°47′N, 76°17′W; 1799 m).

Table 20. Depth-to-depth correlation (mcd) between Sites 1055 and 1056.

Site 1055 depth (mcd)	Site 1056 depth (mcd)	Age (ka)
0.14	0.09	9.70
3.89	1.64	19.04
4.79	3.09	27.77
5.19	3.44	29.88
6.04	3.99	33.19
6.49	4.44	35.90
6.74	4.64	37.11
7.09	4.89	38.61
8.04	5.54	42.53
8.34	5.79	44.04
8.84	6.14	46.14
11.79	7.93	56.69
16.09	11.05	86.40
24.73	14.64	128.48
26.18	16.24	143.97
27.48	17.39	155.10
28.31	17.99	160.90
30.74	18.99	170.58
34.58	21.04	192.31
37.62	22.24	212.98
41.77	23.54	235.38
43.23	24.19	245.22
48.86	28.94	283.75
51.31	29.84	291.05
60.56	34.19	335.75
61.16	34.49	338.45
65.91	38.59	356.99
76.85	43.59	415.54
79.45	44.84	430.78
83.55	47.39	452.96

Note: Correlations based on depth-to-depth relation between magnetic susceptibility records, using Site 1056 as a reference.

Table 21. Age-depth relation for Site 1055 using the tie points defined in the "Explanatory Notes" section (this volume).

Age (ka)	Depth (mcd)	Average sedimentation rate (cm/k.y.)
10	0.26	22.4
70	13.72	22.4
128	24.63	18.8
188	33.82	15.3
244	43.05	16.5
302	53.58	18.1
338	61.06	20.8
364	67.22	23.7
426	78.63	18.4
476	85.57	13.9

idly from 26.5 to 88 mbsf, reaching 64,536 ppm at 50 mbsf. Below this depth, methane concentrations abruptly decrease, but stay at levels higher than 4000 ppm. Extremely low amounts of ethane are present, ranging from 0.4 to 2 ppm; higher molecular-weight hydrocarbons occur in concentrations of less than 1 ppm.

Headspace and vacutainer C_1/C_2 values are also similar to those from Hole 1054A. Higher headspace values occur at 50 mbsf (Tables 24, 25; Fig. 33), and sharply decrease with depth. Both headspace and vacutainer C_1/C_2 values higher than 4000 occur throughout the hole, a characteristic gas signature of immature sediments.

Discussion

Methane can be derived from either thermogenic or biogenic sources. In situ formation of methane by methanogenic bacteria is the

most likely source for methane at Holes 1054A and 1055B. High C_1/C_2 values, as well as the absence of a major contribution of higher molecular-weight hydrocarbons, indicate that the methane is biogenic as opposed to thermogenic in origin. Methane is probably formed by microbial CO_2 reduction and organic matter fermentation. Similar production of methane has been inferred from high biogenic gas concentrations in Pliocene–Pleistocene sediments from the Walvis Ridge (Meyers and Brassell, 1985), in middle Miocene sediments from Site 767 (Shipboard Scientific Party, 1990), in Pliocene–Pleistocene sediments of Site 976 in the Alboran Sea (Shipboard Scientific Party, 1996), and in sediments from Sites 991, 992, and 993 of the North American continental margin (Shipboard Scientific Party, 1996). At both sites, a biogenic origin of the methane is substantiated by the depletion of interstitial sulfate at exactly the same depth where methane concentrations begin to rise (see "Inorganic Geochemistry" section, this chapter). As noted by Claypool and Kvenvolden (1983), the presence of interstitial sulfate inhibits methanogenesis in sediments.

Hole 1055B generally shows higher methane concentrations throughout the sedimentary section. Here, the sulfate reduction zone is thinner and shallower than at Hole 1054A (see "Inorganic Geochemistry" section, this chapter).

Inorganic and Organic Carbon Concentrations

Hole 1054A

Carbonate carbon shows considerable variation, ranging from 4.04 to 8.05 wt% (Table 26; Fig. 34). These values are equivalent to 33.7 to 67 wt% sedimentary $CaCO_3$, assuming that all of the carbonate is pure calcite. The range in carbonate content reflects interplay between biological productivity, dilution by noncarbonate sedimentary components, and postdepositional carbonate dissolution. Highest $CaCO_3$ values occur between 6.44 and 21.27 mbsf, 43.28 and 72.42 mbsf, and 94.33 and 119.48 mbsf. The lowest values occur below 180 mbsf.

Sediments from Hole 1054A average 1.2 wt% TOC, about four times higher than the average of 0.3 wt% compiled by McIver (1975) from DSDP Legs 1 through 33. TOC concentrations range from 0.7 (31 mbsf) to 1.84 wt% (88.6 mbsf; Table 26; Fig. 34).

Hole 1055B

Carbonate carbon shows a wide range of variation, ranging from 1.72 to 7.57 wt% (Table 26; Fig. 35). These values are equivalent to 14.33–63.09 wt% sedimentary $CaCO_3$, assuming that all of the carbonate is pure calcite. High $CaCO_3$ accumulations are found in the top of the hole, especially between 0.63 and 2.03 mbsf. Downhole, carbonate content shows large fluctuations with especially high values between 5.28 and 58.42 mbsf, which could correspond to a high accumulation period recorded at Hole 1054A between 6.44 and 21.27 mbsf. This event has been estimated to last from 0.068 to 0.41 Ma in both sites (see "Biostratigraphy" section, this chapter). Typically lower values are found below 100 mbsf.

Sediments from Hole 1055B also contain relatively high TOC concentrations that range from 0.3 (62 mbsf) to an astonishingly high 2.10 wt% (127.14 mbsf) (Table 26; Fig. 35). Highest TOC values occur below 116 mbsf. That level has been estimated to be older than 1.30 Ma (see "Biostratigraphy" section, this chapter), and thus could correspond to the high TOC value recorded in Hole 1054A. High TOC concentrations are likely caused by a decrease in sedimentation rate, lowering the TOC dilution by mineral material and/or by an increase in primary production.

Organic Matter Source Characterization

Hole 1054A

Organic C/N values help to identify the provenance of organic matter. C/N ratios from Site 1054A vary from <5 to 10 (Table 26). Low C/N values occur in samples with especially low TOC, and are probably an artifact due to low total carbon (TC) content and the tendency of clay minerals to absorb ammonium ions (Müller, 1977). Average C/N values of marine zooplankton and phytoplankton lie between 5 and 8, whereas land plants have ratios between 20 and 200 (Emerson and Hedges, 1988). The C/N values of samples containing more than 1 wt% TOC average 9. Although these values may change during maturation, these C/N values should reflect a major contribution of unaltered algal material (Meyers, 1994).

Sediment samples having elevated TOC concentrations (>1 wt%) were selected for Rock-Eval analysis to characterize the type and thermal maturity of the organic matter (Table 27). A van Krevelen plot of the Hydrogen Index (HI) and Oxygen Index (OI) values suggests that the sedimentary organic matter is a mixture of partially oxidized type II algal material and type III land-plant material (Fig. 36). However, this source assignment for the organic matter conflicts with the relatively low C/N values for these samples, which indicate that the organic matter is predominantly marine material. The contradiction between the Rock-Eval and elemental source characterizations is evidence that the marine organic matter has been oxidized, probably by microbial reworking (Espitalié et al., 1986). The dominance of refractory organic material here is consistent with results from the SEEP experiment conducted farther north on the continental slope between Cape Hatteras and Martha's Vineyard (Biscaye and Ander-

Table 22. Estimated ages, concentrations, and accumulation rates of calcium carbonate at Site 1055.

Age (ka)	$CaCO_3$ content (wt%)	$CaCO_3$ MAR ($g/cm^2/k.y.$)
11.29	54.31	6.09
14.78	47.37	11.75
18.54	27.41	4.60
30.04	32.04	5.40
43.79	32.63	6.22
54.94	37.53	9.80
95.22	54.82	7.92
110.46	51.31	8.00
124.73	55.12	9.11
162.93	45.49	7.94
178.56	29.68	7.32
192.44	62.13	12.93
224.10	45.63	7.04
239.16	47.21	6.52
263.63	41.08	6.81
287.98	44.25	7.03
297.67	42.92	6.81
312.22	48.21	9.78
334.16	53.17	9.79
345.24	34.79	9.47
356.52	30.68	8.80
378.08	43.75	8.11
394.67	43.04	7.08
410.73	63.09	11.13
546.47	52.70	7.77
578.60	34.97	4.63

Notes: MAR = mass accumulation rate. Estimations based on geochemistry data collected at Hole 1055B

Table 23. Estimated ages, concentrations, and accumulation rates of organic carbon at Site 1055.

Age (ka)	C_{org} content (wt%)	C_{org} MAR ($g/cm^2/k.y.$)
18.54	0.92	0.15
30.04	1.08	0.18
43.79	0.68	0.13
54.94	0.31	0.08
192.44	0.65	0.14
263.63	0.66	0.11
345.24	0.36	0.10
378.08	0.30	0.06
578.60	1.16	0.15

Notes: MAR = mass accumulation rate. Estimations based on geochemistry data collected at Hole 1055B.

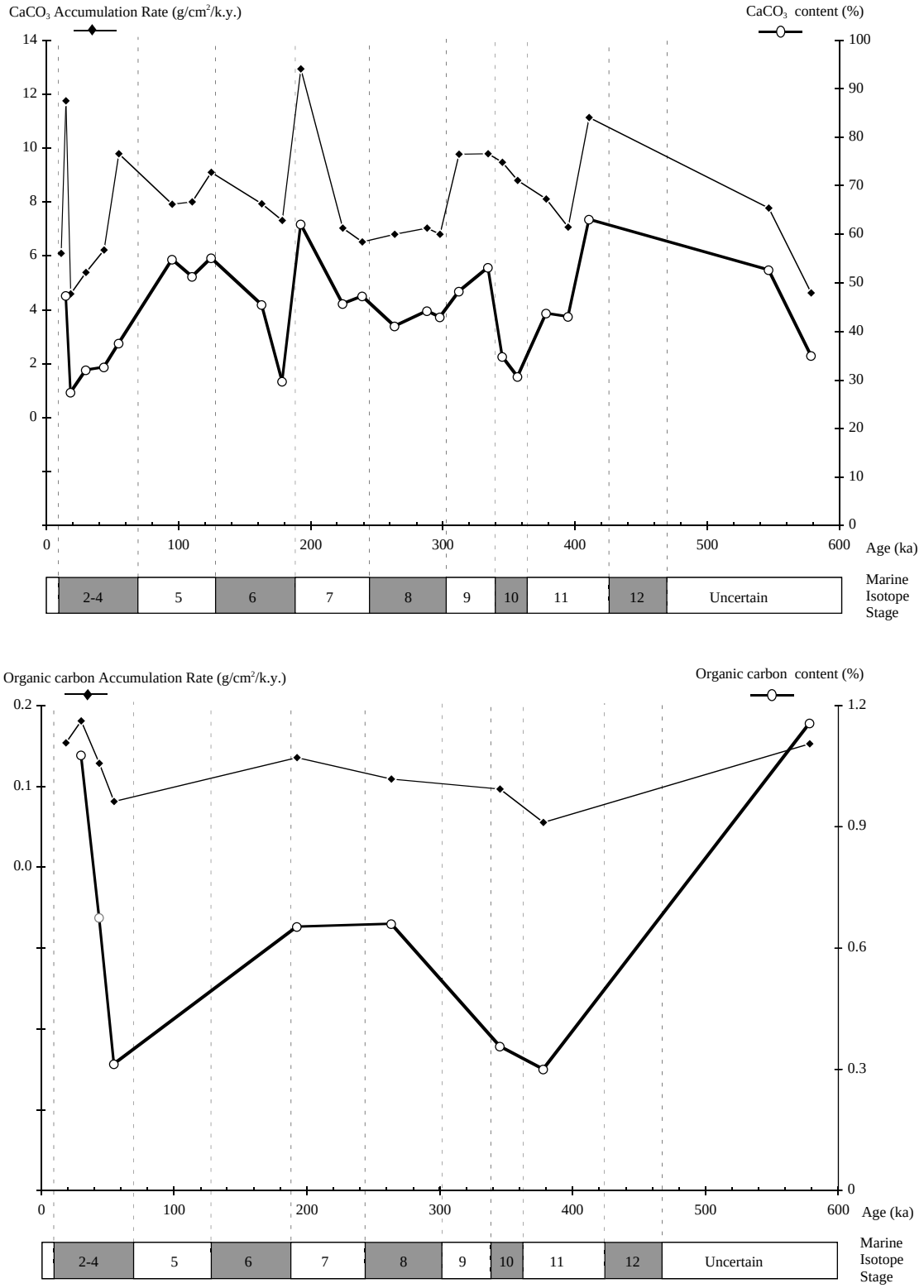

Figure 29. Downhole profiles of calcium carbonate and organic carbon accumulation rates at Site 1055 (composite). MISs are indicated, with glacial ones shaded. Dashed lines = magnetic susceptibility-based boundaries.

Table 24. Results of headspace gas analyses of sediments from Sites 1054 and 1055.

Core, section, interval (cm)	Depth (mbsf)	C_1 (ppm)	C_2 (ppm)	C_3 (ppm)	C_1/C_2
172-1054A-					
1H-2, 0-5	1.5	13	ND	ND	—
1H-5, 0-5	6.0	7	ND	ND	—
2H-1, 0-5	8.0	14	ND	ND	—
2H-2, 0-5	9.5	14	ND	ND	—
2H-3, 0-5	11.0	21	ND	ND	—
2H-4, 0-5	12.5	23	0.22	ND	105
2H-5, 0-5	14.0	29	ND	ND	—
3H-2, 0-5	19.0	48	0.73	ND	66
3H-3, 0-5	20.5	83	2	ND	42
3H4, 0-5	22.0	86	2	ND	43
3H5, 0-5	23.5	92	2	ND	46
3H-6, 0-5	25.0	124	2	ND	62
4H-2, 0-5	28.5	256	4	ND	64
4H-3, 0-5	30.0	278	5	ND	56
4H-4, 0-5	31.5	291	5	ND	58
4H-5, 0-5	33.0	238	4	ND	60
4H-6, 0-5	34.5	223	4	ND	56
5H-2, 0-5	38.0	120	5	ND	24
5H-4, 0-5	41.0	376	5	ND	75
5H-6, 0-5	44.0	492	5	ND	98
6H-6, 0-5	53.5	18,359	8	3	2,295
7H-2, 0-5	57.0	27,557	9	2	3,062
8H-3, 0-5	62.4	19,497	5	ND	3,899
10H-6, 0-5	82.8	33,779	8	2	4,222
11X-5, 0-5	90.8	26,883	ND	ND	—
13X-5, 0-5	109.0	2,823	1	ND	2,823
14X5, 0-5	118.7	4,866	2	ND	2,433
15X-5, 0-5	128.3	912	1	2	912
16X-5, 0-5	137.9	5,129	3	2	1,710
18X-3, 0-5	154.2	4,763	2	ND	2,382
19X-3, 0-5	163.9	5,291	3.5	ND	1,512
20X-3, 0-5	173.5	5,408	4.3	5	1,258
21X-3, 0-5	182.2	2,225	1.4	ND	1,589
22X-5, 0-5	195.8	1,229	1	ND	1,229
172-1055B-					
1H-2, 0-5	1.5	2	ND	ND	—
1H-3, 0-5	3.0	3	ND	ND	—
2H-2, 0-5	6.0	3	ND	ND	—
2H-3, 0-5	7.5	3	ND	ND	—
2H-4, 0-5	9.0	192	ND	ND	—
2H-5, 0-5	10.5	14	ND	ND	—
2H-6, 0-5	12.0	3	ND	ND	—
3H-2, 0-5	15.5	25	ND	ND	—
3H-3, 0-5	17.0	30	ND	ND	—
3H4, 0-5	18.5	72	ND	ND	—
3H5, 0-5	20.0	55	ND	ND	—
3H-6, 0-5	21.5	193	ND	ND	—
4H-2, 0-5	25.0	2,027	ND	ND	—
4H-3, 0-5	26.5	1,767	ND	ND	—
4H-4, 0-5	28.0	9,590	1	ND	9,590
4H-5, 0-5	29.5	6,783	0.4	ND	16,958
4H-6, 0-5	31.0	8,313	0.4	ND	20,783
5H-2, 0-5	34.5	22,403	1	ND	22,403
5H-3, 0-5	36.0	21,503	1.22	ND	17,625
5H-4, 0-5	37.5	27,495	1.47	ND	18,704
5H-5, 0-5	39.0	35,714	2.22	ND	16,087
5H-6, 0-5	40.5	37,188	1.81	ND	20,546
6H-6, 0-5	50.0	64,536	2	ND	32,268
7H-6, 140-145	60.9	29,688	1	ND	29,688
8H-2, 0-5	63.0	22,810	1	1	22,810
8H-6, 135-140	70.4	27,579	1.48	ND	18,634
9H-2, 0-5	72.5	24,417	1.63	ND	14,980
9H-5, 0-5	77.0	16,190	1.61	ND	10,056
10H-2, 0-5	82.0	12,517	1	ND	12,517
10H-6, 0-5	88.0	4,292	0.46	0	9,330
11H-3, 0-5	92.2	13,655	1.17	ND	11,671
11H-8, 0-5	99.7	13,895	1.48	1	9,389
12H-4, 0-5	103.6	11,377	1.2	ND	9,481
12H-7, 0-5	108.1	4,698	1	ND	4,698
13H-4, 0-5	112.3	11,095	2.03	2	5,466
13H7, 0-5	116.8	8,830	1	ND	8,830
14H-7, 0-5	126.5	7,769	1.86	ND	4,177

Notes: ND = not detected; — = not applicable.

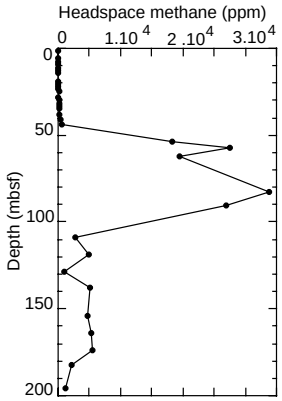

Figure 30. Downhole profile of headspace methane concentrations in Hole 1054A.

Table 25. Results of vacutainer gas analyses of sediments from Holes 1054A and 1055A.

Core, section, interval (cm)	Depth (mbsf)	C_1 (ppm)	C_2 (ppm)	C_3 (ppm)	C_1/C_2
172-1054A-					
6H-5, 50-51	52.5	27,229	6	4	4,538
10H-2, 135-136	84.2	625,170	155	29	4,033
11X-2, 135-136	87.7	622,670	146	30	4,265
11X-3, 135-136	89.2	463,930	135	21	3,437
13X-5, 135-136	110.4	564,942	155	39	3,645
14X-5, 51-52	119.2	798,910	250	63	3,196
16X-6, 135-136	140.8	806,727	218	48	3,701
18X-2, 135-136	154.1	715,195	185	38	3,866
19X-2, 135-136	163.8	671,931	245	85	2,743
20X-2, 135-136	173.4	407,057	150	38	2,714
21X-2, 135-136	186.4	625,170	155	29	4,033
22X-5, 135-136	197.2	642,292	176	62	3,649
172-1055A-					
8H-2, 135-136	64.4	284,408	36	5	7,900
9H-2, 135-136	73.9	682,130	107	8	6,405
11X-3, 135-136	93.6	798,184	147	11	5,430
11H-3, 135-136	103.3	1,209,871	215	19	5,627
13H-5, 135-136	113.6	823,438	146	13	5,640

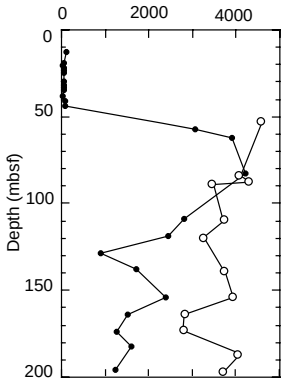

Figure 31. Downhole profiles of headspace and vacutainer methane/ethane ratios in Hole 1054A. Solid circles = headspace samples; open circles = vacutainer samples.

son, 1994). Rock-Eval T_{max} values are relatively low at all depths (Table 27). They indicate that organic matter is thermally immature with respect to petroleum generation.

Hole 1055B

C/N values vary from <2 to 35 (Table 26). The anomalously high value at 55.5 mbsf may be an artifact because total nitrogen concentration (TN) is 0.1 wt%, which is close to the detection limit of the CNS device. As at Hole 1054A, low C/N values generally occur in samples with especially low TOC. C/N values of samples containing more than 1 wt% TOC average 6, characteristic of marine zooplankton and phytoplankton (Emerson and Hedges, 1988).

The results of Rock-Eval analyses of selected samples from Hole 1055B suggest that sediments contain a mixture of type II (algal material) and type III (land-derived) organic matter (Table 27; Fig. 37).

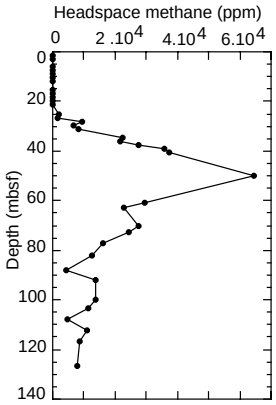

Figure 32. Downhole profile of headspace methane concentrations for Hole 1055B.

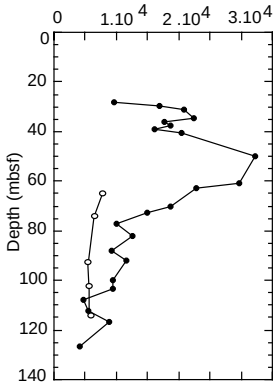

Figure 33. Downhole profiles of headspace and vacutainer methane/ethane ratios for Hole 1055B. Solid circles = headspace samples; open circles = vacutainer samples.

Table 26. Results of coulometric and elemental analyses from Sites 1054 and 1055.

Core, section, interval (cm)	Depth (mbsf)	IC (wt%)	$CaCO_3$ (wt%)	TC (wt%)	TOC (wt%)	TN (wt%)	TS (wt%)	C/N
172-1054A-								
1H-1, 90-91	0.9	6.96	57.97					
1H-3,87-88	3.9	6.09	50.73					
1H-5, 44-45	6.4	5.49	45.77	6.35	0.86	0.12	0.68	6.91
2H-1, 56-57	8.6	8.05	67.03					
2H-3, 76-77	11.8	7.24	60.31					
2H-5, 101-102	15.0	7.75	64.52					
3H-1, 34-35	17.8	7.03	58.55					
3H-3, 77-78	21.3	5.86	48.81	6.98	1.12	0.12	0.81	9.00
3H-5, 77-78	24.3	5.96	49.66					
4H-1, 95-96	28.0	5.43	45.23					
4H-3, 71-72	30.7	5.40	44.95	6.12	0.73	0.11	1.01	6.44
4H-5, 96-97	34.0	5.74	47.84					
5H-1, 78-79	37.3	4.07	33.89	5.17	1.11	0.12	1.34	8.91
5H-3, 78-79	40.3	4.63	38.57	5.84	1.21	0.13	1.40	9.33
5H-5, 78-79	43.3	4.78	39.85	6.11	1.32	0.16	1.29	8.14
6H-1, 28-29	46.3	5.79	48.21					
6H-3, 79-80	49.8	6.07	50.54					
6H-5, 141-142	53.4	6.28	52.34					
7H-1, 111-112	56.6	5.62	46.81	7.12	1.50	0.15	1.28	9.90
7H-3, 42-43	58.9	6.02	50.18					
8H-1, 132-133	60.7	5.42	45.17	6.75	1.33	0.13	1.34	10.06
9H-1, 62-63	66.4	5.90	49.14					
9H-3, 62-63	69.4	4.88	40.66	6.17	1.29	0.16	1.20	8.18
10H-1, 82-83	72.4	4.65	38.76					
10H-1, 82-83	76.1	5.62	46.77	6.66	1.04	0.15	0.96	6.93
10H-3, 82-83	79.1	5.61	46.71					
10H-5, 82-83	82.1	5.38	44.77					
11X-1, 83-84	85.6	6.33	52.74					
11X-3, 82-83	88.6	4.28	35.66	6.12	1.84	0.18	1.36	10.14
11X-5, 99-100	91.8	5.61	46.75					
12H-1, 83-84	94.3	5.12	42.62	6.06	0.94	0.14	1.32	6.93
12H-2, 93-94	95.9	6.85	57.08					
12H-3, 83-84	97.3	6.20	51.61					
12H-5, 84-85	100.3	6.09	50.73					
14X-1, 78-79	113.5	6.86	57.14					
14X-3, 126-127	117.0	6.34	52.84					
14X-5, 78-79	119.5	4.97	41.36	6.57	1.60	0.17	1.04	9.22
15X-1, 42-43	122.7	5.45	45.41					
15X-3, 67-68	126.0	4.86	40.48	6.20	1.34	0.17	1.36	8.08
15X-5, 65-66	129.0	5.08	42.27	6.17	1.09	0.16	1.38	6.74
16X-1, 80-81	132.7	5.92	49.35					
16X-3, 80-81	135.7	5.75	47.88	7.18	1.44	0.15	0.88	9.57
16X-5, 62-63	138.5	6.58	54.79					
18X-1, 80-81	152.0	4.89	40.73	5.94	1.05	0.16	1.07	6.72
18X-3, 80-81	155.0	5.04	41.97	5.94	0.90	0.15	0.89	5.83
18X-5, 58-59	157.8	5.44	45.34					
19X-1, 73-74	161.6	5.09	42.37	6.20	1.12	0.17	1.04	6.63
19X-3, 73-74	164.6	6.05	50.40					
20X-1, 72-73	171.2	5.20	43.34	6.16	0.96	0.15	1.01	6.36
20X-3, 73-74	174.2	4.73	39.39	6.27	1.55	0.18	1.38	8.40
20X-5, 73-74	177.2	5.36	44.66					
21X-1, 21-22	180.3	3.75	31.21	5.02	1.27	0.16	0.99	7.76
21X-3, 76-77	182.9	4.66	38.84	6.08	1.42	0.16	1.07	8.74
21X-5, 76-77	185.8	4.77	39.73	5.99	1.22	0.17	1.09	7.29
22X-1, 49-50	190.3	3.67	30.60	6.421	0.83	0.14	0.91	5.80
22X-3, 38-39	193.2	4.06	33.78	4.755	0.62	0.13	1.07	4.64
22X-5, 39-40	196.2	4.04	33.68	5.23	1.19	0.17	1.10	6.96
172-1055B-								
1H-1, 63-64	0.6	6.52	54.31					
1H-2, 53-54	2.0	5.69	47.37					

Table 26 (continued).

Core, section, interval (cm)	Depth (mbsf)	IC (wt%)	$CaCO_3$ (wt%)	TC (wt%)	TOC (wt%)	TN (wt%)	TS (wt%)	C/N
1H-3, 54-55	3.5	3.29	27.41	4.21	0.92	0.13	0.43	7.07
2H-1, 78-79	5.3	3.85	32.04	4.92	1.08	0.14	0.27	7.69
2H-3, 84-85	8.3	3.92	32.63	4.59	0.68	0.08	0.19	8.44
2H-5, 85-86	11.4	4.51	37.53	4.82	0.31	0.06	0.02	5.22
3H-1, 77-78	14.8	6.58	54.82					
3H-3, 90-91	17.9	6.16	51.31					
3H-5, 83-84	20.8	6.62	55.12					
4H-1, 89-90	24.4	5.46	45.49					
4H-3, 122-123	27.7	3.56	29.68					
4H-5, 67-68	30.2	7.46	62.13	8.11	0.65	0.12	0.18	5.43
5H-1, 96-97	34.0	5.48	45.63					
5H-3, 61-62	36.6	5.67	47.21					
5H-5, 120-121	40.2	4.93	41.08	5.59	0.66	0.11	0.88	5.99
6H-1, 136-137	43.9	5.31	44.25					
6H-3, 76-77	46.3	5.15	42.92					
6H-5, 77-78	49.3	5.79	48.21					
7H-1, 86-87	52.9	6.38	53.17					
7H-3, 53-54	55.5	4.18	34.79	4.53	0.36	0.01	0.29	35.60
7H-5, 42-43	58.4	3.68	30.68					
8H-1, 54-55	62.0	5.25	43.75	3.98	0.30	0.06	0.17	5.00
8H-3, 64-65	65.1	5.17	43.04					
8H-5, 64-65	68.1	7.57	63.09					
10H-1, 77-78	81.3	6.33	52.70					
10H-3, 58-59	84.1	4.20	34.97	5.35	1.16	0.16	0.72	7.23
10H-5, 58-59	87.1	4.67	38.92	5.83	1.16	0.14	0.53	8.27
11H-3, 62-63	92.8	4.02	33.49	4.83	0.81	0.12	1.00	6.74
11H-5, 62-63	95.8	4.23	35.22	4.39	0.16	0.06	0.19	2.70
11H-7, 63-64	98.8	5.51	45.86					
12H-1, 58-59	100.1	2.78	23.15	3.02	0.24	0.07	0.04	3.44
12H-3, 58-59	102.7	4.00	33.28	4.59	0.60	0.09	0.13	6.61
12H-5, 58-59	105.7	5.24	43.65					
13H-3, 57-58	111.3	3.44	28.66	3.81	0.37	0.07	0.23	5.27
13H-5, 57-58	114.3	1.72	14.33	2.03	0.31	0.20	1.89	1.55
13H-8, 77-78	117.8	3.12	26.01	4.92	1.80	0.19	1.05	9.46
14H-3, 62-63	121.2	4.09	34.09					
14H-5, 62-63	124.2	3.16	26.31	4.66	1.50	0.19	1.39	7.91
14H-7, 61-62	127.1	3.78	31.49	5.88	2.10	0.19	1.43	11.05

Note: IC = inorganic carbon , TC = total carbon, TOC = total organic carbon, TN = total nitrogen, TS = total sulfur. Blank spaces indicate no measurements were made.

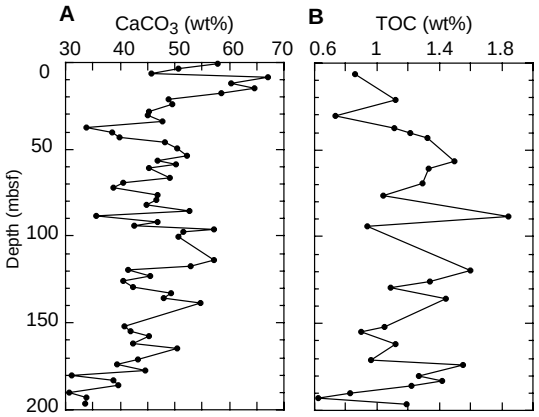

Figure 34. Downhole profiles of (**A**) calcium carbonate and (**B**) total organic carbon for Hole 1054A.

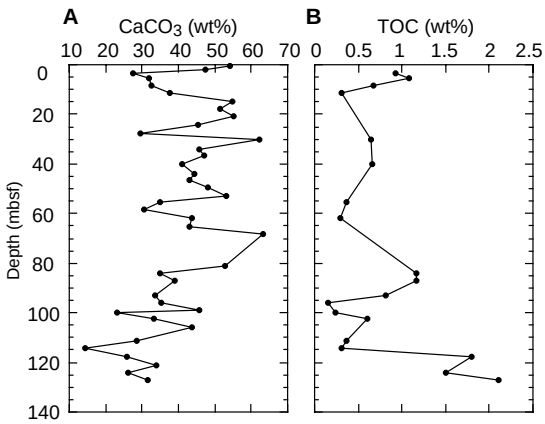

Figure 35. Downhole profiles of (**A**) calcium carbonate and (**B**) total organic carbon for Hole 1055B.

Again, the sedimentary organic matter here is interpreted to be largely refractory as a result of microbial degradation. Rock-Eval T_{max} values are low at all depths (Table 27), and indicate that organic matter is thermally immature with respect to petroleum generation.

Summary

Methane concentration and methane/ethane data indicate that gases are produced biologically throughout the two holes of the Carolina Slope. The methanogenic zone occurs higher in Hole 1055B. Furthermore, methane concentrations at Hole 1055B are greater than those at Hole 1054A. Carbonate and organic carbon concentrations are high at both sites. Heavily oxidized and refractory organic matter dominates, perhaps indicating a southward extension of the Cape Hatteras and Martha's Vineyard depocenter zones. Furthermore, sediments at both sites are thermally immature.

INORGANIC GEOCHEMISTRY

Interstitial waters were extracted and analyzed from 75 whole-round sections of core from Sites 1054 and 1055. Samples were collected from the bottom of every section in the upper part of Holes 1054A (Cores 172-1054A-1H through 4H) and 1055B (Cores 172-1055B-1H through 5H), and from every core thereafter. The main objectives were to document the early diagenetic changes and to locate

Table 27. Results of Rock-Eval analyses from Sites 1054 and 1055.

Core, section, interval (cm)	Depth (mbsf)	T_{max}	S_1	S_2	S_3	S_2/S_3	PC	HI	OI	PI
172-1054A-										
5H-1, 78-79	37.3	414	0.31	2.52	1.85	1.36	0.23	227	166	0.11
5H-3, 78-79	40.3	411	0.60	5.26	2.32	2.26	0.48	434	191	0.10
5H-5, 78-79	43.3	417	0.44	4.37	2.51	1.74	0.40	331	190	0.09
7H-1, 111-112	56.6	417	0.46	4.71	2.44	1.93	0.43	314	162	0.09
8H-1, 132-133	60.7	418	0.33	2.96	2.13	1.38	0.27	222	160	0.10
10H-1, 82-83	85.6	419	0.53	4.46	2.14	2.08	0.41	428	205	0.11
11X-3, 82-83	88.6	414	0.67	5.85	2.35	2.48	0.54	317	127	0.10
14X-5, 78-79	119.5	416	0.51	5.21	2.34	2.22	0.47	325	146	0.09
15X-3, 67-68	126	418	0.39	3.07	2.07	1.48	0.28	229	154	0.11
15X-5, 65-66	129	419	0.39	3.23	1.96	1.64	0.30	296	179	0.11
16X-3, 80-81	135.7	422	0.46	4.40	1.78	2.47	0.40	305	123	0.09
18X-1, 80-81	80-81	417	0.37	3.44	1.79	1.92	0.31	327	170	0.10
19X-1, 73-74	161.6	419	0.43	4.19	1.88	2.22	0.38	374	167	0.09
20X-3, 73-74	174.2	411	0.54	3.37	2.43	1.38	0.32	217	156	0.14
21X-1, 21-22	180.3	419	0.34	3.17	1.60	1.98	0.29	249	125	0.10
21X-3, 76-77	182.9	422	0.45	4.15	1.90	2.18	0.38	292	133	0.10
22X-5, 39-40	196.2	423	0.48	4.21	1.81	2.32	0.39	353	152	0.10
172-1055B-										
1H-3, 54-55	3.5	403	0.31	1.23	3.02	0.40	0.12	133	328	0.20
2H-1, 78-79	5.3	416	0.49	2.98	2.77	1.07	0.28	275	256	0.14
10H-3, 58-59	58-59	419	0.40	3.21	2.83	1.13	0.30	276	243	0.11
10H-5, 58-59	87.1	419	0.38	2.99	2.81	1.06	0.28	257	242	0.11
13H-8, 77-78	117.8	415	0.57	5.57	2.76	2.01	0.51	309	153	0.09
14H-5, 62-63	124.2	413	0.37	0.37	2.41	1.71	0.37	275	160	0.08
14H-7, 61-62	127.1	415	0.43	0.43	2.68	1.85	0.45	236	127	0.08

Note: PC = petroleum potential, HI = hydrogen index, OI = oxygen index, and PI = production index.

possible gas hydrate zones. Interstitial water data for the two sites are given in Table 28 and are presented as depth concentration profiles in Figures 38–42.

Early Diagenesis Associated with Organic Matter Degradation

Site 1054

Site 1054 data clearly show three early diagenetic zones associated with microbially mediated organic matter degradation: (1) an oxic to dysoxic zone in the upper 8 mbsf; (2) a sulfate reduction zone between 8 and 48 mbsf; and (3) the methanogenic zone below 48 mbsf (Table 28; Fig. 38).

Sulfate concentration decreases rapidly from near-seawater values at 8 mbsf to values less than 1 mM at 50 mbsf. The onset of sulfate reduction is accompanied by a rapid downhole increase in alkalinity (Fig. 38), resulting from microbial sulfate reduction:

$$SO_4^{2-} + 2CH_2O \rightarrow H_2S + 2HCO_3^-,$$

which produces two bicarbonate ions for every sulfate ion reduced. Active organic matter degradation in the sulfate reduction zone is also supported by high ammonium and phosphate concentrations between 20 and 30 mbsf, probably because of a local increase in organic matter remineralization (Fig. 38).

Complete sulfate consumption occurs at a depth of 48 mbsf and coincides with the onset of the microbially induced methanogenesis. Alkalinity and ammonium continue to increase with depth within the methanogenesis zone as HCO_3^- and NH_4^+ are added to pore water from microbial fermentation reactions (Claypool and Kaplan, 1974; Pedersen and Shimmield, 1991). Phosphate shows only minor change with depth below the sulfate reduction zone.

Site 1055

At Site 1055, the sulfate reduction zone is only ~25 m thick, and the onset of sulfate reduction starts close to the seafloor (Fig. 39). The shallower and thinner sulfate reduction zone at this site compared to Site 1054 is probably due to the labile nature of the sedimentary organic matter at Site 1055.

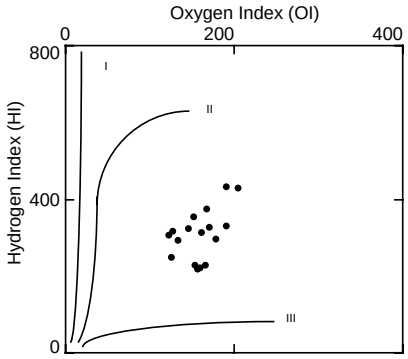

Figure 36. Rock-Eval van Krevelen-type diagram of sediments from Hole 1054A. HI = mg HC/g TOC, OI = mg CO_2/g TOC. The curves I, II, and III refer to trends of three types of organic matter: type I = algal, oil-prone organic matter; type II = marine, oil/gas-prone organic matter; and type III = terrestrial, gas-prone organic matter.

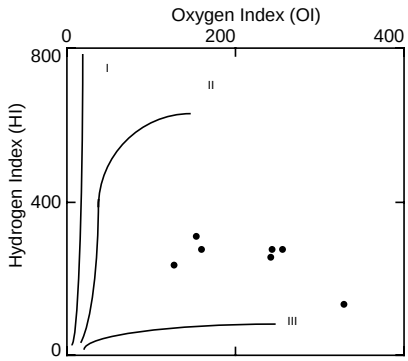

Figure 37. Rock-Eval van Krevelen-type diagram of sediments from Hole 1055B. Abbreviations and curve types as in Figure 36.

Table 28. Interstitial water analyses for Holes 1054A and 1055B.

Core, section, interval (cm)	Depth (mbsf)	pH	Alkalinity (mM)	Salinity	Cl (mM)	SO_4 (mM)	PO_4 (μM)	NH_4 (μM)	Na (mM)	Mg (mM)	Ca (mM)	K (mM)	SiO_2 (μM)
172-1054A-													
1H-1, 145-150	1.45	7.52	4.566	35.0	560	27.61	14	268	479	53.89	10.29	12.01	587
1H-2, 145-150	2.95	7.64	4.740	35.0	560	27.71	16	238	479	53.71	10.28	12.71	613
1H-3, 145-150	4.45			35.0	563	27.63	13	231	477	53.55	10.72	12.77	610
1H-4, 145-150	5.95	7.59	4.550	35.0	566	28.22	16	370	486	53.65	10.85	12.2	604
1H-5, 145-150	7.45	7.59	4.273	35.0	561	27.44	13	329	479	53.59	10.67	12.32	597
2H-1, 145-150	9.45	7.64	6.426	35.0	566	26.01	17	569	486	52.9	10.02	12.16	693
2H-2, 145-150	10.95	7.82	7.250	35.0	560	25.27	17	592	480	52.91	9.93	12.48	745
2H-3, 145-150	12.45	7.78	7.969	35.0	571	24.15	17	872	490	52.96	9.59	12.48	728
2H-4, 145-150	13.95	7.76		35.0	554	23.96	16	1059	467	51.77	9.41	3.04	795
2H-5, 145-150	15.45	8.02	9.148	35.0	567	22.98	27	872	488	51.75	9.21	13.06	840
2H-6, 145-150	16.95	7.89	9.950	35.0	567	22.97		1292	488	51.29	8.93	12.53	868
3H-1, 145-150	18.95	7.75	10.919	35.0	552	21.01	42	2528	476	49.78	9.87	12.05	799
3H-2, 145-150	20.45	7.63	10.949	35.0	559	19.06	39	779	474	51.16	8.75	12.35	834
3H-3, 145-150	21.95	7.58	12.776	35.5	505	20.63	63	872	432	47.53	9.88	11.4	866
3H-4, 145-150	23.45			36.0	594	19.79	29	1035	497	51.42	10.25	12.88	905
3H-5, 145-150	24.95	7.73	14.637	36.0	569	17.94	63	1268	490	50.01	10.2	12.84	990
3H-6, 145-150	26.45	7.71	16.225	36.0	581	16.88	139	1220	506	48.54	8.54	12.97	1094
4H-1, 145-150	28.45	8.22	19.390	35.0	563	13.02	19	7320	486	47.24	7.46	12.84	
4H-2, 145-150	29.95	8.07	21.173	35.0	573	12.25	17	9190	497	47.14	7.46	12.48	
4H-3, 145-150	31.45	8.10	21.770	34.5	570	12.12	24	965	496	46.38	7.36	12.68	764
4H-4, 145-150	32.95	8.22	21.211	35.0	564	11.41	42	965	489	46.06	7.48	12.42	877
4H-5, 145-150	34.45	8.24	23.552	34.5	572	10.47	40	965	498	45.93	7.2	12.91	
4H-6, 145-150	35.95	8.23	23.776	35.5	564	10.3	24	919	493	45.52	6.92	12.48	849
5H-5, 145-150	43.9	8.19	28.734	34.0	576	3.37	26	1250	502	42.51	6.15	12.7	
6H-4, 140-150	51.9	8.03	33.477	34.0	567	0	35	1712	496	40.05	5.67	12.93	
7H-1, 140-150	56.9	8.16	35.197	34.5	572	0.67	40	2365	505	39.99	5.86	12.73	855
8H-3, 140-150	63.8	8.13	37.656	34.0	571	0.06	26	3437	506	39.45	5.65	13.02	
9H-2, 140-150	67.45	8.08	39.047	34.0	564	0.01	37	1947	502	39.06	5.26	13.02	
10H-5, 140-150	82.7	7.70	43.124	34.0	559	0.15	37	2878	502	38.39	5.03	13.25	
11X-6, 140-150	93.7	7.49	41.203	34.5	557	0.47	35	3204	499	38.07	5.37	13.26	868
12X-4, 140-150	100	7.52	50.727	35.5	555	0.14	39	3997	508	37.3	5.48	13.36	914
13X-4, 140-150	108.9	6.94	52.909	34.5	556	0.01	40	3764	510	37.26	5.16	13.52	886
14X-4, 140-150	118.6	7.55	55.790	34.5	556	0	32	4137	514	37.34	5.2	13.83	847
15X4, 140-150	128.2	7.61	55.803	34.0	557	0.21	30	4734	517	36.35	4.44	14.01	823
16X-4, 135-150	137.75	7.55	58.915	34.0	558	0.62	37	5256	520	37.43	4.83	14.26	860
18X-4, 140-150	154.1	7.47	61.458	34.5	561	0.06	40	5723	525	36.88	4.32	14.89	881
19X-2, 140-150	163.8	7.12	65.244	35.0	555	0.52	43	4650	524	36.65	4.6	14.97	892
20X-2, 140-150	173.4	7.31	64.181	35.0	546	0.14	45	6096	513	37.02	4.43	14.96	878
21X-2, 140-150	182.06	7.26	53.051	35.0	551	0.57	45	8148	507	37.29	4.45	15.47	915
22X-4, 140-150	195.7	7.48	67.767	35.5	555	0.15	43	6049	535	36.36	4.18	15.83	865
172-1055B-													
1H-1, 145-150	1.45	7.45	3.875	35.5	561	27.43	21		482	52.43	10.42	12.4	552
1H-2, 145-150	2.95	7.42	4.727	35.5	559	27.2	47		480	52.52	10.34	12.63	626
2H-2, 145-150	5.95	7.49	6.583	35	562	25.3	54	1736	483	52.29	9.48	12.3	635
1H-4, 145-150	7.45	7.42	7.548	35	565	24.12	69	2734	488	51.48	8.78	12.37	700
2H-3, 145-150	8.95	7.49	8.284	35	561	22.55	74	2995	483	51.13	8.16	12.48	693
2H-4, 145-150	10.45	7.57	9.013	35	565	21.06	83	3212	488	50.38	7.48	12.33	763
2H-5, 145-150	11.95	7.57	9.861	35	562	20.79	58	3169	486	50.57	7.1	12.3	628
2H-6, 145-150	13.7	7.47	10.28	34.5	561	19.39	86		485	49.34	6.61	12.88	696
3H-1, 145-150	15.45	7.62	13.94	34	566	11.92	114	2778	492	45.65	4.17	12.59	754
3H-2, 145-150	16.95	7.66	16.36	34	559	9.94	106	2344	485	44.68	3.89	12.89	795
3H-3, 145-150	18.45	7.62	16.95	34	562	8.76	120	3429	490	43.4	3.75	12.47	780
3H-4, 145-150	19.95	7.69	17.87	33.5	560	7.13	164	3212	487	42.58	3.53	13.06	778
3H-5, 145-150	21.45	7.83	18.23	33.5	564	5.66	125	1822	492	40.85	3.35	12.77	706
3H-6, 145-150	22.95	7.8	19.63	33	566	4.01	111	3646	495	39.91	3.36	12.28	663
4H-1, 145-150	24.95	7.73	21.78	32.5	571	0.47	119	3212	500	38.11	2.95	11.68	685
4H-2, 145-150	26.45	7.55	21.04	32.5	561	0.27	95	4124	492	36.26	2.72	12.89	683
4H-3, 145-150	27.95	7.72	21.16	32.5	561	0.06	103		491	36.4	2.64	12.71	758
4H-4, 145-150	29.45	7.75		32.5	553	0.11	121	4037	462	36.44	3.14	12.12	717
4H-5, 145-150	30.95	7.82	20.4	32.5	567	0	124	5514	499	35.12	2.61	12.83	754
4H-6, 145-150	32.45	7.57	20.72	32.5	563	0.2	124	5427	495	35.03	2.75	13.24	810
5H-1, 145-150	34.45	7.4	21.2	32.5	562	0.05	124	5818	495	34.71	3.05	12.57	856
5H-2, 145-150	35.95	7.63	21.32	32.5	567	0.77	144	6035	501	34.82	3.23	12.93	860
5H-3, 140-150	37.4	7.7	21.42	33	564	0.45	147	5167	499	34.19	2.94	12.63	878
5H-4, 140-150	38.9	7.69	21.63	32.5	570	0.61	156	6469	505	34.32	3.1	13.29	882
5H-5, 140-150	40.4	7.67	22.5	32.5	565	0.44	161	6165	500	34.43	3.37	12.5	852
5H-6, 140-150	41.9	7.75	23.06	32.5	567	0.09	140	7208	501	35.18	3.36	12.19	771
6H-5, 140-150	49.9	7.69	24.8	33	566	0.39	151		503	34.74	3.05	12.71	791
7H-6, 140-150	60.9	7.52	29.09	34	557	0.26	166	8728	496	35.69	2.38	14.28	763
8H-6, 140-150	70.4	7.78	31.61	34	558	0.1	159	9813	499	36.14	2.29	13.99	767
9H-5, 140-150	78.4	7.94	34.43	34	561	0	188	10248	504	35.89	2.68	13.8	906
10H-6, 140-150	89.4	7.91	38.65	34	569	0.56	204		516	36.49	2.74	13.96	947
11H-7, 140-150	98.69	8.03	40.45	34.5	572	0.29	205	9466	520	36.21	2.59	15.71	758
12X-6, 140-150	108	7.94	40.97	35	570	0.35	238	9770	517	37.16	3.09	14.31	906
13X6, 140-150	116.7	7.54	42.9	35	565	0	201		517	33.88	2.64	17.5	808
14X-6, 135-150	126.4	7.63	48.47	35	565	0.17	224	12723	520	35.88	3.55	15.1	860

Note: Blank spaces indicate no measurements were made.

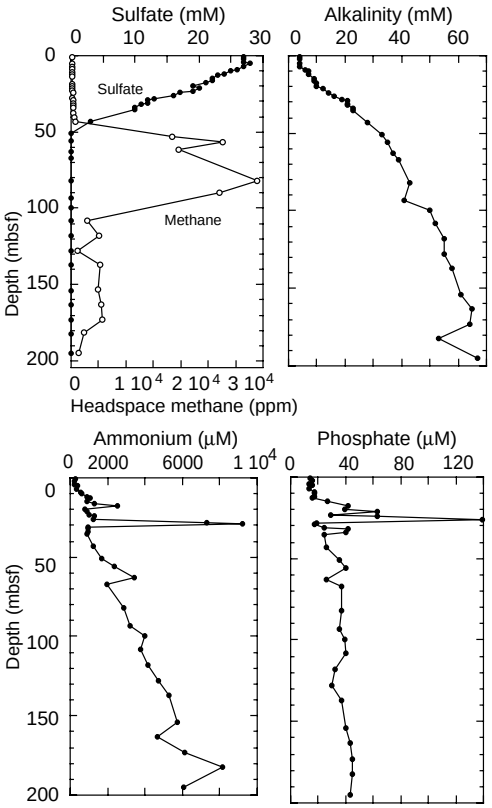

Figure 38. Concentration vs. depth profiles for interstitial waters, Hole 1054A.

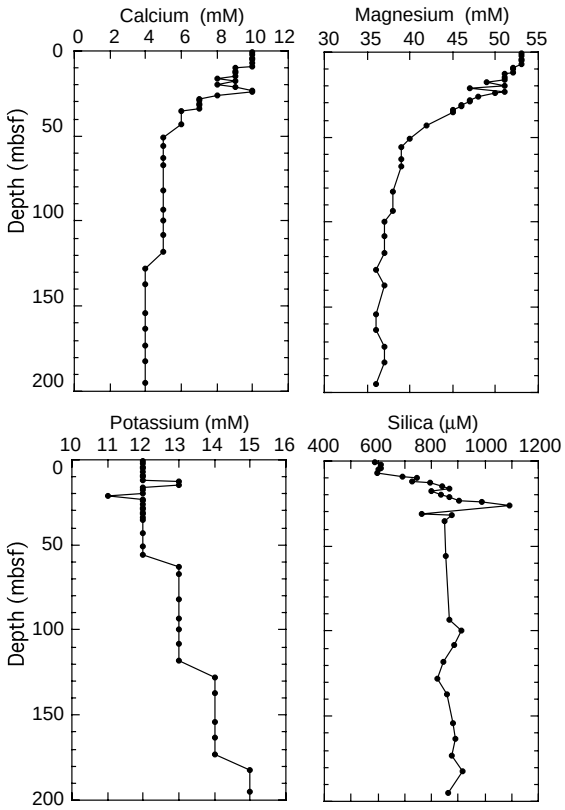

Figure 40. Concentration vs. depth profiles for interstitial waters, Hole 1054A.

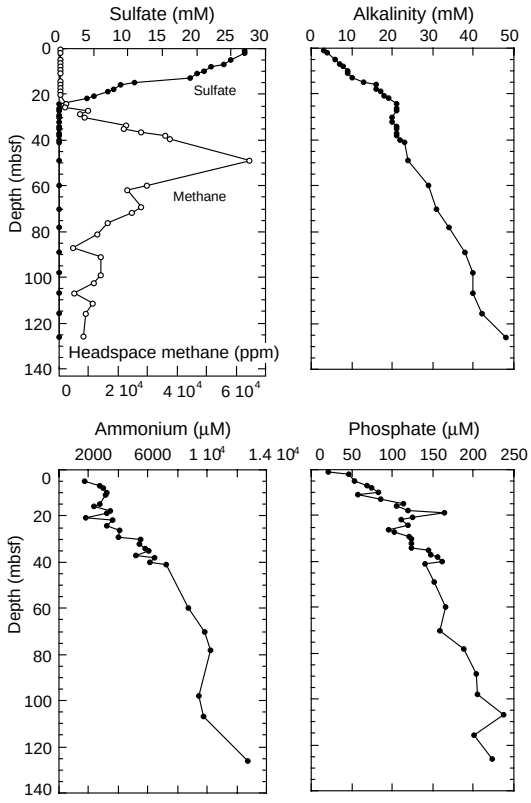

Figure 39. Concentration vs. depth profiles for interstitial waters, Hole 1055B.

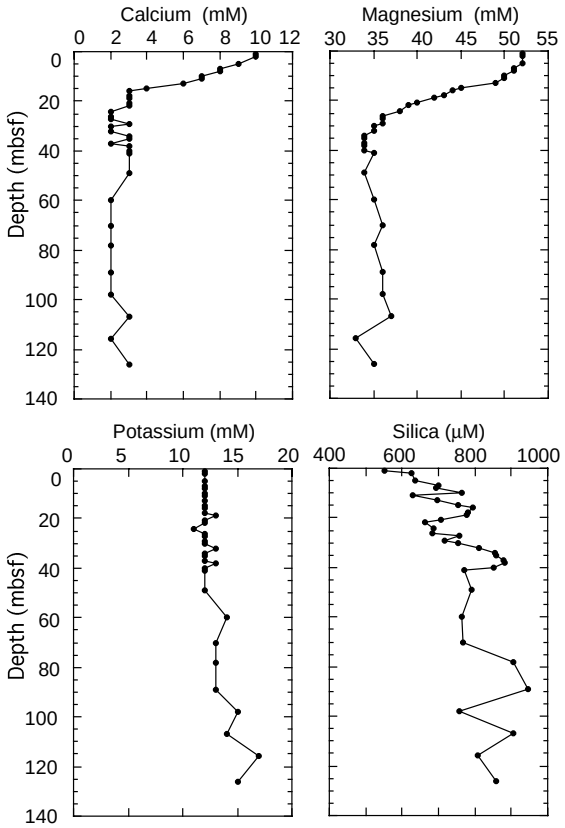

Figure 41. Concentration vs. depth profiles for interstitial waters, Hole 1055B.

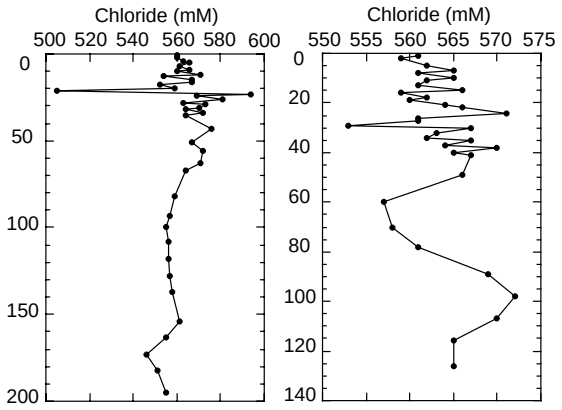

Figure 42. Downhole chloride profiles for Holes 1054A and 1055B.

Alkalinity increases rapidly with depth, producing a peak value of 22 mM at the sulfate/methane interface (Fig. 39). The depth of complete sulfate depletion again coincides with a rapid increase in the volume of methane (Fig. 39). Alkalinity increases with depth in the zone of methanogenesis, although at a lesser rate than at Site 1054. Ammonia and phosphate concentrations also increase with depth, but at greater rates than those at Site 1054 (Fig. 39).

Authigenic Mineral Precipitation

Site 1054

Calcium and magnesium concentrations of interstitial waters decrease with depth from near-seawater values, showing a diffusive flux of these ions from overlying seawater into the sediment (Fig. 40). At 48 mbsf (at the base of the sulfate reduction zone), the magnesium and calcium concentrations decrease by ~25% and 50%, respectively, from their high values near the seafloor. This decrease is probably due to precipitation of carbonate minerals in the methanogenic zone. This conclusion is supported by the presence of carbonate (mainly dolomite) nodules at various intervals in the sediment column (see "Lithostratigraphy" section, this chapter). Local increases in calcium and magnesium within the sulfate reduction zone probably indicate dissolution of biogenic carbonate material (e.g., Gieskes, 1981). Magnesium may also be involved in ion exchange reactions with clay minerals in the methanogenesis zone (Gieskes, 1981).

Potassium shows increasing concentration with depth (Fig. 40). This trend is most likely caused by replacement of potassium with ammonium at clay-mineral exchange sites as the concentration of ammonium builds up in the lower part of the sediment column (e.g., Rosenfeld, 1979; Mackin and Aller, 1984).

Dissolved silica concentration generally reflects lithologic changes in sediments. In Hole 1054A the silica concentrations increase with depth and reach a maximum value of ~1100 µM at a depth of 27 mbsf (Fig. 40). This value, being close to the solubility limit of opal-A (Kastner, 1979), suggests that dissolution of siliceous tests (e.g., diatoms) is occurring. Diatoms are known to be present in the sedimentary section (see "Biostratigraphy" section, this chapter).

Site 1055

The trends of calcium and magnesium in interstitial waters at Site 1055 are similar to those observed at Site 1054. Sharp decreases in the concentrations of these two cations are observed in the zone of sulfate reduction (Fig. 41). At the top of the methanogenesis zone, both calcium and magnesium reach their minimum values, which are 80% and 33% less, respectively, than their values near the seafloor. These decreasing concentrations suggest a sink for these species at an active diagenetic front of carbonate formation near the top of the methanogenesis zone. A small but distinct decrease in alkalinity, together with the increase in dolomite content of the sediments at the same depth interval, indicates that the sulfate/methane interface is an active zone of carbonate precipitation. Both the calcium and magnesium concentrations remain low in the lower part of the sediment column, suggesting carbonate precipitation throughout the methanogenic zone.

As at Site 1055, potassium concentration increases with depth (Fig. 41), strongly suggesting active ion exchange processes. High silica values (>850 µM) at intervals between 30 and 40 mbsf and 75 and 90 mbsf are probably related to the dissolution of opaline tests (Fig. 41).

Gas Hydrate

Although both Sites 1054 and 1055 lie in a well-characterized gas hydrate terrane (see "Introduction" chapter, this volume), there are no unequivocal geochemical indications of gas hydrate (Fig. 42). Marked variation in chloride concentration can represent the presence of gas hydrate (Hesse and Harrison, 1981; Kvenvolden and Kastner, 1990). Although chloride values here typically vary by only 1%, two successive samples at Site 1054 (Samples 172-1054A-3H-3, 145–150 cm, and 3H-4, 145–150 cm) show variations of –10% and +5%, respectively, from the seawater chloride concentration of 559 mM. However, this occurrence is located within the sulfate reduction zone where methane concentrations are insufficient to induce gas hydrate formation. In short, clear, diffusive gradients of chloride like those present at Leg 164 sites (Sites 994, 995, and 997; [Paull, Matsumoto, Wallace, et al., 1996]**)** are absent, suggesting that no gas hydrate was recovered in cores from the Carolina Slope sites.

PHYSICAL PROPERTIES

Millennial-scale oceanographic changes in the waters overlying the Carolina Slope modulate both sediment supply and the pattern of sedimentation. Downslope and contour-parallel depositional processes, the composition of sediment deposited, and postdepositional changes related to either stress or diagenesis all influence the sediments accumulating on the Carolina Slope. The result of this complex interplay of processes is a vertically heterogeneous sediment column (see "Lithostratigraphy" section, this chapter), reflecting erosion and deposition from turbidity currents, debris flows, contour currents, and hemipelagic processes. Naturally occurring gases also exerted an influence on physical properties (both in situ and through the formation of voids as the gas expands) during core recovery, thus cracking and distorting the sediments. These deformations noticeably influenced the quality of the physical property measurements below 65 mbsf at Site 1054 and below 40 mbsf at Site 1055.

At Sites 1054 and 1055, the MST provided data sets for hole-to-hole correlations (see "Stratigraphic Correlation" section, this chapter) compatible with investigating the influence of millennial-timescale (centimeter-depth scale) variations on the physical properties of recovered sediments. Additional laboratory measurements on the working halves of cores of acoustic compressional wave velocity, shear strength, index properties, and resistivity, as well as thermal conductivity measurements on whole-round cores, provided lower resolution (meter-scale) information less influenced by gas expansion voids.

MST Measurements

The MST provided high-resolution, nondestructive measurements on whole-round cores from the Carolina Slope using four different sensors. At Sites 1054 and 1055, GRAPE density and magnetic susceptibility were measured at 5-cm intervals on all cores from all holes. The *P*-wave logger (PWL) was also used at 5-cm intervals, but

was switched off when the signal became too attenuated for reliable velocity readings (below ~50 mbsf at both sites). Holes 1054A (Cores 172-1054A-9H through 22X), 1054B (Cores 172-1054B-1H through 9H), 1055B, and 1055C were measured with the natural gamma-ray sensor at 50-cm intervals.

MST-measurements from Sites 1054 and 1055 (Figs. 43, 44) show that GRAPE and magnetic susceptibility data become much noisier below 70 and 40 mbsf, respectively, because of the increasing number of cracks and voids caused by gas expansion in the cored sediment. This change correlates with lower thermal conductivity and shear-strength values (see below).

Site 1054

MST data from Site 1054 show low-amplitude variability, punctuated by occasional high values associated with downslope deposits. Magnetic susceptibility is low, with most values between 2 and 8×10^{-5} SI, and generally co-varies with total natural gamma-ray measurements, suggesting susceptibility is primarily controlled by paramagnetism of clay minerals (Hoppie et al., 1994). GRAPE values are typically around 1.6 g/cm^3. Thin (10–30 cm), high-density (up to 2.2 g/cm^3) beds occur within lithologic Unit II (Fig. 43). These beds are characterized by a sharp (<4 cm) density increase at their base, followed by a more gradual decrease to background levels and are associated with more coarsely grained mass transport deposits (see "Lithostratigraphy" section, this chapter). A distinct bulk density low (1.47 g/cm^3) occurs between 60 and 65 mbsf in Hole 1054A (and is also observed in Holes 1054B and 1054C) and may correspond to a zone of higher biogenic silica productivity and/or preservation.

In general, intervals of higher density are associated with higher L* reflectance values (see "Lithostratigraphy" section, this chapter), suggesting high densities caused by higher carbonate contents. On the other hand, low-density intervals contain increased biogenic silica. However, the observed pattern cannot be readily related to large-scale (Milankovitch) climate cycles. This may be due to several factors: (1) relatively low sedimentation rates (15 m/m.y. over the last 0.5 m.y. and 120 m/m.y. before this—see "Biostratigraphy" section, this chapter) combined with bioturbation "smear" from the climatic signal; (2) low variability in the physical characteristics of sediment deposited in glacial and interglacial periods; or (3) the removal of glacial-age sediment by increased margin slumping during sea-level minima above gas hydrate-bearing sediments (see "Lithostratigraphy" section, this chapter)

Compressional wave velocity exhibits a positive correlation with GRAPE density in most parts of the record. On the other hand, the relationship between acoustic parameters and magnetic susceptibility variations is more complex. Intervals with positive, negative, or no correlation occur over short depth ranges (Fig. 45).

Site 1055

MST records from Site 1055 (Fig. 44) are dominated by meter-scale cycles (wavelength 8–18 m) in all parameters (Fig. 45). Based on the available age control (see "Biostratigraphy" section, this chapter) the observed cycles occur at a frequency of 100 k.y., suggesting they are caused by orbitally induced climate change (Milankovitch cycles). Higher values in all parameters occur during glacial periods. Magnetic susceptibility is generally low ($5–15 \times 10^{-5}$ SI), except for the interval from 0 to 15 mbsf, where the presence of authigenic pyrite contributes to the overall susceptibility, with values up to $50 \text{ SI} \times 10^{-6}$. As at Site 1054, magnetic susceptibility covaries closely with total natural gamma-ray measurements (with the exception of the 0–15-mbsf interval), suggesting susceptibility is primarily controlled by paramagnetic clay minerals.

Compressional wave velocity ranges from 1410 to 1480 m/s. High-velocity layers are associated with high GRAPE density, and occur during glacial periods.

At Site 1055, higher GRAPE density values are associated with lower L* reflectance values (see "Lithostratigraphy" section, this chapter), in marked contrast to the relationship seen at Site 1054. This suggests that glacial periods (which are low in carbonate) are dominated by heavier minerals (the most obvious example of which is he-

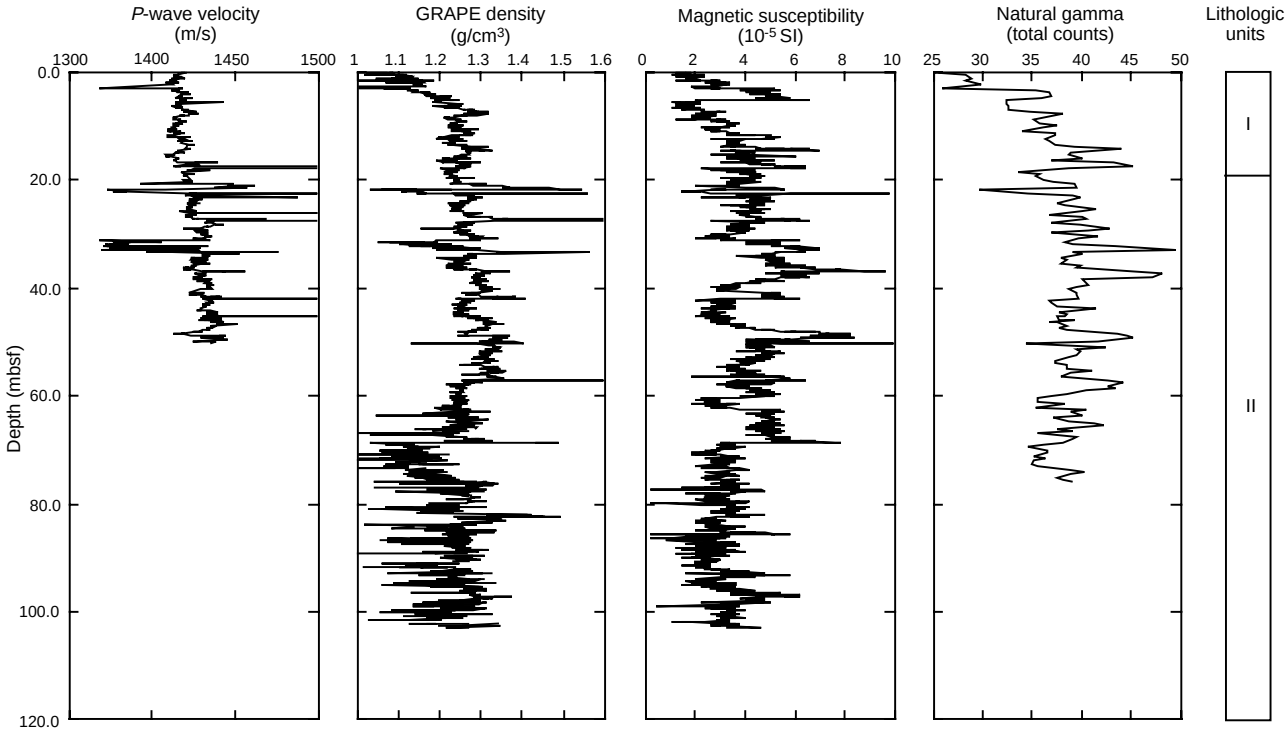

Figure 43. Vertical profiles of MST data from Hole 1054B.

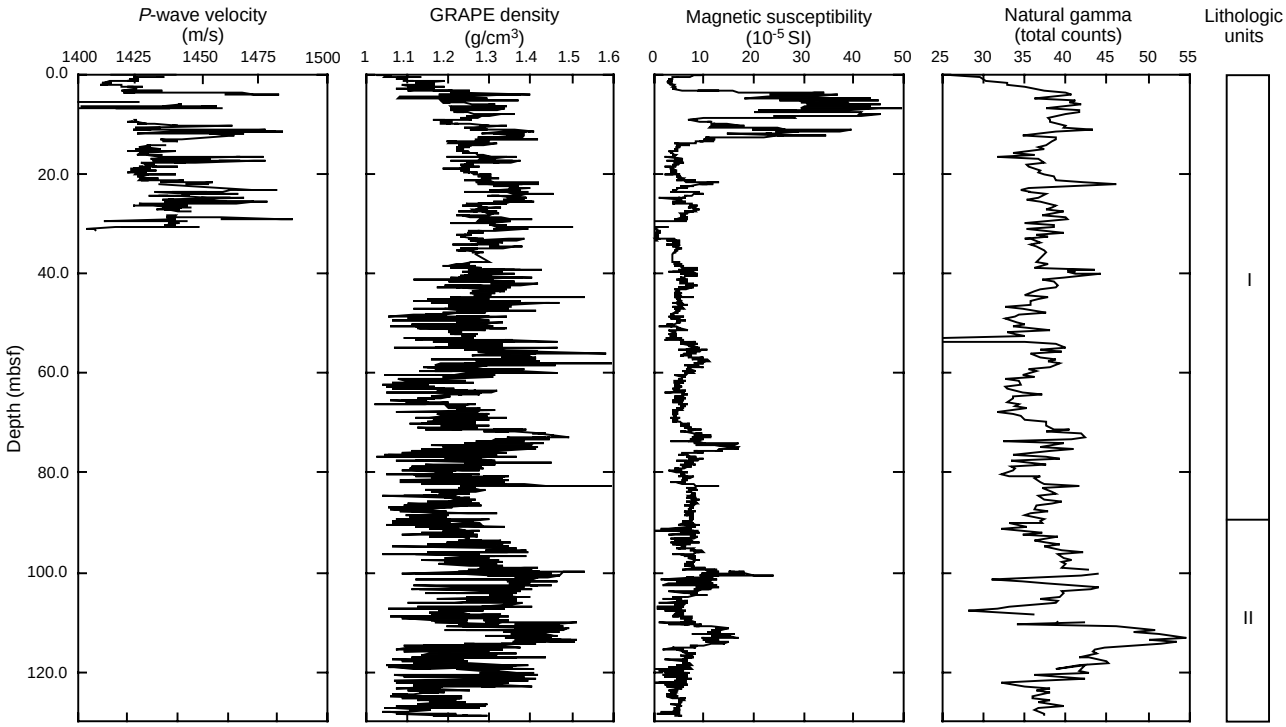

Figure 44. Vertical profiles of MST data from Hole 1055B.

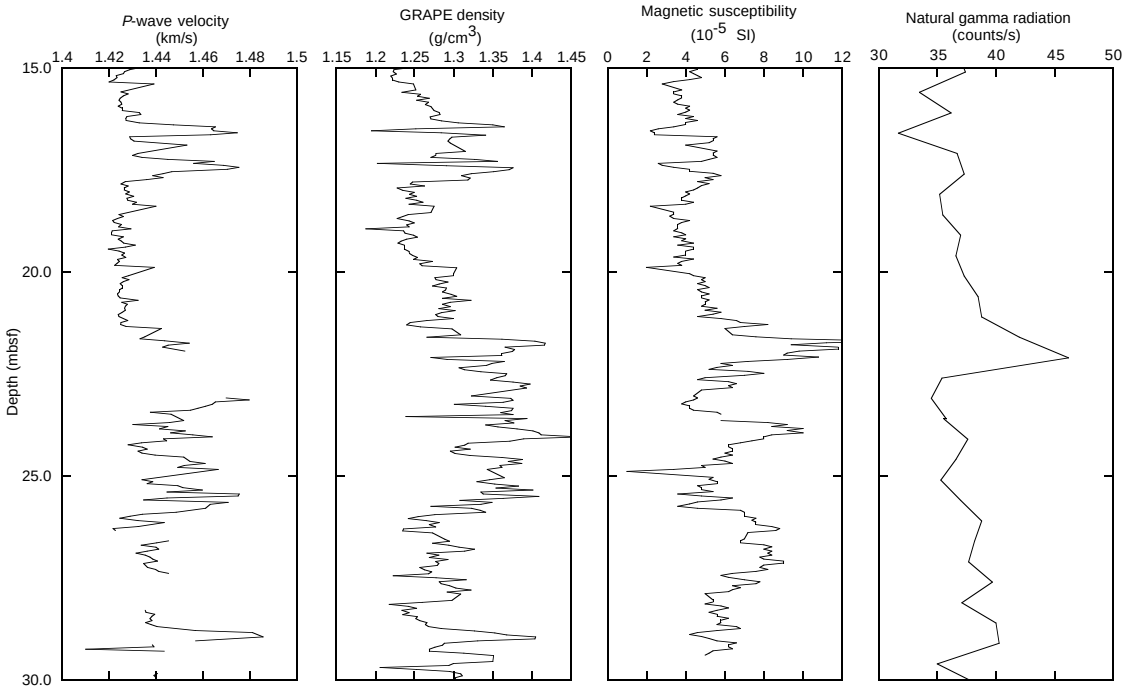

Figure 45. Comparison of decimeter-scale variations in *P*-wave velocity, GRAPE density, magnetic susceptibility, and natural gamma radiation at Hole 1055B.

matite) rather than biogenic silica, which appears to be a major glacial component at Site 1054. This view is supported by the much lower abundance of diatoms observed at Site 1055 compared with Site 1054 (see Table 5). In this regard Site 1055 appears to be much more closely related genetically to the Intermediate Depth Blake-Bahama Ridge sites than Site 1054.

Index Properties and Velocity Measurements on Split Cores

Index properties were sampled at three per core (in Holes 1054A and 1055B) at both sites, and thus do not resolve the shorter wavelength vertical variations seen with the MST. Nevertheless, the larger

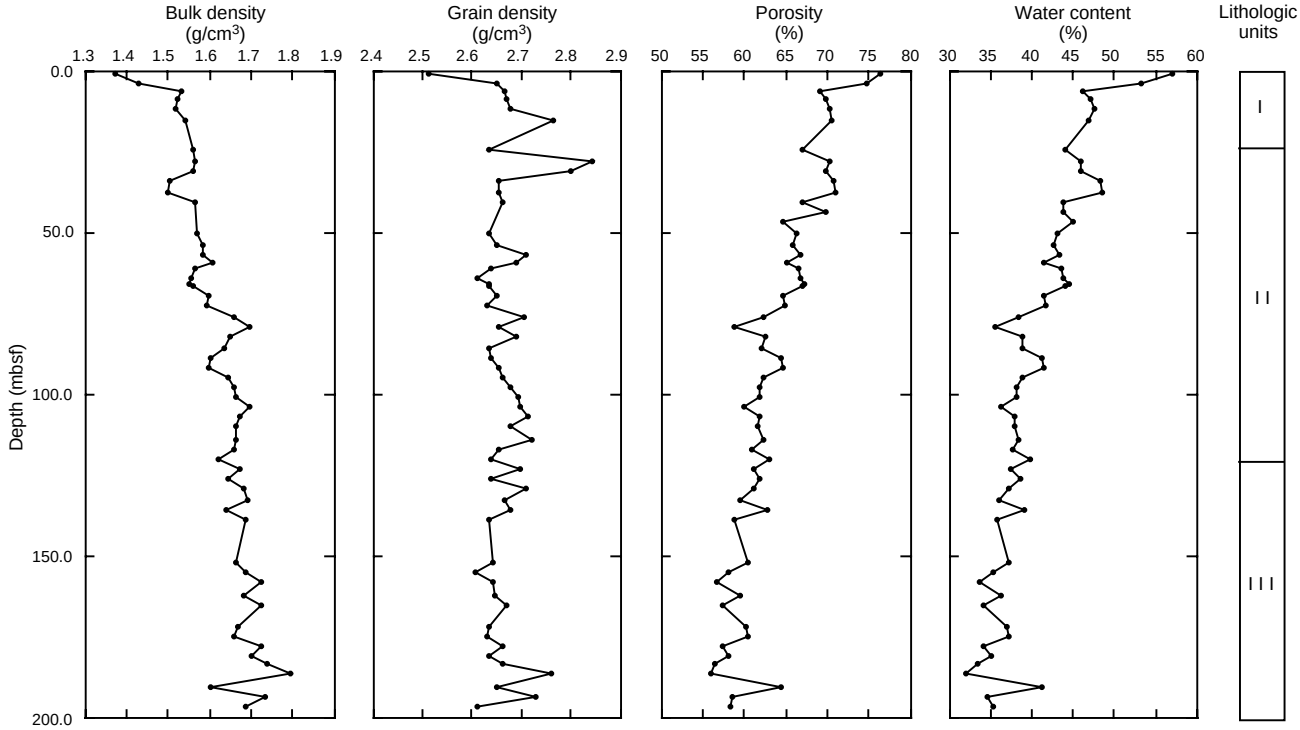

Figure 46. Index properties measurements of wet bulk density, grain density, porosity, and water content vs. depth for Hole 1054A.

Table 29. Index properties of samples from Site 1054.

Leg	Site	Hole	Core	Type	Section	Top	Bottom	Depth (mbsf)	Water content wet (%)	Water content dry (%)	Wet bulk density (g/cm^3)	Grain density (g/cm^3)	Dry density (g/cm^3)	Porosity (%)	Void ratio
172	1054	A	1	H	1	88	90	0.88	56.87	131.85	1.37	2.51	0.59	76.39	3.23
172	1054	A	1	H	3	84	86	3.84	53.29	114.1	1.43	2.65	0.67	74.74	2.96
172	1054	A	1	H	5	40	42	6.4	46.22	85.94	1.53	2.66	0.82	69.1	2.24
172	1054	A	2	H	1	55	57	8.55	47.04	88.81	1.52	2.67	0.81	69.82	2.31
172	1054	A	2	H	3	74	76	11.74	47.47	90.38	1.52	2.68	0.8	70.25	2.36
172	1054	A	2	H	5	103	105	15.03	46.91	88.37	1.54	2.77	0.82	70.47	2.39
172	1054	A	3	H	5	79	81	24.29	43.97	78.48	1.56	2.63	0.87	66.87	2.02
172	1054	A	4	H	1	93	95	27.93	45.9	84.84	1.57	2.84	0.85	70.19	2.35
172	1054	A	4	H	3	69	71	30.69	45.89	84.81	1.56	2.8	0.84	69.86	2.32
172	1054	A	4	H	5	94	96	33.94	48.21	93.07	1.5	2.66	0.78	70.7	2.41

This is a sample of the table that appears on the volume CD-ROM.

scale trends in density-related properties were delineated to the bottom of both holes with better reliability than the MST.

Site 1054

Bulk density increases rapidly in the upper 10 m of Hole 1054A from 1.37 to 1.531 g/cm^3 at 6.4 mbsf (Fig. 46; Table 29). Below this there is a steady, gradual increase in bulk density to a peak value of 1.91 g/cm^3 at 185.76 mbsf. Bulk density cycles are primary driven by changes in water content, whereas grain density remains relatively constant throughout. Water content exhibits a similar but reversed pattern, falling from a peak of 56.9% (percent wet weight) in sediment from the surface to a low of 31.9% at 11 m in core from the bottom of the hole. Porosity behaves similarly, falling to 55.8% at 185.76 mbsf. Grain densities average 2.658 g/cm^3. Three samples above 2.75 g/cm^3 from the upper 44 mbsf may reflect the presence of dolomite layers within the sediments (see "Lithostratigraphy" section, this chapter) or, alternatively, these data could be unreliable because there are no corresponding high GRAPE values at the intervals these samples were taken from.

Bulk densities measured on discrete samples and by the GRAPE agree in trend for the upper 55–60 mbsf, the depth at which gassy sediments became common. Common cracking and distortion of the sediment through gas expansion within the core liner combined with the 5-cm sampling resolution of the GRAPE presumably led to measurements of water and gas-filled cracks by the GRAPE and the subsequent drop in apparent bulk densities. Sampling for bulk density and other index properties allowed us to avoid the numerous cracks and obtain measurements more representative of subseafloor conditions than those obtained with the MST.

Site 1055

The index properties observed at Hole 1055B (Table 30) show the same cyclicity observed in the MST data (see above and Fig. 47, Table 31). Bulk density exhibits a rapid increase in core from the upper four meters, from 1.337 g/cm^3 at 0.65 mbsf to 1.566 g/cm^3 at 3.98 mbsf. Below this level, bulk density increases more slowly and with greater variability. Glacial periods are characterized by higher grain densities (2.75–2.8 g/cm^3) and lower water content than interglacials

Table 30. Index properties of samples from Site 1055.

Leg	Site	Hole	Core	Type	Section	Top	Bottom	Depth (mbsf)	Water content wet (%)	Water content dry (%)	Wet bulk density (g/cm^3)	Grain density (g/cm^3)	Dry density (g/cm^3)	Porosity (%)	Void ratio
172	1055	B	1	H	1	65	67	0.65	61.96	162.84	1.33	2.66	0.5	80.89	4.23
172	1055	B	1	H	2	54	56	2.04	56.04	127.47	1.13	1.32	0.5	62.3	1.65
172	1055	B	1	H	2	124	126	2.74	56.64	130.65	1.39	2.67	0.6	77.32	3.41
172	1055	B	1	H	3	56	58	3.56	49.52	98.11	1.49	2.68	0.75	71.95	2.56
172	1055	B	1	H	3	98	100	3.98	44.36	79.73	1.57	2.71	0.87	67.85	2.11
172	1055	B	2	H	1	80	82	5.3	49.47	97.89	1.48	2.64	0.75	71.6	2.52
172	1055	B	2	H	3	81	83	8.31	45.31	82.85	1.56	2.76	0.85	69.04	2.23
172	1055	B	2	H	4	61	63	9.61	50.47	101.87	1.47	2.68	0.73	72.73	2.66
172	1055	B	3	H	1	27	29	14.27	49.21	96.88	1.49	2.69	0.76	71.77	2.54
172	1055	B	3	H	3	17	19	17.17	46.43	86.66	1.53	2.66	0.82	69.22	2.25

This is a sample of the table that appears on the volume CD-ROM.

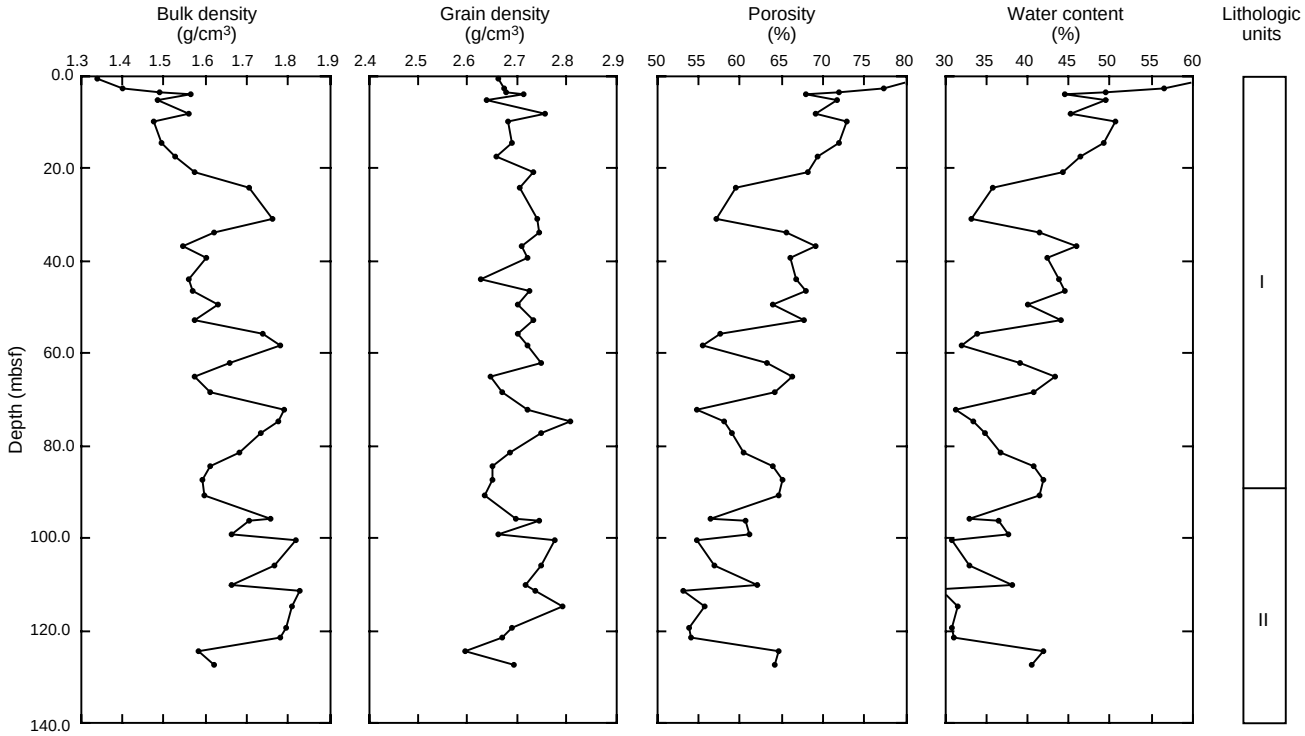

Figure 47. Index properties measurements of wet bulk density, grain density, porosity, and water content vs. depth for Hole 1055B.

Table 31. Average values and standard deviation of index properties measured at Holes1054A and 1055B.

Hole	Bulk density (g/cm^3)	Grain density (g/cm^3)	Porosity (%)	Water content (% wet weight)
1054A	1.615 ± 0.82	2.658 ± 0.097	63.8 ± 4.7	40.7 ± 5.1
1055B	1.650 ± 1.32	2.701 ± 0.046	63.6 ± 7.5	39.8 ± 7.9

(grain density = 2.63–2.67 g/cm^3), thus producing the distinct bulk density cycles. Porosity and water content both decrease with depth, exhibiting the same higher level of variability seen in bulk density (Table 31).

The higher average grain density and standard deviation at Hole 1055B (2.701 and 0.046 g/cm^3, respectively), when compared to Site 1054 (2.658 and 0.097 g/cm^3, respectively; see also Table 31), are probably caused by the much lower abundance of biogenic silica (grain density = 1.89 g/cm^3) and higher heavy mineral content at Site 1055.

Velocity on split cores in longitudinal and transverse directions was measured in the uppermost 50 to 60 mbsf of each site at a resolution of three per core (Tables 32, 33). Values of discrete velocity from Sites 1054 and 1055 are generally higher than those obtained by the PWL; however, in both cases of the PWL the high gas content of the sediments precludes the recovery of high-quality data.

Vane Shear

Undrained shear strength (Tables 34, 35) is a measure of the development of sediment grain-to-grain and of physico-chemical bonds. This property is measured under no confining stress and is therefore described as a “friction angle (f) = 0” test obtained under no equivalent depth (stress) below the seafloor.

A comparison of shear-strength measurements (S_u) at Sites 1054 and 1055 (Fig. 48) shows that shear strength increases more rapidly with depth in core from the upper 60 mbsf of Site 1054. Below this depth in both records similar average values (30 kPa) were detected, but shear-strength values show more variability at Site 1054. At this site, remarkably low shear strength (7–12 kPa) is observed in core

Table 32. Compressional wave velocity measurements from Site 1054.

Leg	Site	Hole	Core	Type	Section	Interval (cm)	Depth (mbsf)	Temp. (°C)	Velocity 1 Z-direction (m/s)	Velocity 2 Y-direction (m/s)	Velocity 3 X-direction (m/s)
172	1054	A	3	H	1	31	17.81	19.4	1501	1491	
172	1054	A	3	H	3	75	21.25	19.7	1524		
172	1054	A	3	H	5	79	24.29	19.9		1551	
172	1054	A	4	H	1	93	27.93	20.2		1533	
172	1054	A	4	H	3	69	30.69	20.3	1552	1544	
172	1054	A	4	H	5	95	33.95	20.1	1523	1508	
172	1054	A	5	H	1	87	37.37	19.8	1517	1515	
172	1054	A	5	H	3	80	40.3	19.8	1535	1545	
172	1054	A	5	H	5	80	43.3	20.3	1526	1535	
172	1054	A	5	H	5	106	43.56	20.5			1572

This is a sample of the table that appears on the volume CD-ROM.

Table 33. Compressional wave velocity measurements from Site 1055.

Leg	Site	Hole	Core	Type	Section	Interval (cm)	Depth (mbsf)	Temp. (°C)	Velocity 1 Z-direction (m/s)	Velocity 2 Y-direction (m/s)	Velocity 3 X-direction (m/s)
172	1055	B	1	H	1	66	0.66	22.8	1514	1515	
172	1055	B	1	H	2	55	2.05	22.6	1506	1514	
172	1055	B	1	H	2	125	2.75	22.4	1510	1510	
172	1055	B	1	H	3	57	3.57	22.5	1516	1524	
172	1055	B	2	H	1	82	5.32	22.8	1520	1532	
172	1055	B	2	H	3	83	8.33	22.3	1513	1516	
172	1055	B	2	H	4	62	9.62	23	1507	1531	
172	1055	B	3	H	1	28	14.28	23.6	1530	1533	
172	1055	B	3	H	3	18	17.18	23.3	1527	1538	
172	1055	B	3	H	5	26	20.26	22.9	1519	1511	
172	1055	B	4	H	1	58	24.08	23	1572	1587	
172	1055	B	4	H	3	133	27.83	23.2			1619
172	1055	B	4	H	5	123	30.73	23.2			1620
172	1055	B	5	H	1	66	33.66	22.6			1638
172	1055	B	5	H	3	66	36.66	23			1588
172	1055	B	5	H	5	126	40.26	22.3			1579
172	1055	B	6	H	1	135	43.85	22.3			1586
172	1055	B	6	H	3	74	46.24	22.3			1574
172	1055	B	7	H	1	83	52.83	23.4			1596
172	1055	B	7	H	3	50	55.5	20			1607

This table also appears on the volume CD-ROM.

from 70 to 75 mbsf (Fig. 48), possibly as a result of distortion of the sediment fabric by gas expansion.

Normalized shear strength, which is represented by the ratio of S_u to the effective overburden stress (P_o'), can be used to assess the stress history of sediment. Normally consolidated sediment S_u/P_o' ratios vary from 0.2 to 0.22 (Ladd et al., 1977). In the upper 60 mbsf of Site 1054, the average S_u/P_o' ratio is close to this value (Fig. 48), but farther down a steplike decrease to much lower ratios is observed, indicating underconsolidated sediments. However, we cannot ignore that this might be an artifact of disturbance caused by gas expansion. In nearby Site 1055, the step to lower S_u/P_o' ratios occurs just below 20 mbsf (Fig. 48).

Thermal Conductivity

For Site 1054, one measurement per core was made for both Holes 1054B and 1054C (Tables 36, 37). The values range from 0.671 to 1.084 W/(m·K) and form two distinct groupings (Fig. 49). Shallower than 65 mbsf, the readings increase slightly with depth and average 0.94 W/(m·K), whereas below that depth the variability in measurements (0.671–1.084 W/[m·K]) increases while the trend maintains the same average value. This change coincides with increasing variability in GRAPE bulk density data and reflects the unavoidable sampling of small, fluid-filled gas expansion voids in the cores recovered from below 65 mbsf.

Measurement density was increased to three per core at Holes 1055B, 1055C, and 1055D. The data range from 0.66 to 1.24 W/(m·K) (Fig. 49). Thermal conductivity values increase rapidly with depth in the upper 5 mbsf, then remain steady until 65 mbsf, at which point they exhibit a pattern of widely varying values (0.66–1.24 W/[m·K]) similar to that observed at Site 1054B.

Resistivity

Resistivity at Site 1055C was measured using the Wayne-Kerr Precision Component Analyzer with a four-electrode probe (see "Physical Properties" section, "Explanatory Notes" chapter, this volume). In general, two measurements per section were made.

Electrical resistivity (Tables 38, 39) increases with depth below seafloor (Fig. 50), which is expected for increasingly compacted sediment. Resistivity is a function of the porosity and tortuosity (and, to a lesser extent, mineralogy) of sediments (Boyce, 1980). The general trend of increasing resistivity with depth below seafloor is consistent with the index properties results of decreasing porosity with depth (Fig. 47). Anisotropy of resistivity also increases with depth below seafloor, with the "bed parallel" resistivity (transverse) in general being lower than resistivity perpendicular to bedding (longitudinal; see Fig. 50). This trend is probably caused by a millimeter-scale, diagenetic parting fabric observed at this site as the sediment becomes more consolidated.

SITE GEOPHYSICS

The Survey

At 0700 hr on 19 February, we began deploying seismic gear, which included a GI air gun, a Teledyne single-channel oil-filled streamer, and a new six-channel seismic streamer produced by Inno-

Table 34. Undrained shear-strength measurements from Site 1054.

Leg	Site	Hole	Core	Type	Section	Interval (cm)	Depth (mbsf)	Spring no.	Undrained shear strength (kPa)	Residual strength (kPa)
172	1054	B	1	H	1	86	0.864	B-1	4.3	2.6
172	1054	B	2	H	1	129	3.986	B-1	6.7	3.8
172	1054	B	2	H	3	115	6.849	B-1	7.4	3
172	1054	B	2	H	3	140	7.101	B-2	7.9	3.7
172	1054	B	2	H	5	117	9.874	B-2	11.1	4.8
172	1054	B	3	H	1	114	13.341	B-2	16.6	7.5
172	1054	B	3	H	3	92	16.122	B-2	19.4	9.5
172	1054	B	3	H	5	96	19.157	B-2	12.3	5.8
172	1054	B	4	H	2	134	24.54	B-4	25.8	9.6
172	1054	B	4	H	4	104	27.238	B-4	29.9	12.5
172	1054	B	4	H	6	104	30.236	B-4	20.5	7.3
172	1054	B	5	H	2	116	33.858	B-4	18.7	7.5
172	1054	B	5	H	4	91	36.613	B-4	30.7	10.8
172	1054	B	5	H	6	124	39.939	B-4	39.5	14.2
172	1054	B	6	H	2	134	43.541	B-4	32.9	12
172	1054	B	6	H	4	119	46.385	B-4	35.3	9.4
172	1054	B	6	H	6	118	49.38	B-4	52.9	15.5
172	1054	B	7	H	2	135	53.047	B-4	42.8	16.7
172	1054	B	7	H	4	141	56.11	B-4	35	15.3
172	1054	B	8	H	2	139	59.79	B-4	50.8	18.4
172	1054	B	8	H	4	115	62.549	B-4	35.3	12.1
172	1054	B	8	H	6	100	65.404	B-4	37.7	15.3
172	1054	B	9	H	2	128	69.179	B-4	7.4	3.4
172	1054	B	9	H	4	62	71.518	B-4	6.8	1.8
172	1054	B	9	H	6	109	74.99	B-4	12	8.1
172	1054	B	10	H	2	81	78.206	B-4	30.3	11
172	1054	B	10	H	4	98	81.384	B-4	17.9	4.5
172	1054	B	10	H	6	116	84.559	B-4	35.3	10.2
172	1054	B	11	H	2	113	88.033	B-4	35.6	14.7
172	1054	B	11	H	4	115	91.047	B-4	29.8	8.3
172	1054	B	11	H	6	133	94.227	B-4	43.4	18.1
172	1054	B	12	H	2	104	97.44	B-4	59.1	21.1
172	1054	B	12	H	4	91	100.313	B-4	21.9	8

This table also appears on the volume CD-ROM.

Table 35. Undrained shear-strength measurements from Site 1055.

Leg	Site	Hole	Core	Type	Section	Interval (cm)	Depth (mbsf)	Spring no.	Undrained shear strength (kPa)	Residual strength (kPa)
172	1055	C	1	H	1	86	0.86	B-1	2.5	1.2
172	1055	C	1	H	3	135	4.35	B-1	5.6	2.5
172	1055	C	1	H	5	124	7.24	B-1	8.4	3.6
172	1055	C	2	H	1	107	9.57	B-1	6.9	3.5
172	1055	C	2	H	3	126	12.76	B-1	9.3	3.7
172	1055	C	2	H	5	135	15.85	B-2	10.8	6.1
172	1055	C	3	H	1	52	18.52	B-2	14.4	6.4
172	1055	C	4	H	1	130	28.8	B-2	16.5	8.2
172	1055	C	4	H	3	60	31.1	B-2	14.2	5.6
172	1055	C	4	H	5	137	34.87	B-2	21	1.2
172	1055	C	5	H	1	120	38.2	B-2	15	7.2
172	1055	C	5	H	3	128	41.28	B-2	12.1	3.7
172	1055	C	5	H	5	119	44.19	B-2	15	8
172	1055	C	5	H	7	61	46.61	B-2	4.7	1.9
172	1055	C	6	H	1	135	47.85	B-4	13.9	5.8
172	1055	C	6	H	3	143	50.93	B-4	22.8	9.8
172	1055	C	6	H	5	142	53.92	B-4	40.8	18.8
172	1055	C	7	H	1	25	56.245	B-4	16.5	7.4
172	1055	C	7	H	3	12	59.115	B-4	21	7.1
172	1055	C	7	H	5	129	63.294	B-4	36.2	16.2
172	1055	C	8	H	1	140	66.897	B-4	19.1	10.1
172	1055	C	8	H	3	134	69.844	B-4	26.4	12.5
172	1055	C	8	H	5	111	72.614	B-4	21.8	11.3
172	1055	C	9	H	1	95	75.95	B-4	27.2	9.7
172	1055	C	9	H	3	86	78.855	B-4	16.4	3.9
172	1055	C	9	H	5	118	82.184	B-4	20.1	10.9
172	1055	C	10	H	2	13	83.186	B-4	24.7	11.6
172	1055	C	10	H	3	9	84.653	B-4	26.5	11.6
172	1055	C	10	H	6	119	90.246	B-4	23.4	8.3
172	1055	C	11	H	2	88	93.5	B-4	40.9	15.1
172	1055	C	11	H	4	76	96.382	B-4	32.4	11.7
172	1055	C	11	H	6	68	99.296	B-4	27.2	9.4
172	1055	C	12	H	2	14	103.142	B-4	42.5	13.1
172	1055	C	12	H	4	88	106.883	B-4	39.6	17
172	1055	C	12	H	6	32	109.32	B-4	22.8	7
172	1055	C	13	H	2	96	112.562	B-4	29.6	11.2
172	1055	C	13	H	4	118	115.784	B-4	41.1	14.8
172	1055	C	13	H	6	78	118.378	B-4	25.5	8.8

This table also appears on the volume CD-ROM.

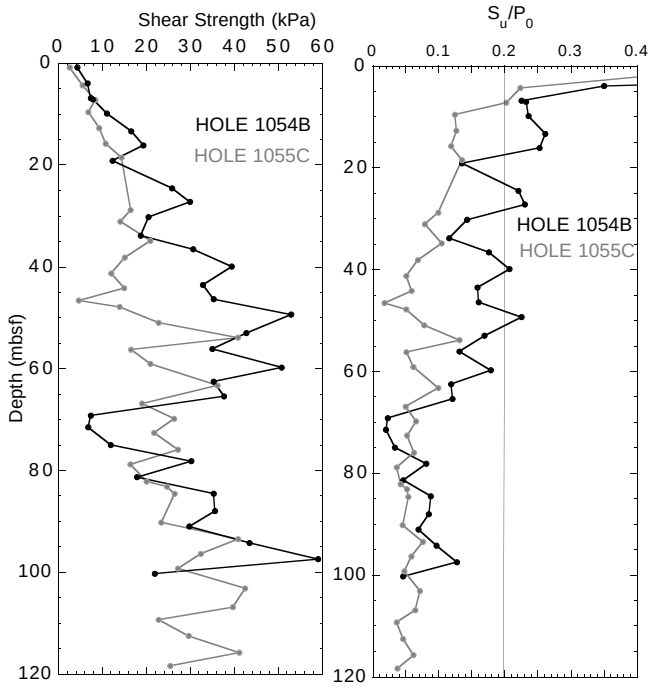

Figure 48. Comparison of vertical profiles of undrained shear strength (left) and normalized shear strength (right) for Holes 1054B and 1055C. The vertical line indicates normalized shear strength for normally consolidated sediments (Ladd et al., 1977).

vative Transducers Incorporated. By 1200 hr, we began a 46-km-long seismic survey (Line 1) over the first two drill sites, Sites 1054 and 1055. In addition to seismic surveying, we collected 3.5- and 12-kHz precision depth recorder (PDR) data along the survey profile. No multichannel seismic data were recorded during the survey because the multichannel streamer failed when deployed because of a pin configuration problem with the streamer.

The survey line runs from west to east across Site 1055 and then turns and recrosses Site 1055 on a south-to-north profile that also crosses Site 1054. After another course change, the survey line recrosses Site 1054 on a northeast-to-southwest profile (Fig. 51). The seismic survey ended at the southwestern end of the profile, shown on Figure 51, although the PDR survey continued on the ship's return course to Site 1054.

The survey was conducted mainly at speeds of 8.5 to 5.5 kt. The seismic data quality, as observed on chart recorders during the survey, begins to degrade at speeds in excess of 8 kt, whereas maintaining the ship's course becomes more difficult at speeds of less than ~5.0 kt. Thus, a speed of ~6 kt maintained over the portions of the survey line within ~3 km of the sites best optimizes the seismic data quality. Accurate positioning was obtained using a dGPS.

PDR (3.5 kHz) Data

The 3.5-kHz record over Site 1054 (Fig. 52) shows several prominent sub-bottom reflections from the seafloor down to 0.05 s two-way traveltime (TWT) below the seafloor, and a few faint reflections are present down to 0.08 s TWT. Laterally continuous reflections occur at ~0.008, 0.011, 0.018, and 0.021 s TWT. Underlying these is a reflection of variable depth that appears to mark the top of a lens-

Table 36. Thermal conductivity measurements from Site 1054.

Leg	Site	Hole	Core	Type	Section	Interval (cm)	Depth (mbsf)	Thermal conductivity (W/[m·K])
172	1054	B	1	H	2	50	2	0.876
172	1054	B	2	H	5	50	9.2	0.918
172	1054	B	3	H	5	50	18.7	0.938
172	1054	B	4	H	5	50	28.2	0.936
172	1054	B	5	H	5	50	37.7	1.028
172	1054	B	6	H	5	50	47.2	1.006
172	1054	B	7	H	4	50	55.2	1.049
172	1054	B	8	H	5	50	63.4	1.026
172	1054	B	9	H	5	50	72.9	0.786
172	1054	B	10	H	5	50	82.4	1.083
172	1054	B	11	H	5	50	91.9	0.671
172	1054	B	12	H	5	50	101.4	0.684
172	1054	C	1	H	2	50	2	0.868
172	1054	C	2	H	2	50	10.2	0.904
172	1054	C	3	H	2	50	19.7	0.977
172	1054	C	5	H	2	50	30.2	0.982
172	1054	C	6	H	2	50	39.7	1.018
172	1054	C	7	H	2	50	49.2	0.987
172	1054	C	9	H	2	50	60.7	0.967
172	1054	C	10	H	2	50	70.2	1.084
172	1054	C	11	H	2	50	79.7	0.999
172	1054	C	12	H	2	50	89.2	0.957
172	1054	C	13	H	2	50	98.7	0.968

This table also appears on the volume CD-ROM.

Table 37. Thermal conductivity measurements from Site 1055.

Leg	Site	Hole	Core	Type	Section	Interval (cm)	Depth (mbsf)	Thermal conductivity (W/[m·K])
172	1055	B	4	H	3	50	27	1
172	1055	B	5	H	3	50	36.5	0.99
172	1055	B	6	H	3	50	46	1.24
172	1055	B	7	H	3	50	55.5	1.07
172	1055	B	8	H	3	50	65	0.82
172	1055	B	9	H	3	50	74.5	0.92
172	1055	B	10	H	3	50	84	0.89
172	1055	B	11	H	3	50	92.7	0.8
172	1055	B	12	H	3	50	102.6	1
172	1055	B	13	H	3	50	111.3	1.15

This is a sample of the table that appears on the volume CD-ROM.

shaped body (at 0.026 s TWT at Site 1054), and two prominent reflections that do not extend far from Site 1054 at 0.038 and 0.047 s TWT.

The 3.5-kHz record over Site 1055 shows two laterally continuous reflections at ~0.009 and 0.014 s TWT (Fig. 53). Fainter reflections are present down to ~0.045 s TWT.

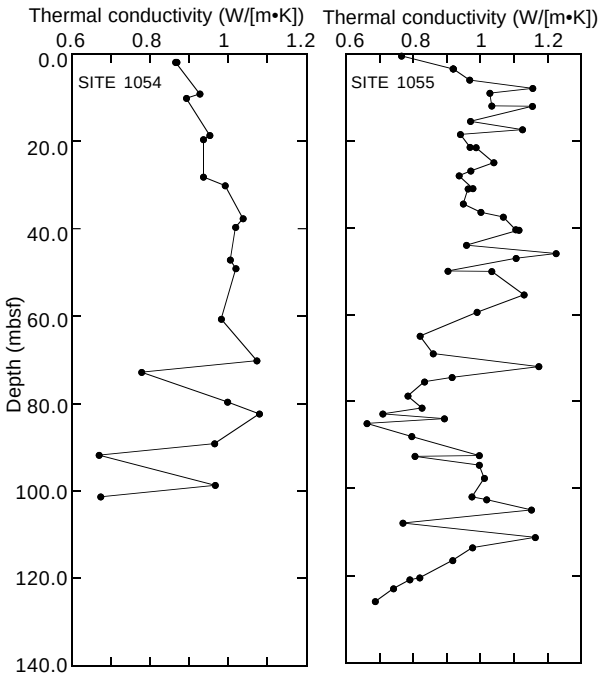

Figure 49. Thermal conductivity vs. depth at Sites 1054 and 1055.

Seismic Data

Very good seismic images were obtained using the GI gun and the Teledyne single-channel oil-filled streamer. The seismic processing consisted of a 15- to 20-Hz band-pass filter, deconvolution, and automatic gain control.

The profile over Site 1054 shows that the site is located within a subsurface depression, which, based on the drilling results, has filled since the Pliocene (Fig. 54). Note that the apparent relief on the seismic profile is an artifact related to the survey track. The seafloor here dips uniformly downslope at 2.8°. Other seismic records suggest that the subsurface depression may have formed by the rotation of relatively large blocks associated with nearby downslope movement. Within the depression, reflectors are flatlying and onlap or merge with northeast dipping reflectors (apparent dip). Numerous reflections are observed on the seismic record in this region. The most important reflections appear to be at 0.064, 0.078 (which both appear to mark unconformities), and 0.16 s TWT (which marks the contact of the sediment fill with the underlying blocks). A sediment-filled channel(?) occurs at ~0.01 s TWT at shotpoint 3450 southwest of Site 1054. The downslope continuation of this feature may be imaged at shotpoint 3070.

A filled channel is also evident to the north of Site 1055 at shotpoint 2450 (Fig. 55). A possible fault, which has an apparent southerly dip, merges with the channel. Site 1055, however, lies within a region of relatively flat-lying reflectors. The seismic-reflection profile shows numerous reflections, with distinct reflections at ~0.09, 0.11, and 0.14 s TWT. The reflections at ~0.11 and 0.14 s TWT appear to mark seismic unconformities. There are also a number of closely spaced reflections below 0.14 s TWT. As at Site 1054, the apparent relief on the acoustic profiles is caused by the survey track. The seafloor is generally flat and dipping downslope at 1.4°.

A BSR is present at both sites but is slightly deeper and less distinct at Site 1055 (at ~0.42 s TWT) than at Site 1054 (0.38 s TWT), which places the BSR below 300 mbsf at both sites.

Table 38. Resistivity measurements from Site 1054.

Leg	Site	Hole	Core	Type	Section	Interval (cm)	Depth (mbsf)	Temperature (°C)	Resistance Z-direction (Ω)	Resistance Y-direction (Ω)	Resistivity Z-direction (Ωm)	Resistivity Y-direction (Ωm)
172	1054	B	1	H	1	124	1.24	20.9	5.589	5.412	0.575	0.557
172	1054	B	2	H	1	135	4.05	20.4	6.663	6.929	0.686	0.713
172	1054	B	2	H	3	136	7.06	21.1	7.074	7.261	0.728	0.747
172	1054	B	2	H	5	128	9.98	21.6	6.182	6.504	0.636	0.669
172	1054	B	3	H	1	130	13.5	21.2	13.872	11.411	1.427	1.174
172	1054	B	3	H	3	129	16.49	21.4	7.169	6.837	0.738	0.703
172	1054	B	3	H	5	140	19.6	21.9	6.467	6.785	0.665	0.698
172	1054	B	4	H	2	126	24.46	21.2	7.599	7.967	0.782	0.82
172	1054	B	4	H	4	135	27.55	21.3	8.347	8.268	0.859	0.851
172	1054	B	4	H	6	132	30.52	21.4	8.794	7.399	0.905	0.761
172	1054	B	5	H	2	143	34.13	21.5	6.842	6.876	0.704	0.707
172	1054	B	5	H	4	143	37.13	21.6	8.127	8.3	0.836	0.854
172	1054	B	5	H	6	140	40.1	21	8.018	8.005	0.825	0.824
172	1054	B	6	H	2	123	43.43	22	7.212	7.405	0.742	0.762
172	1054	B	6	H	4	133	46.53	22	7.943	8.136	0.817	0.837
172	1054	B	6	H	6	133	49.53	22.9	8.234	8.12	0.847	0.836
172	1054	B	7	H	2	121	52.91	21.7	7.757	8.382	0.798	0.862
172	1054	B	7	H	4	124	55.94	21.8	9.07	9.082	0.933	0.934
172	1054	B	8	H	2	120	59.6	22.2	7.87	7.703	0.81	0.793
172	1054	B	8	H	4	130	62.7	22.2	12.182	10.917	1.253	1.123
172	1054	B	8	H	6	140	65.8	22.5	12.964	10.507	1.334	1.081
172	1054	B	9	H	2	135	69.25	22.7	10.25	9.681	1.055	0.996
172	1054	B	9	H	4	122	72.12	22.1	9.245	9.651	0.951	0.993
172	1054	B	9	H	6	137	75.27	22.1	8.806	7.212	0.906	0.742
172	1054	B	10	H	2	134	78.74	22.4	10.57	9.448	1.088	0.972
172	1054	B	10	H	4	133	81.73	22.4	17.093	15.503	1.759	1.595
172	1054	B	10	H	6	138	84.78	22.4	11.599	10.667	1.193	1.098
172	1054	B	11	H	2	103	87.93	22.4	12.428	11.622	1.279	1.196
172	1054	B	11	H	4	106	90.96	22.4	12.235	11.282	1.259	1.161
172	1054	B	11	H	6	118	94.08	22.2	9.68	11.156	0.996	1.148
172	1054	B	12	H	2	140	97.8	22.4	13.358	12.275	1.374	1.263
172	1054	B	12	H	4	130	100.7	22.2	33.974	24.812	3.496	2.553
172	1054	B	12	H	6	8	102.48	22.4	14.169	11.295	1.458	1.162

This table also appears on the volume CD-ROM.

Table 39. Resistivity measurements from Site 1055.

Leg	Site	Hole	Core	Type	Section	Interval (cm)	Depth (mbsf)	Temperature (°C)	Resistance Z-direction (Ω)	Resistance Y-direction (Ω)	Resistivity Z-direction (Ωm)	Resistivity Y-direction (Ωm)
172	1055	C	1	H	1	0.7	0.007	20.4	5.087	4.878	0.523	0.502
172	1055	C	1	H	1	1.2	0.012	20.4	5.841	5.52	0.601	0.568
172	1055	C	1	H	2	0.4	1.504	20	6.229	5.964	0.641	0.614
172	1055	C	1	H	2	1.27	1.5127	20	6.563	6.074	0.675	0.625
172	1055	C	1	H	3	0.25	3.0025	20.5	5.957	5.664	0.613	0.583
172	1055	C	1	H	3	0.9	3.009	20.5	6.868	6.277	0.707	0.646
172	1055	C	1	H	3	1.25	3.0125	20.5	9.124	8.106	0.939	0.834
172	1055	C	1	H	4	0.27	4.5027	20.8	7.03	6.633	0.723	0.683
172	1055	C	1	H	4	0.85	4.5085	20.8	6.298	6.219	0.648	0.64
172	1055	C	1	H	4	1.25	4.5125	20.8	6.91	6.489	0.711	0.668
172	1055	C	1	H	5	0.25	6.0025	20.2	7.323	7.014	0.753	0.722

This is a sample of the table that appears on the volume CD-ROM.

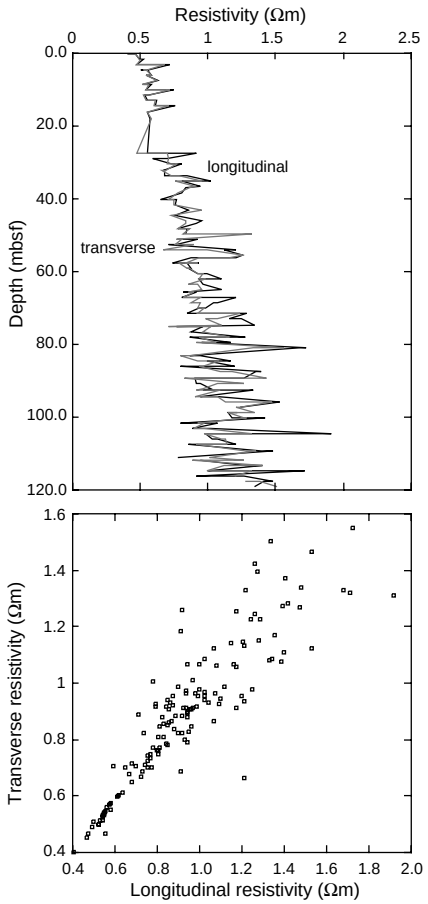

Figure 50. Resistivity (top) and resistivity-anisotropy (bottom) at Hole 1055C. Resistivity-anisotropy increases at higher resistivity values (i.e., the greater the scatter) found with increasing depth below seafloor. This trend is considered to be caused by the development of a diagenetic parting fabric parallel to the bedding plane, thus increasing electrical resistance in the longitudinal direction.

Correlation

Correlations between the reflection records and the cored sediments were undertaken both on a qualitative and a quantitative basis. First, a regional depth-velocity model (see "Explanatory Notes" chapter, this volume) was used to estimate the sub-bottom depths associated with the reflections at the site. These depths were compared to the recovered core to determine the kinds of lithologic changes occurring at those depths that may be responsible for the reflections.

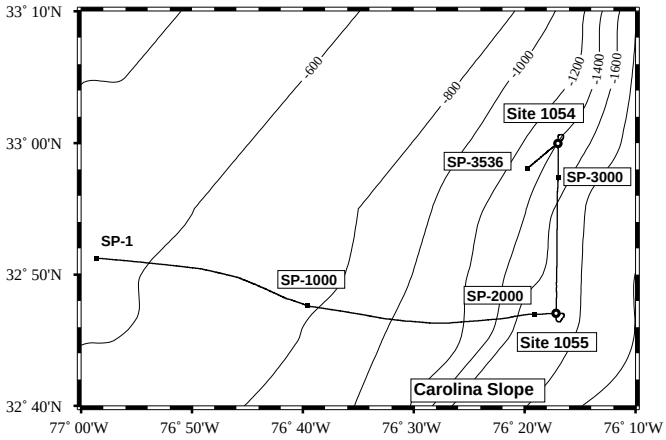

Figure 51. Survey track over Sites 1054 and 1055, with shotpoint (SP) numbers given along survey Line 1. Depths on contours are in meters.

Second, a quantitative analysis of GRAPE and other available physical properties data provided estimates of downcore impedance contrasts. Third, downcore bulk density measurements were used as input to a synthetic seismogram program, which was then related to the observed seismic record.

Lithologic Correlations

At Site 1054, the uppermost parallel reflections appear to correspond to sharp downcore magnetic susceptibility changes that may be related to slope failure and sediment removal. The prominent reflection at 0.038 s TWT appears to correlate with a carbonate-rich turbidite recovered at ~28 mbsf in Sections 172-1054A-4H-2 and 4H-4. The reflections below ~0.038 s TWT are too numerous to correlate in detail with the cored lithology, but the change from fill to the underlying material occurs at ~0.16 s TWT (~123 mbsf). This appears to correspond with the Unit II/Unit III boundary.

At Site 1055, many of the prominent reflections appear to occur at depths of pronounced changes in magnetic susceptibility, suggesting that the reflectors represent lithologic variations in the cores. The seismic discontinuity at 0.11 s TWT (~84 mbsf) may correspond to the Unit I/Unit II boundary.

Acoustic Impedance

Acoustic impedance calculated from bulk densities and compressional wave velocities that were measured with the PWL and GRAPE tools on the MST (See "Physical Properties" section, this chapter) provides information about reflectors to a depth of ~50 mbsf at Site 1054. We note that the acoustic impedance profile we present here (Fig. 56) is based on unedited data that are not corrected for system-

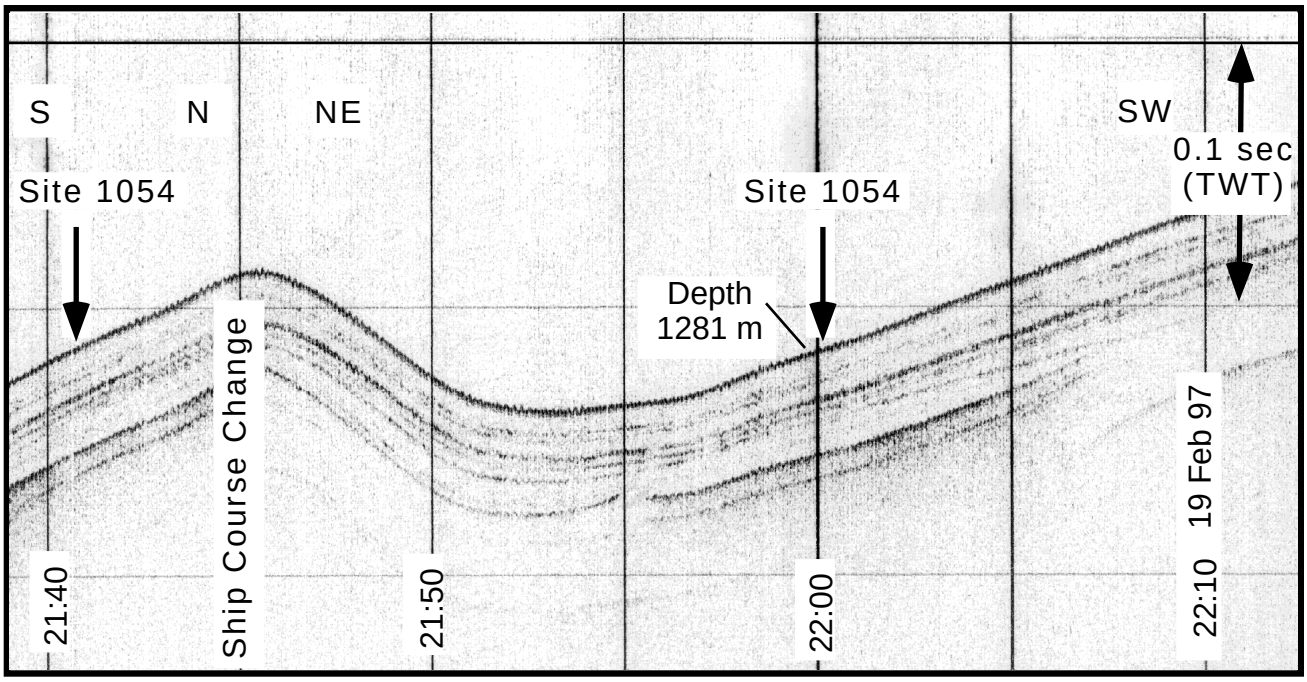

Figure 52. PDR (3.5 kHz) profile collected over Site 1054. Note that topographic variation mainly reflects changes in the course of the ship.

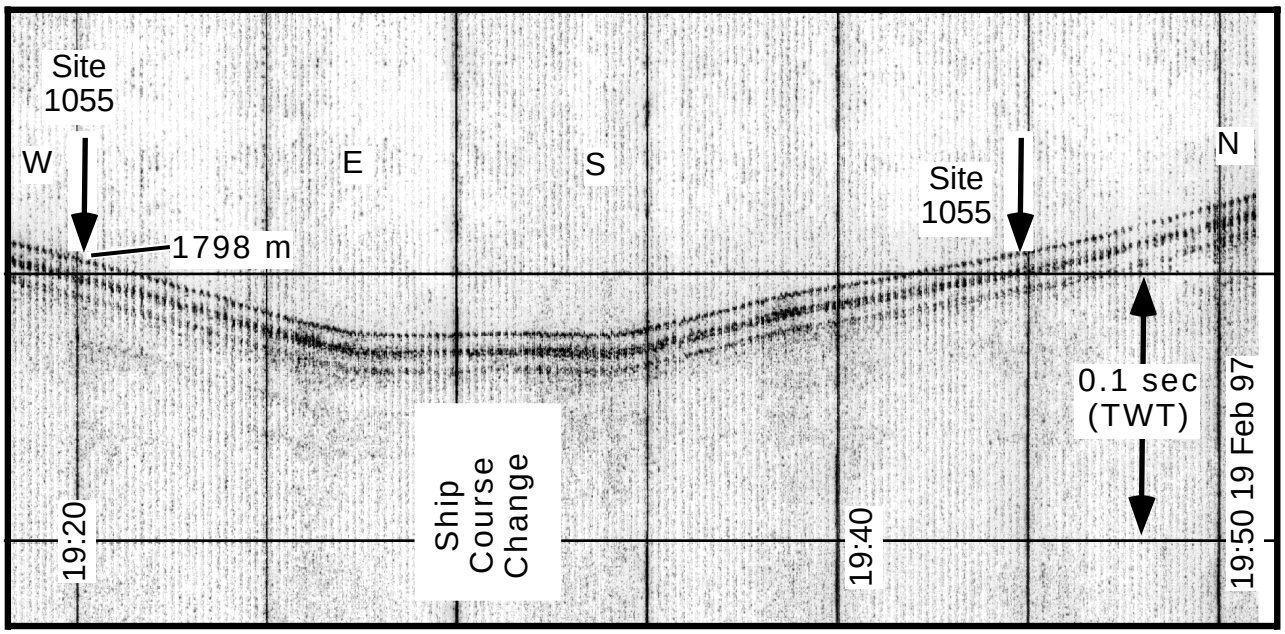

Figure 53. PDR (3.5 kHz) profile of Site 1055. Note that topographic variation mainly reflects changes in the course of the ship.

atic offsets between MST-measured *P*-wave velocity and bulk density and discrete measurements of the same quantities made on split cores (See "Physical Properties" section, this chapter). Once the data are edited and these offsets are corrected, we believe that the basic trends in acoustic impedance will remain, but that details may disappear (or appear) and the average values will probably shift higher. The PWL and GRAPE data from Site 1055 are much noisier and in need of significantly more editing than shipboard operations allow; thus, no acoustic impedance profile from this site will be presented in this report.

Three major excursions in acoustic impedance are observed in the MST data at Site 1054. The first is at ~0.030 s TWT (based on an average compressional wave velocity in sediments of 1.50 km/s). Below that, the acoustic impedance curve has significant excursions at 0.038 and 0.042 s TWT. These three excursions match reasonably well with three reflectors observed in the 3.5-kHz echograms. The first, at 0.030 s TWT, is slightly deeper than the reflector that defines the lens-shaped body, which begins at 0.027 s TWT. The second peak, at 0.038 s TWT, aligns with a strong, but laterally terminating, reflector at 0.038 s TWT. The last is at 0.045 s TWT and probably corresponds to a reflector observed at 0.047 s TWT. The excursion at 0.038 s TWT corresponds to a carbonate turbidite in the lithologic record.

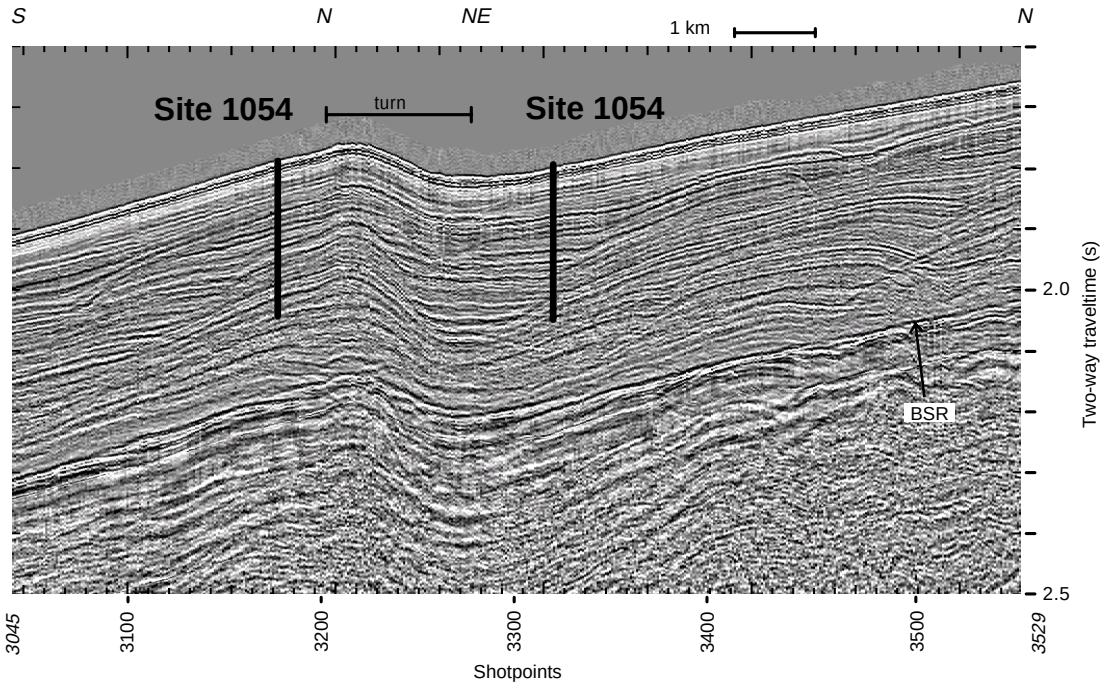

Figure 54. Processed single-channel seismic profile of Site 1054. The vertical bar shows the depth interval sampled at Site 1054. Prominent seismic reflections occur at ~0.038, 0.064, 0.078, and 0.16 s TWT (~29, 49, 61, and 123 mbsf).

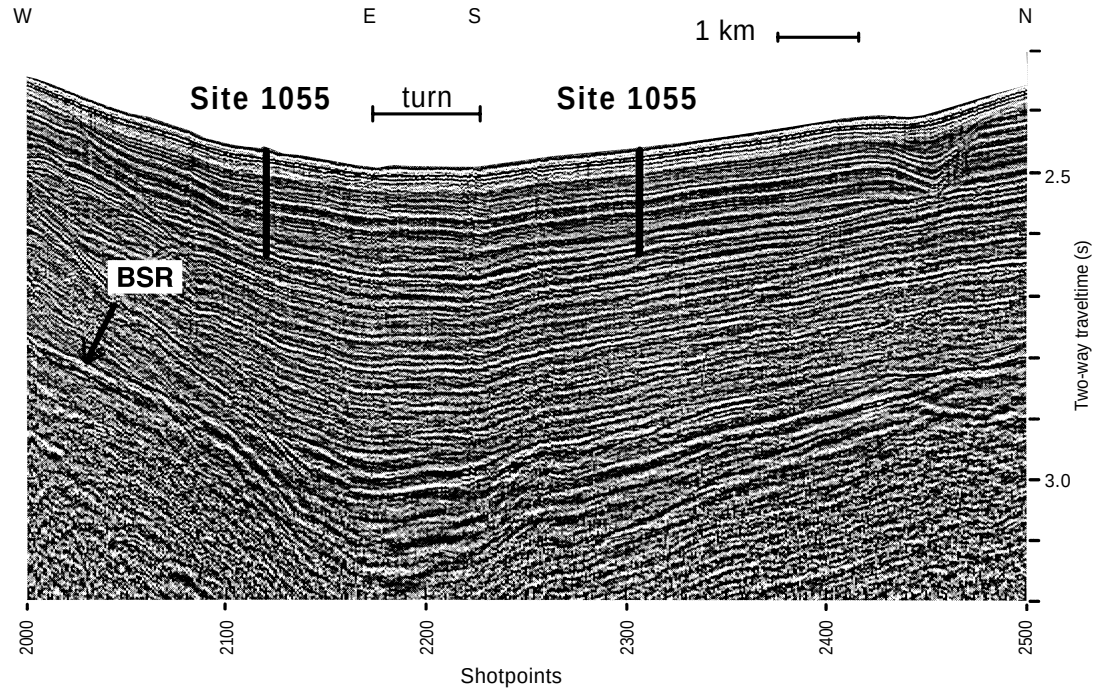

Figure 55. Processed single-channel seismic profile of Site 1055. The vertical bar shows the depth interval sampled at Site 1055. Prominent seismic reflections occur at ~0.09, 0.11, and 0.14 s TWT (~53, 84, and 107 mbsf).

Synthetic Seismograms

Because the cores are affected by gas expansion at both Sites 1054 and 1055, the seismic velocity and bulk density measurements are poor or absent below ~50 mbsf at both sites. Some downcore changes in bulk density occur; however, that may give rise to the prominent reflections observed in the site survey seismic profiles. To tentatively examine possible correlations between the seismic profiles and the cored sediments, synthetic seismograms were constructed by convolving a water gun signature with an impedance log derived from the discrete-sample density log (Fig. 55) and a synthetic velocity model (Figs. 57, 58).

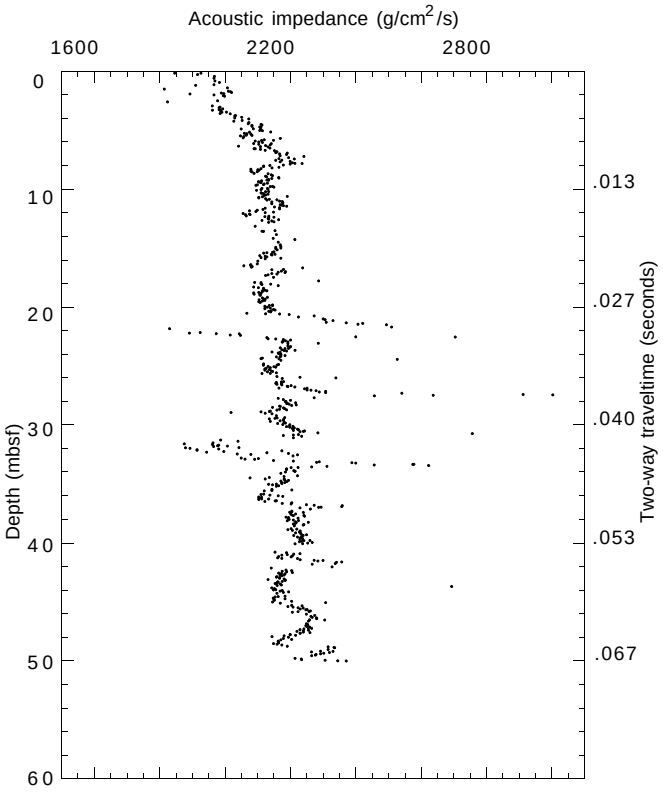

Figure 56. Acoustic impedance for the upper 50 mbsf at Site 1054 calculated from unedited GRAPE bulk density and PWL compressional wave velocity data. Acoustic impedance excursions at 0.030, 0.038, and 0.042 s TWT (based on estimated sediment velocity of 1.5 km/s) correspond to reflectors observed in the 3.5-kHz echograms (see Fig. 52).

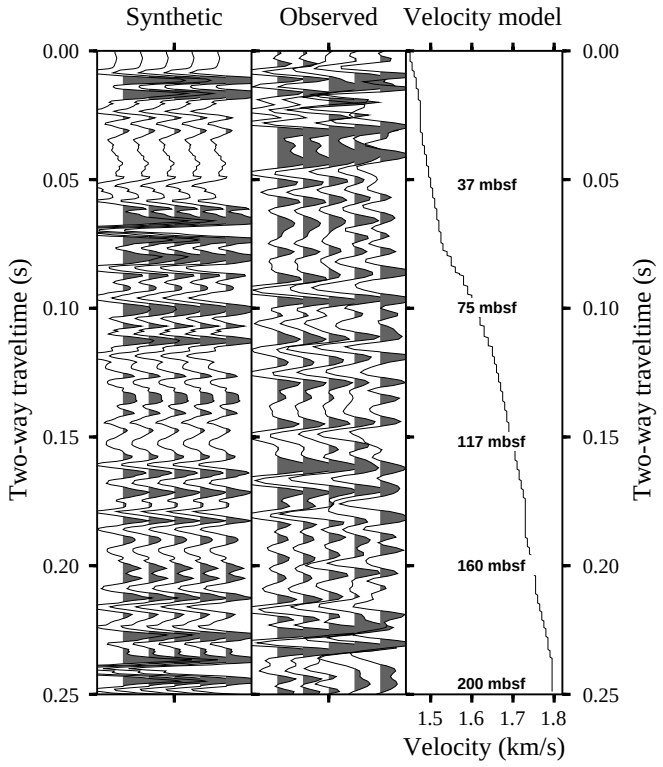

Figure 57. Synthetic seismogram for Site 1054. The observed seismic traces are for shotpoints 3310–3314.

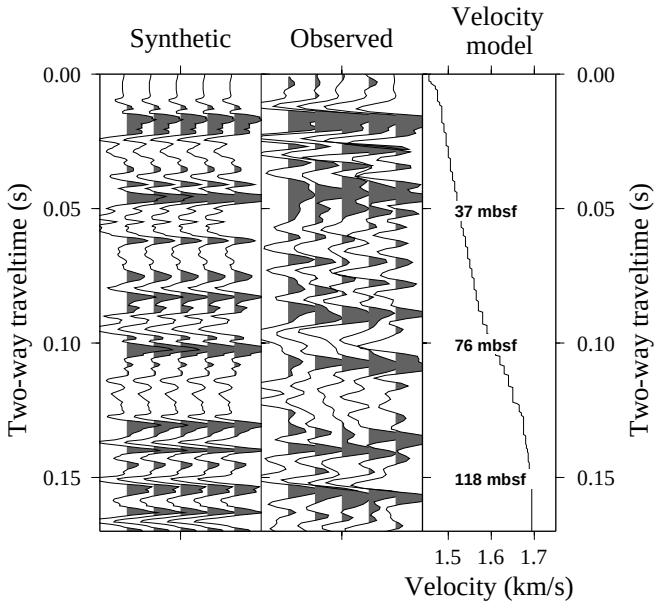

Figure 58. Synthetic seismogram for Site 1055. The observed seismic traces are for shotpoints 2109–2113.

The synthetic seismogram for Site 1054 agrees moderately well with the observed record, although there are intervals of very poor agreement, such as between 0.025 and 0.06 s TWT (Fig. 57). The general character of the top two reflectors and many of the characteristics of the deeper reflectors are well modeled considering the lack of seismic velocity information and the rather large spacing (~3 m) between density observations.

The synthetic seismogram for Site 1055 agrees well with the observed record, although a slightly more complex seismic model should improve correlation further (Fig. 58). Several interesting correlations can be made with the core. For example, the broad reflection on the observed record at ~0.045 s TWT corresponds to an increase in density variations that occurs between 27 and 38 mbsf. The core photos (e.g., Cores 172-1055B-5H and 4H, "Section 4," this volume) show a clear change in the character of the core recovered within this interval; the core above the interval has few cracks, whereas below the interval cracks are numerous. The cracks result from postcoring gas expansion, but likely reflect the amount of gas and how the sediments respond to gas expansion, both of which could lead to an impedance contrast. Similarly, the prominent reflection at 0.016 s TWT appears to correspond to an uphole increase in lightness (L*) of the core at ~115–125 mbsf (Cores 172-1055B-13H and 14H, "Section 4," this volume). Other first-order correlations can be seen, but further work is needed for detailed correlations.

REFERENCES

Baldauf, J.G., 1984. Cenozoic diatom biostratigraphy and paleoceanography of the Rockall Plateau region, North Atlantic, Deep Sea Drilling Project Leg 81. *In* Roberts, D.G., Schnitker, D., et al., *Init. Repts. DSDP,* 81: Washington (U.S. Govt. Printing Office), 439–478.

Barron, J.A., 1985. Late Eocene to Holocene diatom biostratigraphy of the equatorial Pacific Ocean, Deep Sea Drilling Project Leg 85. *In* Mayer, L., Theyer, F., Thomas, E., et al., *Init. Repts. DSDP,* 85: Washington (U.S. Govt. Printing Office), 413–456.

Berggren, W.A., Hilgen, F.J., Langereis, C.G., Kent, D.V., Obradovich, J.D., Raffi, I., Raymo, M.E., and Shackleton, N.J., 1995. Late Neogene chronology: new perspectives in high-resolution stratigraphy. *Geol. Soc. Am. Bull.,* 107:1272–1287.

Berner, R.A., 1984. Sedimentary pyrite formation: an update. *Geochim. Cosmochim. Acta,* 48:605–615.

Biscaye, P.E., and Anderson, R.F., 1994. Fluxes of particulate matter on the slope of the southern Middle Atlantic Bight: SEEP II. *Deep-Sea Res.*, 41:459–509.

Boyce, R.E., 1980. Determination of the relationships of electrical resistivity, sound velocity, and density/porosity of sediment and rock by laboratory techniques and well logs from Deep Sea Drilling Project Sites 415 and 416 off the coast of Morocco. *In* Lancelot, Y., Winterer, E.L., et al., *Init. Repts. DSDP,* 50: Washington (U.S. Govt. Printing Office), 305–318.

Boyle, E.A., and Keigwin, L.D., 1987. North Atlantic thermohaline circulation during the past 20,000 years linked to high-latitude surface temperature. *Nature,* 330:35–40.

Bukry, D., 1973. Low-latitude coccolith biostratigraphic zonation. *In* Edgar, N.T., Saunders, J.B., et al., *Init. Repts. DSDP,* 15: Washington (U.S. Govt. Printing Office), 685–703.

Chaisson, W.P., and Leckie, R.M., 1993. High-resolution Neogene planktonic foraminifer biostratigraphy of Site 806, Ontong Java Plateau (western equatorial Pacific). *In* Berger, W.H., Kroenke, L.W., Mayer, L.A., et al., *Proc. ODP, Sci. Results,* 130: College Station, TX (Ocean Drilling Program), 137–178.

Chaisson, W.P., and Pearson, P.N., 1997. Planktonic foraminifer biostratigraphy at Site 925: Middle Miocene–Pleistocene (last 12 m.y.). *In* Shackleton, N.J., Curry, W.B., Richter, C., and Bralower, T.J. (Eds.), *Proc. ODP, Sci. Results,* 154: College Station, TX (Ocean Drilling Program), 3-32.

Claypool, G.E., and Kaplan, I.R., 1974. The origin and distribution of methane in marine sediments. *In* Kaplan, I.R. (Ed.), *Natural Gases in Marine Sediments:* New York (Plenum), 99–139.

Claypool, G.E., and Kvenvolden, K.A., 1983. Methane and other hydrocarbon gases in marine sediment. *Annu. Rev. Earth Planet. Sci.*, 11:299–327.

Curry, W.B., Shackleton, N.J., Richter, C., et al., 1995. *Proc. ODP, Init. Repts.*, 154: College Station, TX (Ocean Drilling Program).

Dillon, W.P., Popenoe, P., Grow, J.A., Klitgord, K.D., Swift, B.A., Paull, C.K., and Cashman, K.V., 1982. Growth faulting and salt diapirism: their relationship and control in the Carolina Trough, Eastern North America. *In* Watkins, J.S., and Drake, C.L. (Eds.), *Studies of Continental Margin Geology.* AAPG Mem., 34:21–46.

Dowsett, H.J., 1988. Diachroneity of Late Neogene microfossils in the southwest Pacific Ocean: application of the graphic correlation method. *Paleoceanography,* 3:209–222.

Emerson, S., and Hedges, J.I., 1988. Processes controlling the organic carbon content of open ocean sediments. *Paleoceanography,* 3:621–634.

Espitalié, J., Deroo, G., and Marquis, F., 1986. La pyrolyse Rock-Eval et ses applications, Partie III. *Rev. Inst. Fr. Pet.*, 41:73–89.

Gieskes, J.M., 1981. Deep-sea drilling interstitial water studies: implications for chemical alteration of the oceanic crust, layers I and II. *In* Warme, J.E., Douglas, R.G., and Winterer, E.L. (Eds.), *The Deep Sea Drilling Project: A Decade of Progress.* Spec. Publ.—Soc. Econ. Paleontol. Mineral., 32:149–167.

GLORIA, EEZ-SCAN, 87 Scientific Staff, 1991. Atlas of the U.S. Exclusive Economic Zone, Atlantic Continental Margin. *U.S. Geol. Surv. Misc. Invest. Ser.,* I-2054.

Hathaway, J.C., 1972. Regional clay mineral facies in estuaries and continental margin of the United States East Coast. *Mem.—Geol. Soc. Am.,* 133:293–316.

Heezen, B.C., Hollister, C.D., and Ruddiman, W.F., 1966. Shaping of the continental rise by deep geostrophic contour currents. *Science,* 152:502–508.

Hesse, R., and Harrison, W.E., 1981. Gas hydrates (clathrates) causing porewater freshening and oxygen isotope fractionation in deep-water sedimentary sections of terrigenous continental margins. *Earth Planet. Sci. Lett.*, 55:453–462.

Hoppie, B.W., Blum, P., and the Shipboard Scientific Party, 1994. Natural gamma-ray measurements on ODP cores: introduction to procedures with examples from Leg 150. *In* Mountain, G.S., Miller, K.G., Blum, P., et al., *Proc. ODP, Init. Repts.*, 150: College Station, TX (Ocean Drilling Program), 51–59.

Kastner, M., 1979. Silica polymorphs. *In* Burns, R.G. (Ed.), *Marine Minerals.* Mineral. Soc. Am., Rev. Mineral., 6:99–111.

Kvenvolden, K.A., and Kastner, M., 1990. Gas hydrates of the Peruvian outer continental margin. *In* Suess, E., von Huene, R., et al., *Proc. ODP, Sci. Results,* 112: College Station, TX (Ocean Drilling Program), 517–526.

Ladd, C.C., Foott, R., Ishihara, K., Schlosser, F., and Poulos, H.G., 1977. Stress-deformation and strength characteristics: state-of-the-art report. *Proc. 9th Int. Conf. Soil Mech. and Found. Eng.*, Tokyo, 2:421–482.

Lehman, S.J., and Keigwin, L.D., 1992. Sudden changes in North Atlantic circulation during the last deglaciation. *Nature,* 356:757–762.

Lourens, L.J., Antonarakou, A., Hilgen, F.J., Van Hoof, A.A.M., Vergnaud-Grazzini, C., and Zachariasse, W.J., 1996. Evaluation of the Plio-Pleistocene astronomical timescale. *Paleoceanography,* 11:391–413.

Mackin, J.E., and Aller, R.C., 1984. Ammonium adsorption in marine sediments. *Limnol. Oceanogr.*, 29:250–257.

McIver, R.D., 1975. Hydrocarbon occurrences from JOIDES Deep Sea Drilling Project. *Proc. Ninth Petrol. Congr.*, 269–280.

Meyers, P.A., 1994. Preservation of elemental and isotopic source identification of sedimentary organic matter. *Chem. Geol.*, 144:289–302.

Meyers, P.A., and Brassell, S.C., 1985. Biogenic gases in sediments deposited since Miocene times on the Walvis Ridge, South Atlantic Ocean. *In* Caldwell, D.E, Brierley, J.A., and Brierley, C.L. (Eds.), *Planetary Ecology:* New York (Van Nostrand Reinhold), 69–80.

Müller, P.J., 1977. C/N ratios in Pacific deep sea sediments: effect of inorganic ammonium and organic nitrogen compounds sorbed by clays. *Geochim. Cosmochim. Acta,* 41:765–776.

Oppo, D.W., and Fairbanks, R.G., 1987. Variability in the deep and intermediate water circulation of the Atlantic Ocean during the past 25,000 years: Northern Hemisphere modulation of the Southern Ocean. *Earth Planet. Sci. Lett.*, 86:1–15.

Paull, C.K., Buelow, W.J., Ussler, W., III, and Borowski, W.S., 1996. Increased continental margin slumping frequency during sea-level lowstands above gas hydrate-bearing sediments. *Geology,* 24:143–146.

Paull, C.K., Matsumoto, R., Wallace, P.J., et al., 1996. *Proc. ODP, Init. Repts.*, 164: College Station, TX (Ocean Drilling Program).

Pedersen, T.F., and Shimmield, G.B., 1991. Interstitial water chemistry, Leg 117: contrasts with the Peru Margin. *In* Prell, W.L., Niitsuma, N., et al., *Proc. ODP, Sci. Results,* 117: College Station, TX (Ocean Drilling Program), 499–513.

Pickart, R.S., and Smethie, W.M., Jr., 1993. How does the deep western boundary undercurrent cross the Gulf Stream? *J. Phys. Oceanogr.*, 23:2602–2616.

Raffi, I., Backman, J., Rio, D., and Shackleton, N.J., 1993. Plio-Pleistocene nannofossil biostratigraphy and calibration to oxygen isotopes stratigraphies from Deep Sea Drilling Project Site 607 and Ocean Drilling Program Site 677. *Paleoceanography,* 8:387–408.

Rosenfeld, J.K., 1979. Ammonium absorption in nearshore anoxic sediments. *Limnol. Oceanogr.*, 24:356–364.

Shipboard Scientific Party, 1990. Site 767. *In* Rangin, C., Silver, E.A., von Breymann, M.T., et al., *Proc. ODP, Init. Repts.*, 124: College Station, TX (Ocean Drilling Program), 121–193.

————, 1996. Site 976. *In* Comas, M.C., Zahn, R., Klaus, A., et al., *Proc. ODP, Init. Repts.*, 161: College Station, TX (Ocean Drilling Program), 65–97.

————, 1996. Sites 991/992/993. *In* Paull, C.K., Matsumoto, R., Wallace, P.J., et al., *Proc. ODP, Init. Repts.*, 164: College Station, TX (Ocean Drilling Program), 65–97.

Smith, J.D., and Foster, J.H., 1969. Geomagnetic reversal in Brunhes normal polarity epoch. *Science,* 163:565–567.

Weaver, P.P.E., and Clement, B.M., 1987. Magnetobiostratigraphy of planktonic foraminiferal datums, DSDP Leg 94, North Atlantic. *In* Ruddiman, W.F., Kidd, R.B., Thomas, E., et al., *Init. Repts. DSDP,* 94: Washington (U.S. Govt. Printing Office), 815–829.

Wessel, P., and Smith, W.H.F., 1991. Free software helps map and display data. *Eos,* 72:441–446.

Ms 172-103

NOTE: Core-description forms ("barrel sheets") and core photographs can be found in Section 4, beginning on page 325. Forms containing smear-slide data can be found on CD-ROM. See Table of Contents for material contained on CD-ROM.

Prior Chapter Contents Next Chapter